Measurement of the Ratio of Charged and Neutral B Mesons in $\Upsilon(4S)$ Events via Partial Reconstruction of the Semileptonic Decays $\bar{B}^0 \to D^{*+}\ell^-\bar{\nu}_\ell$ and $B^- \to D^{*0}\ell^-\bar{\nu}_\ell$

Romulus Godang

Dissertation submitted to the Faculty of the

Virginia Polytechnic Institute and State University

in Partial Fullfilment of the Requirements for the Degree of

Doctor of Philosophy

in

Physics

Kay Kinoshita, Chair

Leo Piilonen, Co-Chair

Alexander Abashian, Marvin Blecher

Lay Nam Chang, Guy Indebetouw

August 23, 2000

Blacksburg, Virginia

Keywords: B Meson, Semileptonic Decay, Partial Reconstruction

Measurement of the Ratio of Charged and Neutral B Mesons in $\Upsilon(4S)$ Events via Partial Reconstruction of the Semileptonic Decays $\bar{B}^0 \to D^{*+}\ell^-\bar{\nu}_\ell$ and $B^- \to D^{*0}\ell^-\bar{\nu}_\ell$

Romulus Godang

ABSTRACT

The decays $\bar{B}^0 \to D^{*+}\ell^-\bar{\nu}_\ell$ and $B^- \to D^{*0}\ell^-\bar{\nu}_\ell$ are studied using data collected at the CLEO II detector at the Cornell Electron Storage Ring. Both decays are identified using a partial reconstruction method where the D^* is detected only through a pion daughter from the decay $D^* \to D\pi$. Because of the similarities in the analyses of the two modes, the ratio of the rates is measured in a way that is independent of the decay model, limited mainly by the uncertainty in the relative efficiency for detecting neutral and charged pions. This ratio is equivalent to the ratio of the product of production fraction and lifetime for charged and neutral B mesons, $\frac{f_{+-}\tau_+}{f_{00}\tau_0}$. It is combined with measurements of the lifetime ratio to obtain the ratio of charged and neutral B meson production at the $\Upsilon(4S)$ resonance, $\frac{f_{+-}}{f_{00}} = 1.071 \pm 0.085 \pm 0.139$.

Dedication

To my wonderful wife, Rosmawaty Godang, and my family.

Acknowledgments

I would like to thank Professor Kay Kinoshita for everything she has done over the years. She has taught me not only about High-Energy Physics but also about life with her kindness and patience. I am so lucky to have her as my Ph.D advisor during my graduate days. Her enthusiasm for the subject has deepened my own interest. Her expertise on semileptonic B meson decays using a partial reconstruction method is a great help. The work presented here would not be possible without her support and effort.

I would like to thank my Ph.D advisory committee members: Professors Leo Piilonen, Alexander Abashian, Marvin Blecher, Lay Nam Chang and Guy Indebetouw who always supported me for finishing the work. I am grateful to them for the support they have given me. Their time and effort were greatly appreciated.

I would like to acknowledge my paper committee members at CLEO collaboration: Professors Jon Thaler and Ron Poling, and Drs. Bonnie Valant-Spaight, Mark Dickson and Bruce Berger for their great suggestions.

I would also like to thank many people who have contributed greatly to this work: Profes-

sors David Cinabro, Tom Browder, Tomasz Skwarnicki, Ritchie Patterson, Arne Freyberger, Vladimir Savinov, Drs. Stephen Richichi, Steve Schrenk, Norman Morgan, Brian Heltsley, Karl Ecklund, Mark Palmer, Mike Saulnier, Jorge Rodriguez for their help and useful discussions. I would also like to thank all analysis coordinators: Professors Roy Briere, Frank Wuerthwein and David Jaffe and my fellows at CLEO collaboration.

I would especially like to thank Dr. Paula Pomianowski, whom I worked closely with for many years. She is a great person who often provided distractions. I thank her for mentoring me during the work on calibrating and monitoring the Time-of-Flight system at CLEO. I would also like to thank Dr. I Chung Lai as my office mate and for taking the time to discuss ways to improve this analysis.

As for my graduate days at Virginia Tech, I would like to thank Professors John Ficenec, Beate Schmittmann, Royce Zia, Randy Heflin, Clayton Williams, Luke Mo, Tetsuro Mizutani, Kazuo Gotow, Mark Pitt, and all Virginia Tech faculty. I am grateful to Christa Thomas, Janet Sanders, Judy Faw, Roger Link and Ross Perkins for their excellent and outstanding technical support and secretarial services. Thank you to my fellow Virginia Tech graduate students: Drs. Alwi Ahmed, Greg and Daniella Topasna, Mark Anderson, Russi Yordanov, Triampo Wannapong, Robert Astalos, and all my classmates.

Finally, I would like to thank my parents Fidelis and Adriana Godang, my parents-in-law Pohon and Anggrek Mahoni and my family for their encouragement and love. A special thank you to my wonderful wife, Rosmawaty, for her love and her patience during my graduate studies. Your deep love has been a great gift. I dedicate this thesis to you.

Contents

List of Figures

List of Tables

Chapter 1

Introduction

Elementary Particle Physics, also known as High Energy Physics, has made enormous advances in the last 30 years, especially concerning how all matter should be described in ultimate detail. Physicists have penetrated even inside the nucleus, which is made up of protons and neutrons. They have discovered a *"zoo"* of hundreds of observed particles.

Experiments have revealed families of short-lived particles that can be created from the energy released in the high energy collisions of other particles, such as protons and electrons. Generally, many particles are created as a result of the collision. There are unstable particles not seen in ordinary matter which are created along with stable particles. The unstable particles decay into stable particles soon after their creation. How long they take to decay, what they decay into, and how many times they decay into other particles are very important data in high energy physics.

1.1 Particle Classification

Particles are classified according to their fundamental properties. Each particle has an intrinsic angular momentum, called *spin*; however, there is no analog in classical mechanics for spin. *Mass*, *spin* and *electric charge* are fundamental characteristics of particles.

If we can determine the mass, spin and electric charge of a particle, then with an appropriate wave function we can tell the motion of the particle. In general each particle has its antiparticle which has an opposite electric charge.

It is an amazing fact of nature that all wave functions for identical particles are either symmetric or antisymmetric under their interchange. Wolfgang Pauli noted a profound connection between spin and symmetry. Such a connection leads to the *Pauli exclusion principle.* He discovered and proved that a system of n identical particles with half-integer spin, called *fermions*, has a change in sign of its wave function if any two particles are interchanged. There is also a system of n identical particles with integer spin which has a wave function that remains unchanged under the interchange of any two particles. These particles are called *bosons.* The spin-symmetry relation can be summarized as following:

Identical fermions: $\Psi(1,2) = -\Psi(2,1)$ anti-symmetric

Identical bosons: $\Psi(1,2) = +\Psi(2,1)$ symmetric

There are two types of fundamental fermions, called *quarks* and *leptons*, which were proposed as the ultimate building blocks of matter. The quarks are organized into three families of

left-handed doublets, and are labeled *u (up)* and *d (down)*, *s (strange)* and *c (charm)* , and *b (bottom)* and *t (top)*.

Quarks carry a fractional electric charge. The *up*, *charm*, and *top* quarks have an electric charge of $+\frac{2}{3}|e|$. The *down*, *strange*, and *bottom* quarks have an electric charge of $-\frac{1}{3}|e|$. A *baryon* is a bound state of three quarks; a *meson* is composed of a quark and an anti-quark. A *p (proton)*, *n (neutron)*, and Λ *(lambda hyperon)* are example of baryons. The *proton* is made of two *up* quarks and one *down* quark with a total charge of +1. A π *(pion)*, *K (kaon)*, and J/Ψ *(psi)* are examples of mesons. The π^+ is made of one *up* quark and one *anti-down* $\bar{d}$ quark with a total charge of +1. There is also π^0 with a total charge of zero made of one *up* and one *anti-up* $\bar{u}$ quark. Since quarks have a half-integer spin, it follows that baryons have a half-integer spin, and mesons have an integer spin.

Quark masses cannot be measured directly since they do not exist by themselves. Rather they are confined inside *baryons* or *mesons* and are not observed as physical particles. The *baryons* and *mesons* together are called *hadrons*. Quark masses must be determined indirectly through their interaction. Therefore, quark masses depend on how they are defined; there is no obvious choice of definition. The three quark families and their properties are shown in Table 1.1.

Like quarks, the leptons are also organized into three families in left-handed doublets. They are labeled e^- *(electron)* and ν_e *(electron neutrino)*, μ^- *(muon)* and ν_μ *(muon neutrino)*, and the more recently discovered τ^- *(tau)* and ν_τ *(tau neutrino)*. All leptons have intrinsic spin $-\frac{1}{2}$ and are therefore fermions.

Table 1.1: The three quark families.

Quark	Charge (e)	Mass (MeV/c^2)
d	$-\frac{1}{3}$	3 - 9
u	$+\frac{2}{3}$	1.5 - 5
s	$-\frac{1}{3}$	60 - 170
c	$+\frac{2}{3}$	1100 -1400
b	$-\frac{1}{3}$	4100 - 4400
t	$+\frac{2}{3}$	173800

The name lepton comes from the Greek meaning "light particle." The leptons carry integer electric charges, $\pm|e|$ or 0. The neutral leptons are called *neutrinos*, have a very small or zero rest mass, and are quite difficult to detect. In 1930, Pauli first proposed neutrinos in order to explain the observed continuous electron energy distribution in nuclear beta decay. The leptons are the most mysterious of all particles, even though their properties are well measured. Muons are like electrons in many ways, but are about 200 times heavier than electrons and are unstable particles. Table 1.2 lists lepton properties.

1.2 Fundamental Interactions

There are four fundamental interactions known in nature, namely: gravitational; electromagnetic; weak and strong interactions. The gravitational interaction is due to mass and

Table 1.2: The three lepton families.

Lepton	Charge (e)	Mass (MeV/c^2)
e	-1	0.511
ν_e	0	$< 10^{-5}$
μ	-1	105.6
ν_μ	0	< 0.17
τ	-1	1870
ν_τ	0	< 18.2

acts over infinite distance. It only has an attractive interaction since negative mass does not exist. In High Energy Physics, the gravitational interaction is a relatively unimportant effect, since its gravitational coupling, 4.6×10^{-40}, is negligibly small compared with the dimensionless fine-structure constant α, where:

$$\alpha = \frac{e^2}{4\pi\hbar c} = \frac{1}{137.0360} \ . \tag{1.1}$$

This fine-structure constant specifies the strength of the interaction between photons and charged particles.

This electromagnetic interaction is due to charge and acts over infinite distance. This interaction has either an attractive or repulsive. The basic electromagnetic process, $e^- \rightarrow e^- + \gamma$, occurs where an incoming electron is observed at the virtual vertex and emits a photon. The amplitude for this process is proportional to the charge of the electron, precisely to $\sqrt{\alpha}$, where α is the fine-structure constant that is given in above expression.

Analogous to the role of electric charge in the electromagnetic interaction, a strong charge or *color* charge plays a role in strong interactions. The gauge bosons of the strong interaction are called *gluons*, which like quarks also carry the color charge. (Colored) gluons can interact among themselves, in contrast to (neutral) photons. The fundamental coupling in strong interactions is therefore due to a color charge of both quarks and gluons. The amplitude of the strong interaction is proportional to a strong coupling constant, $\sqrt{\alpha_s}$, where α_s can be written as:

$$\alpha_s = \frac{g_s^2}{4\pi} \simeq 1 \ . \tag{1.2}$$

The strong coupling constant is about one hundred times that of the fine-structure constant. The strong interaction acts over a short distance, $\sim 10^{-15}\ m$.

At a fundamental level, neutron decay, $n \rightarrow p + e^- + \bar{\nu_e}$, requires a quark flavor change. In this process, the incoming *down* quark in a *neutron* is absorbed and an *up* quark in the *proton* is emitted along with an intermediate weak gauge boson, in this case the W^- boson. Then the W^- decays to an electron and its anti-neutrino. In this case, the leptons couple to the weak gauge boson, W^-, not directly to the quarks. The amplitude of this process is proportional to $\sqrt{\alpha_w}$, with $\alpha_w \simeq 4\ \alpha$. The weak interaction is due to a weak charge and acts over a very short distance, $\sim 10^{-18}\ m$. There are three kinds of known weak gauge bosons; W^-, W^+ and Z^0. The weak interaction is the only interaction which does not conserve parity. Neutrinos are always left-handed and anti-neutrinos are always right-handed. The basic characteristics of the gravitational, electromagnetic, strong, and weak interactions are enumerated in Table 1.3.

Table 1.3: Characteristics of the charge carries of the fundamental interactions.

Propagator	Interaction	Source	Mass (GeV/c^2)	Charge	Range (m)
G	Gravitational	Mass	0	0	∞
γ	Electromagnetic	Electric Charge	0	0	∞
g	Strong	Color Charge	0	0	10^{-15}
$W^{\pm}$	Weak	Weak Charge	80.41	± 1	10^{-18}
Z^0	Weak	Weak Charge	91.187	0	10^{-18}

1.3 Standard Model

In the Standard Model, the only neutrino which interacts is left-handed and massless. The charged quarks and massive leptons can be either left-handed or right-handed. The fundamental constituents of matter are point-like fermions, leptons and quarks. The four fundamental interactions have quite different coupling constants which gives rise to different cross sections. At extremely high energy, the coupling constants may converge to a single quantity which can be explained in terms of a *single unified field*. Glashow, Weinberg and Salam [1] unified the weak and electromagnetic interactions. This great discovery reinforced the belief in an existence of a single unified theory of the fundamental interactions.

The most significant theoretical assumption toward unification is that all fundamental interactions are invariant under local gauge transformations. Theorists realized that gauge theories would provide a basis for a unification of the fundamental interactions.

The interactions between the fundamental particles are described by renormalizable gauge theory. The requirement that the free-particle Lagrangian be invariant under $SU(3)_{color} \times SU(2)_L \times U(1)_Y$ gauge transformation introduces 12 gauge bosons (there are eight gluons, W^+, W^-, Z^0 and photon) and determines the form of their interactions with the fermions.[1]

The fermion-gauge boson Lagrangian of the Standard Model can be written as:

$$\begin{aligned}
\mathcal{L} &= -\frac{1}{4}\mathbf{W}_{\mu\nu}\cdot\mathbf{W}^{\mu\nu} - \frac{1}{4}B_{\mu\nu}B^{\mu\nu} - \frac{1}{4}G^a_{\mu\nu}G^{\mu\nu}_a \\
&+ \bar{L}\gamma^\mu(i\partial_\mu - \frac{1}{2}g\tau\cdot\mathbf{W}_\mu - \frac{1}{2}g'YB_\mu)L \\
&+ \bar{R}\gamma^\mu(i\partial_\mu - \frac{1}{2}g'YB_\mu)R \\
&+ |(i\partial_\mu - \frac{1}{2}g\tau\cdot\mathbf{W}_\mu - \frac{1}{2}g'YB_\mu)\varphi|^2 - V(\varphi) \\
&- (g_1\bar{L}\varphi R + g_2\bar{L}\tilde{\varphi}R + h.c.) \\
&+ \frac{1}{2}g_s(\bar{\psi}^j_q\gamma^\mu\lambda^a_{jk}\psi^k_q)G^a_\mu
\end{aligned} \tag{1.3}$$

The first row is $W^\pm$, Z^0, γ and gluon kinetic energies and self-interactions. The second and third rows are the lepton and quark kinetic energies and their interactions with $W^\pm$, Z^0 and γ. The fourth row is the masses and coupling of the $W^\pm$, Z^0, γ and Higgs boson. The fifth row determines the lepton and quark masses and coupling to the Higgs boson and the last row determines the quark-gluon couplings. In this Lagrangian, L represents a left-handed fermion (lepton or quark) doublet, R represents a right-handed fermion singlet, φ is the Higgs doublet, and ψ^j_q represents a quark color field.

[1] $U(1)_Y$ represents Quantum Electrodynamics (QED), $SU(2)_L$ represents Weak Interaction, and $SU(3)_{color}$ for Quantum Chromodynamics (QCD).

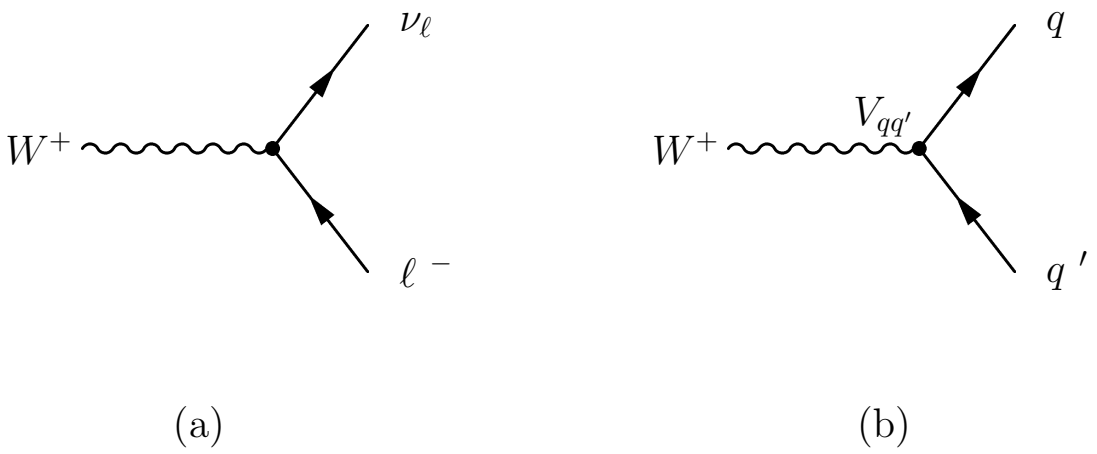

Figure 1.1: In (a) the W couples to the lepton doublets, and in (b) to the quark doublets.

1.4 Charged Current Weak Interactions

The Standard Model has successfully explained both a leptonic weak current and a hadronic weak current. The first description of the weak process was generalized by Feynman and Gell-Mann [6]. Figure 1.1 shows the weak charged current involving a W boson, for leptons and quarks.

In terms of all three quark and lepton generations, the leptonic charged current can be written as:

$$J_\mu^+ = (\bar{\nu}_e, \bar{\nu}_\mu, \bar{\nu}_\tau)\,\frac{1}{2}\,\gamma_\mu\,(1-\gamma^5)\begin{pmatrix} e \\ \mu \\ \tau \end{pmatrix}\,. \tag{1.4}$$

and the hadronic charged current as:

$$J_{\mu}^{+} = (\bar{u}, \bar{c}, \bar{t}) \frac{1}{2} \gamma_{\mu} (1 - \gamma^{5}) \begin{pmatrix} d' \\ s' \\ b' \end{pmatrix} \tag{1.5}$$

In the Standard Model, all quark and lepton generations are grouped into three weak isospin left-handed doublets as:

Quark Isospin Left-handed Doublets

$$\begin{pmatrix} u \\ d \end{pmatrix} \begin{pmatrix} c \\ s \end{pmatrix} \begin{pmatrix} t \\ b \end{pmatrix} \tag{1.6}$$

Lepton Isospin Left-handed Doublets

$$\begin{pmatrix} e \\ \nu_e \end{pmatrix} \begin{pmatrix} \mu \\ \nu_{\mu} \end{pmatrix} \begin{pmatrix} \tau \\ \nu_{\tau} \end{pmatrix} \tag{1.7}$$

The charged leptons have both electromagnetic and weak interactions, and the neutrinos only have a weak interaction with other particles. However, the quarks not only have electromagnetic and weak interactions, but also have the strong interaction.

In the Standard Model, the interchange of leptons between families is not allowed and these observations are formalized by the introduction of three conserved quantities, Lepton Family Number; L_e for electron family, L_{μ} for μ family, and L_{τ} for τ family. In this model with $SU(2) \times U(1)$ as the gauge group of electroweak interactions, the quark mass eigenstates are not the same as the weak interaction eigenstates. However, the weak interaction eigenstates

can be related to the quark mass eigenstates by a 3×3 unitary matrix called the Cabibbo-Kobayashi-Maskawa (CKM) matrix [7]. The CKM matrix can be regarded as a rotation from the quark mass eigenstates (namely d, s, and b) to a set of new states (d', s', and b') with diagonal weak couplings to u, c, and t.

By convention, the CKM matrix can be written as:

$$V_{CKM} = \begin{pmatrix} V_{ud} & V_{us} & V_{ub} \\ V_{cd} & V_{cs} & V_{cb} \\ V_{td} & V_{ts} & V_{tb} \end{pmatrix} \tag{1.8}$$

and the correlation of weak interaction eigenstates to the quark mass eigenstates is

$$\begin{pmatrix} d' \\ s' \\ b' \end{pmatrix} = \begin{pmatrix} V_{ud} & V_{us} & V_{ub} \\ V_{cd} & V_{cs} & V_{cb} \\ V_{td} & V_{ts} & V_{tb} \end{pmatrix} \begin{pmatrix} d \\ s \\ b \end{pmatrix} , \tag{1.9}$$

For example, the element V_{ud} specifies the coupling of the u and d quarks in the process: $d \rightarrow u + W^-$. The off-diagonal elements of the CKM matrix are not exactly zero, leading to the generation-changing transitions between quarks.

The CKM matrix can be parameterized in various ways. One way which is recommended by The Particle Data Group [8] is:

$$V_{CKM} = \begin{pmatrix} c_1 & c_3 s_1 & s_1 s_3 \\ -s_1 c_2 & c_1 c_2 c_3 - s_2 s_3 e^{i\delta} & c_1 c_2 s_3 + c_3 s_2 e^{i\delta} \\ s_1 s_2 & -c_1 c_3 s_2 - c_2 s_3 e^{-i\delta} & -c_1 s_2 s_3 + c_2 c_3 e^{i\delta} \end{pmatrix} , \tag{1.10}$$

where the $c_i = \cos\theta_i$ and $s_i = \sin\theta_i$ for $i = 1, 2, 3$. In the limit, where $\theta_2 = \theta_3 = 0$, this reduces to the usual Cabibbo mixing with θ_1 identified (up to a sign) with the Cabibbo angle, θ_C [9]. Empirically, Wolfenstein [10] suggested the hierarchy motivation of the CKM matrix in terms of a small parameter and the Cabibbo angle, θ_C. One sets $\lambda \equiv s_{12} = \sin\theta_C \simeq 0.22$, the sine of the Cabibbo angle, then writes the other elements: A, η, and ρ in terms of powers of λ. The A, η, and ρ are real numbers that were intended to be order unity. The requirement of unitarity constrains the elements to only four independent parameters: A, λ, ρ, and η. The CKM matrix can then be written in the explicit form to order λ^3 as:

$$V_{CKM} \approx \begin{pmatrix} 1 - \frac{1}{2}\lambda^2 & \lambda & A\lambda^3(\rho - i\eta) \\ -\lambda & 1 - \frac{1}{2}\lambda^2 & A\lambda^2 \\ A\lambda^3(1 - \rho - i\eta) & -A\lambda^2 & 1 \end{pmatrix}. \tag{1.11}$$

One condition of unitarity is that the scalar product of any two rows or columns of the CKM matrix equals zero as:

$$V_{ub}^* V_{ud} + V_{cb}^* V_{cd} + V_{tb}^* V_{td} = 0, \tag{1.12}$$

This equation is represented in Figure 1.2. When the lengths of two sides are normalized in such a way so that the base is a unit length, and the lower left corner is placed at the origin of the complex plane.

It is important to measure the magnitudes of all the interior angles and the lengths of all the sides to ensure consistency within the Standard Model. The length of the base is defined by the value of $|V_{cb}|$ and $|V_{cd}|$. The value of $|V_{cb}|$ can be measured in decays of the type $b \to c\ell\nu$. The side opposite to angle γ is defined by the value of $|V_{td}|$ and $|V_{tb}|$. The value of $|V_{td}|$

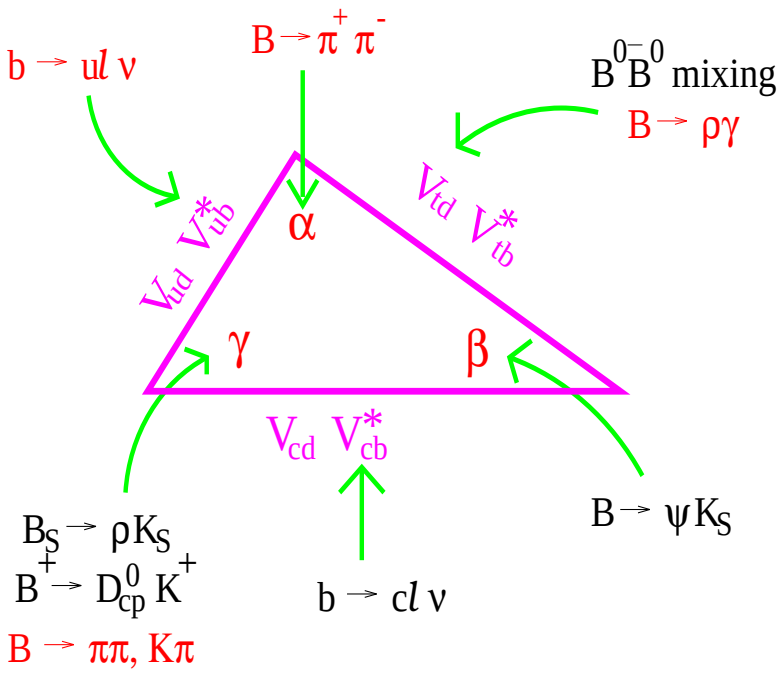

Figure 1.2: Unitarity triangle in complex plane and schematic decay modes.

can be determined through measurements of the neutral B mixing rate. The side opposite to angle β is defined by the value of $|V_{ub}|$ and $|V_{ud}|$. The value of $|V_{ub}|$ can be measured in decays of the type $b \to u\ell\nu$.

The angle γ gives the phase of $|V_{ub}|$, and can be measured with a variety of decays as shown in Figure 1.2. The angle β gives the phase of the mixing, and can be measured with the decay $B \to \psi K_S$. The angle α is defined by the angle β and γ within the Standard Model. It can be measured with the decay $B \to \pi^+\pi^-$.

Chapter 2

B Meson Physics

The first evidence of the b-quark was obtained at Fermilab in the Υ bound states in a fixed-target experiment in 1977 by Lederman and coworkers [12]. The narrow Υ-resonance showed up in the mass distribution of muon pairs in the reaction $p + Be \to \mu^+\mu^- + X$. This resonance was identified as the 1^3S_1 state of $b\bar{b}$ system. Immediately after its discovery, the study of the b-quark was continued at e^+e^- storage rings. A year after its discovery, a single ring DORIS II at DESY reached the two lowest Υ states, namely $\Upsilon(1S)$ and $\Upsilon(2S)$ [13]. In 1980, the Cornell Electron Storage Ring, CESR, at Cornell University found the $\Upsilon(3S)$ and $\Upsilon(4S)$ [14]. The current knowledge of B mesons with large statistics is based on three different colliders: CESR (Cornell, USA), producing $B\bar{B}$ in decays of the $\Upsilon(4S)$ resonance just above $e^+e^- \to B\bar{B}$ threshold; LEP (CERN, Switzerland), producing $b\bar{b}$ pairs in Z^0 boson decays; and TEVATRON (Fermilab, USA), producing $b\bar{b}$ in $p\bar{p}$ collisions. The CLEO experiment has the largest b-hadron data sample, with over 9 million $\Upsilon(4S) \to B\bar{B}$ events.

In recent years, multibunch operation has been one of the most important advantages in producing high luminosity in the storage rings. Currently CESR operates with 27 bunches of electrons and 27 bunches of positrons. There are two new machines which have a huge increase in the number of bunches: KEKB in Japan has 5000 bunches/beam [15] and PEP-II at SLAC has 1658 bunches/beam [16]. On May 26, 1999, BABAR experiment detected its first colliding beam events, with PEP-II running at a luminosity above $10^{31}\ cm^{-2}s^{-1}$ and BELLE detected its first hadronic event candidate on June 1, 1999.

2.1 *B* Meson Production

A year after the Υ bound states were discovered, the B meson was extensively studied. Figure 2.1 shows the four Υ states which were clearly identified by CESR. These are the lowest-lying S states of the $b\bar{b}$ system. The three lowest states, $\Upsilon(1S)$, $\Upsilon(2S)$, and $\Upsilon(3S)$, are below the mass threshold of the $b\bar{b}$ production. This greatly limits their hadronic widths and they decay through OZI-suppressed strong decay [17], therefore displaying a narrower resonance compared to the fourth broad resonance, $\Upsilon(4S)$. The fourth resonance has a sufficient mass to create a light quark pair ($u\bar{u}$ or $d\bar{d}$) and produce a $B^0\bar{B}^0$ or B^+B^- pair, which results in its broader width. The mass for $\Upsilon(4S)$ is about 22 MeV above a $B^0\bar{B}^0$ or B^+B^- pair with no additional pions nor any other types of b hadrons produced. Figure 2.2 shows the mechanism for $B\bar{B}$ production in e^+e^- collisions at the $\Upsilon(4S)$ resonance.

The $\Upsilon(4S)$ cross section is about 1.07 nb [18] with an additional 3 nb contribution to the

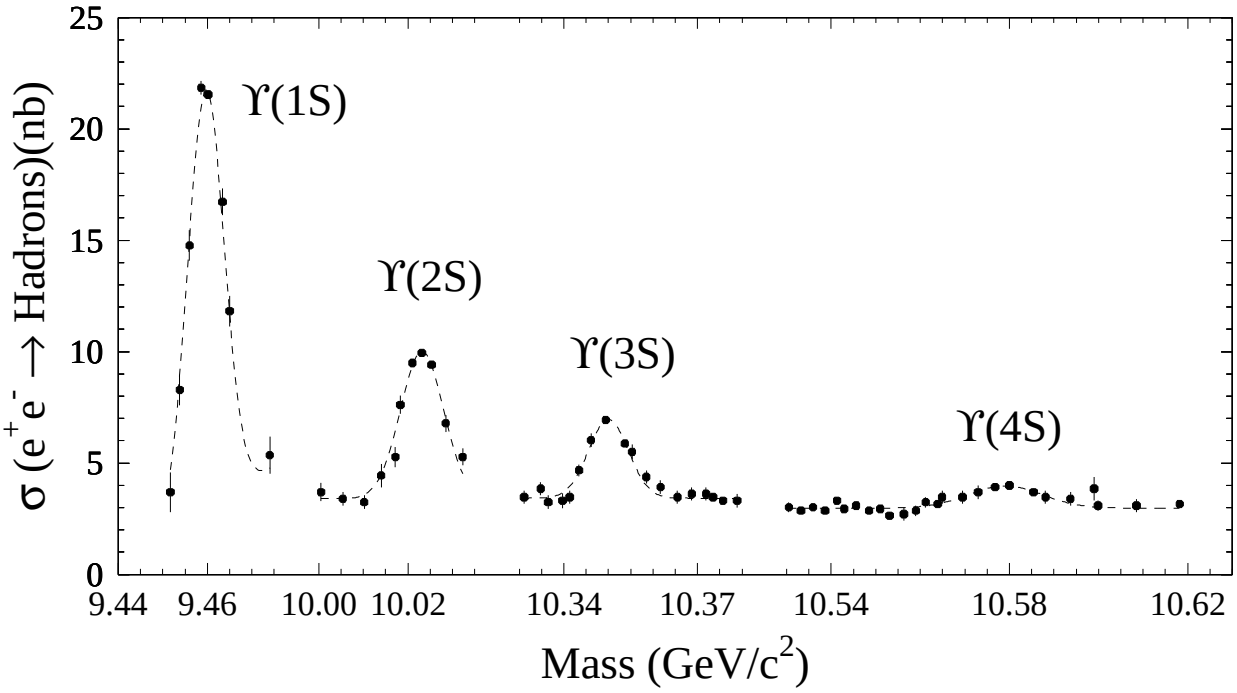

Figure 2.1: The total cross section for $e^+e^- \rightarrow$ *hadrons* showing the $\Upsilon(1S)$, $\Upsilon(2S)$, $\Upsilon(3S)$ and $\Upsilon(4S)$ states. The masses of these states are 9460, 10023, 10355, and 10580 MeV/c^2 and the total widths are 52 keV/c^2, 43 keV/c^2, 24 keV/c^2, and 24 MeV/c^2, respectively.

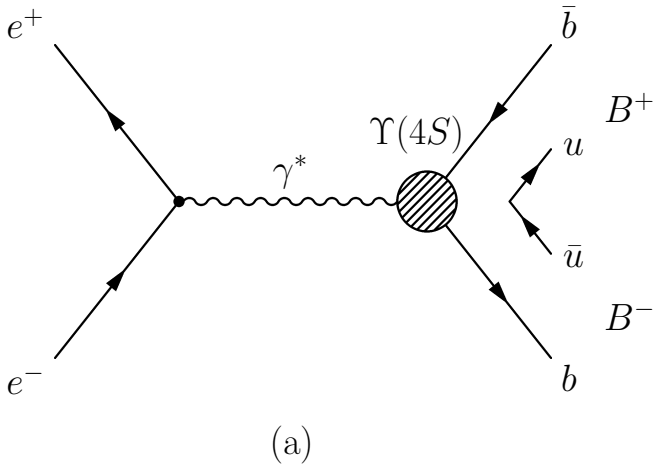

(a)

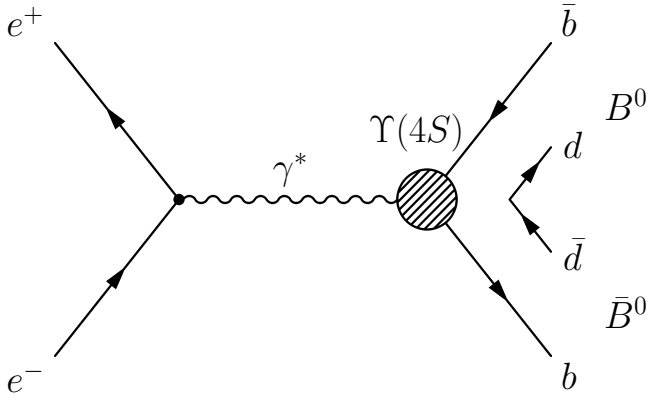

(b)

Figure 2.2: The mechanism for $B\bar{B}$ production in e^+e^- collisions at the $\Upsilon(4S)$ resonance. In (a) $\Upsilon(4S) \to \gamma^* \to B^+B^-$ and in (b) $\Upsilon(4S) \to \gamma^* \to B^0\bar{B}^0$.

total hadronic cross section from continuum events. The continuum events are a non-resonant decay of $e^+e^- \to \gamma^* \to q\bar{q}$ where $q = u, d, s, c$. The relative cross section of $e^+e^- \to \Upsilon(4S)$ with $e^+e^- \to q\bar{q}$ hadronization at $\sqrt{s} = 10.58$ GeV/c^2 can be written as:

$$\frac{\sigma(e^+e^- \to \Upsilon(4S))}{\sigma(e^+e^- \to q\bar{q})} \simeq \frac{1}{3} \ . \tag{2.1}$$

Continuum events are generally collimated into two back-to-back jets and $\Upsilon(4S) \to B\bar{B}$ events are much more isotropic. The spherical topology of the $\Upsilon(4S) \to B\bar{B}$ events are due to a very low B meson momentum, $P_B \simeq 340\ MeV/c$, in the $\Upsilon(4S)$ rest frame. The spherical shape of $B\bar{B}$ events gives an advantage in separating them from continuum events. Due to their low momenta, however, it is a difficult task to associate the correct daughter tracks with the correct B meson, since the two B mesons are close together.

The lifetime of a b baryon can be measured with relativistic time dilation at a high b momentum that gives a measurable flight distance. The b baryon lifetime, which is related to its decay length, L_b, can be written as:

$$\tau_b = \frac{L_b}{\gamma\beta c} \ . \tag{2.2}$$

The world averages of the B^+ lifetime[1] is $\tau(B^+) = 1.67 \pm 0.03\ ps$ [19].

Figure 2.3 shows an example of an $e^+e^- \to \Upsilon(4S) \to B\bar{B}$ event and Figure 2.4 shows an example of an $e^+e^- \to q\bar{q}$ event.

CLEO spends one-third of its time running at a center-of-mass energy about 60 MeV below

[1]Charge conjugation is implied throughout this thesis.

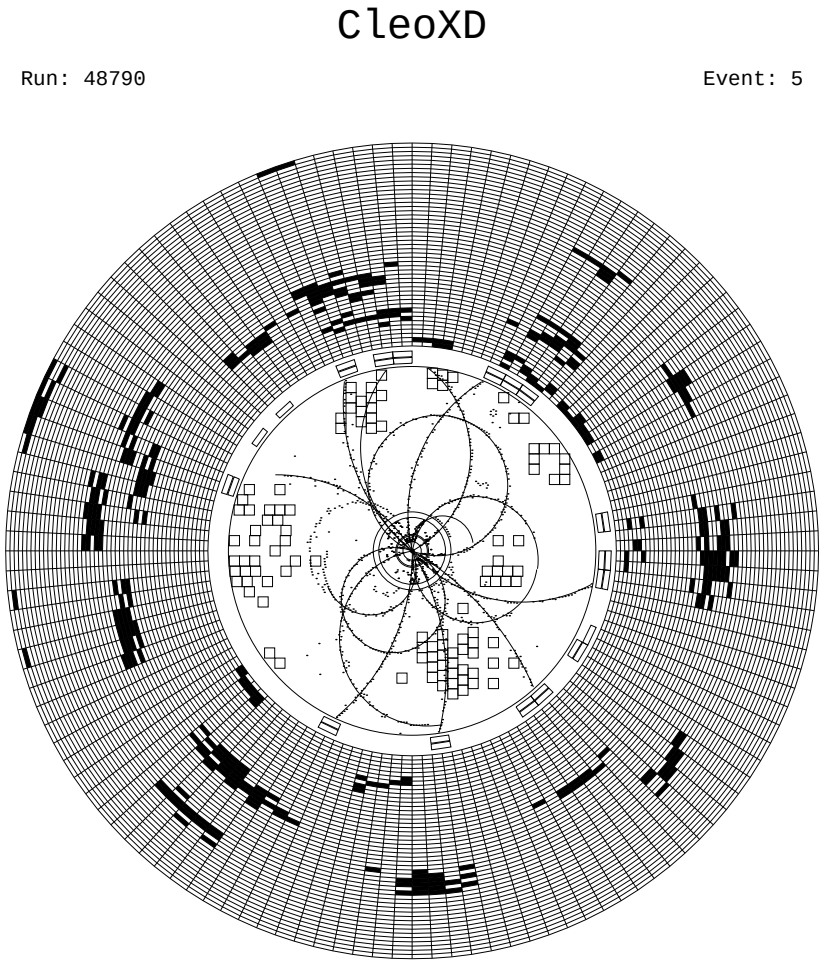

Figure 2.3: An example of an $e^+e^- \to \Upsilon(4S) \to B\bar{B}$ event.

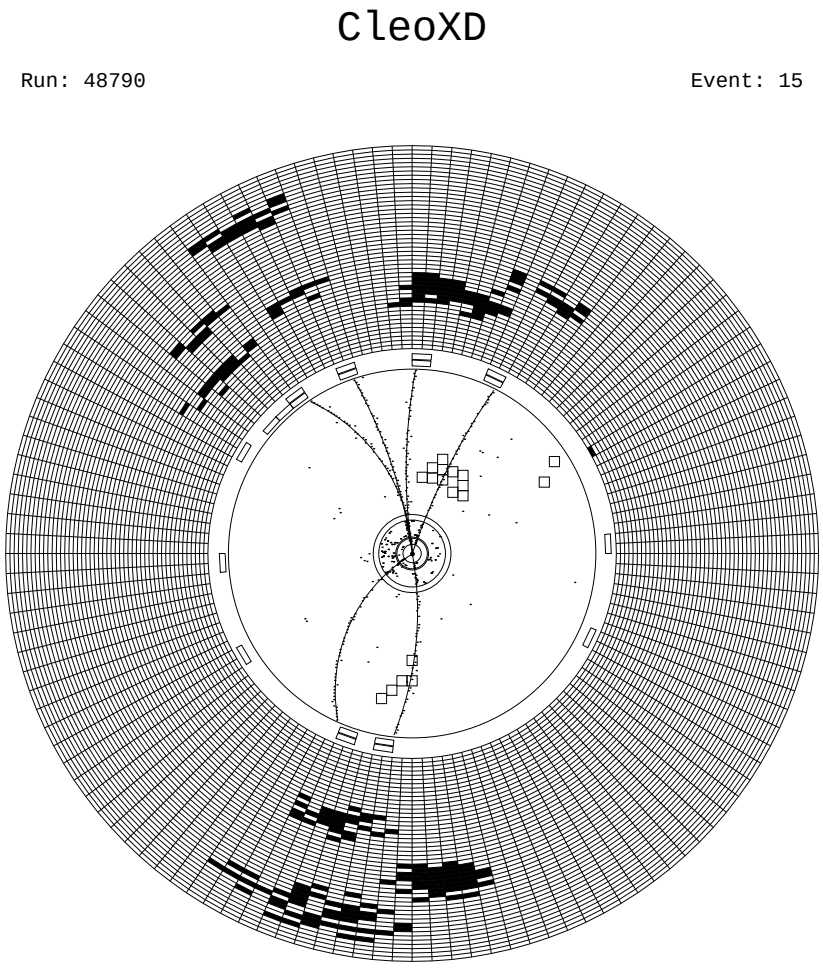

Figure 2.4: An example of an $e^+e^- \to q\bar{q}$ event.

the $\Upsilon(4S)$ resonance. The continuum background can be subtracted using both a selection cut based on the overall event shape and by measuring the continuum background. The continuum background scaling factor, $\lambda_{continuum}$, can be estimated using the following expression:

$$\lambda_{continuum} = \frac{\mathcal{L}_{on}}{\mathcal{L}_{off}} \frac{E_{off}^2}{E_{on}^2} \ . \tag{2.3}$$

where $\mathcal{L}_{on}$ and $\mathcal{L}_{off}$ are the total luminosity at and below the $\Upsilon(4S)$ resonance and E_{on} and E_{off} are the CESR beam energies, respectively. After scaling the off resonance data by this scaling factor to correct for the differences in integrated luminosity and center of mass energy, then the continuum backgrounds are subtracted from the $\Upsilon(4S)$ resonance data. This leaves only events from B meson decays.

2.2 The Relative $B\bar{B}$ Production Rates at $\Upsilon(4S)$

All the branching fraction measurements for an admixture of B mesons at the $\Upsilon(4S)$ assume that $\mathcal{B}(\Upsilon(4S) \to B\bar{B}) = 100\%$ [5]. To be able to get better precision measurements of all the branching fractions of $\Upsilon(4S) \to B\bar{B}$ mesons decay, the measurement of the ratio of the production of charged and neutral B mesons at the $\Upsilon(4S)$ resonance is necessary.

The mass of the $\Upsilon(4S)$ resonance at 10.580 GeV is just about 22 MeV above the $B\bar{B}$ threshold. Therefore, the momentum of B mesons produced from $\Upsilon(4S)$ decay is very small, $|\vec{P}_B| \simeq 340\ MeV/c$. The relatively large $\Upsilon(4S)$ width of 24 MeV implies that the production of $B\bar{B}$ on the $\Upsilon(4S)$ saturates its decay. The B meson velocity in the $\Upsilon(4S)$ rest frame is

small [31]:

$$\beta = \sqrt{1 - \frac{4m_B^2}{m_{\Upsilon(4S)}^2}} \approx 0.065 \ , \tag{2.4}$$

where m_B and $m_{\Upsilon(4S)}$ are the mass of the B meson and the $\Upsilon(4S)$ resonance, respectively.

The production of B mesons is quite non-relativistic. One can therefore calculate the dominant Coulomb correction using non-relativistic time-dependent perturbation theory. In the non-relativistic limit, $\beta \ll 1$, the Coulomb correction factor, C_{corr}, can be expressed as [36]:

$$C_{corr} = \frac{\left(\frac{2\pi\alpha}{\beta_{rel}}\right)}{\left[1 - e^{\frac{-2\pi\alpha}{\beta_{rel}}}\right]} \ , \tag{2.5}$$

where C_{corr} is the Coulomb correction factor, $\beta_{rel} \approx 2\beta$, and α is the fine-structure constant.

The Coulomb corrections between the final state B mesons in $\Upsilon(4S) \to B^+B^-$ production, however, are quite large. They enhance the $\Upsilon(4S) \to B^0\bar{B}^0$ production rate by a factor $(1 + \frac{\pi\alpha}{2\beta})$. In a certain limit, by not including $B^+ - B^0$ mass splitting [37] or isospin-violating form factors in the decay amplitude and treating the mesons as point-like particles, the Coulomb corrections imply an 18% enhancement as:

$$\frac{\Gamma(\Upsilon(4S) \to B^+B^-)}{\Gamma(\Upsilon(4S) \to B^0\bar{B}^0)} \approx 1.18 \ , \tag{2.6}$$

By not considering the $\Upsilon(4S)$ and B meson as point-like particles, however, but rather requiring models for the form factors and vertex function, the Coulomb correction is reduced from 18% to 14%. Furthermore, using the $\Upsilon(4S)$ wave function rather than the B meson wave function, the Coulomb correction is reduced from 18% to 3%. The last calculation used the Cornell quark potential model [38] to compute the $\Upsilon(4S)$ wave function.

In this thesis, we present result of the measurement of the ratio of charged and neutral B mesons in $\Upsilon(4S)$ events via partial reconstruction. We use the semileptonic decays $\bar{B}^0 \to D^{*+}\ell^-\bar{\nu}_\ell$ and $B^- \to D^{*0}\ell^-\bar{\nu}_\ell$ to extract the ratio of the product of production fraction and lifetime for charged and neutral B mesons, $\frac{f_{+-}\tau_+}{f_{00}\tau_0}$.

2.3 Semileptonic B Decay

2.3.1 Dynamics of Quark Decays

In the Standard Model, the decays of the b quark to the t quark and virtual W^- boson are kinematically forbidden to first order; therefore the decays of a b quark to a c or u quark and a virtual W^- boson that turns into a pair of leptons or a pair of quarks is a dominant decay of b quarks.

Due to the value of the quark masses, an *up*-type quark (u, c, t) can only decay to a *down*-type quark (d, s, b) partner within the same generation as a dominant decay. These decays probe the diagonal CKM matrix elements that are known to be close to unity. These decays make the *up*-type quarks have a relatively short lifetime compared to the *down*-type quarks. The dominant decays of heavy *down*-type quarks change the quark generation. The decays of *up*-type quarks to the quarks of other generations are rare and difficult to observe. Figure 2.5(a) and Figure 2.5(b) show the schematics decays of the *up*-type and the *down*-type quarks according to the Standard Model [20]. The simplest model for B meson decay is

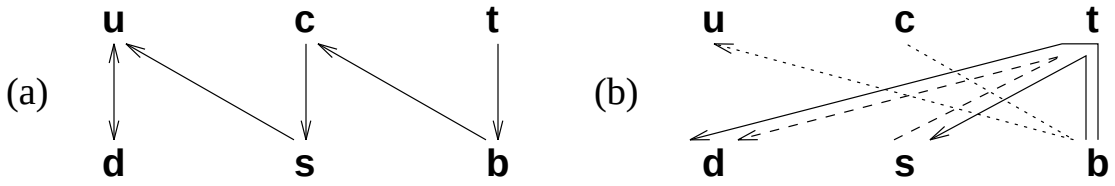

Figure 2.5: Standard Model decays of quarks. (a) first order decays. (b) second order decays.

known as the spectator model, since the light quark in the initial hadron does not participate in the short distance disintegration of the b quark. Figure 2.6(a) shows the spectator model. This is known as a spectator model in semileptonic B decay if the virtual W^- boson decays to a lepton-antineutrino pair. If the virtual W^- boson decays to a quark-antiquark pair instead, this is called the spectator model in hadronic B decay. The decays of the b quark to the c quark are strongly favored by the value of the CKM elements where $|V_{cb}|^2/|V_{ub}|^2 \simeq 10^2$. Figure 2.6(b), (c) and (d) shows the possibilities of quark-level first order Feynman diagrams. The second order is a more complicated decay model where the b quark can decay to virtual t quark and W^- boson that immediately recombine to the s quark. To conserve the energy, a gluon must be emitted. This complicated decay known as a loop or penguin decay is shown in Figure 2.6(e).

2.3.2 Understanding Semileptonic Decays

There are several motivations why semileptonic B decays play a prominent role in testing the Standard Model. First of all, semileptonic decays are the simplest model to understand via the spectator model, where the heavy b quark decays to either a c or u quark and a

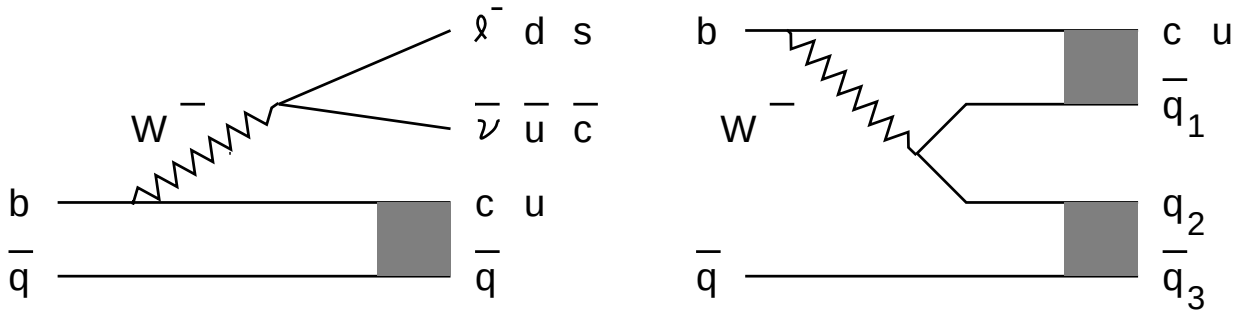

(a) Spectator

(b) Color Mixed

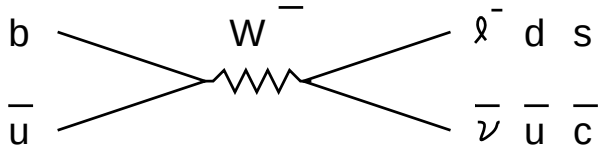

(c) Annihilation

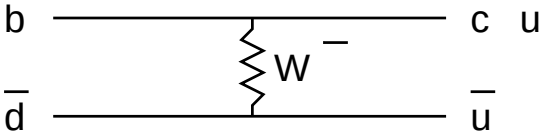

(d) Exchange

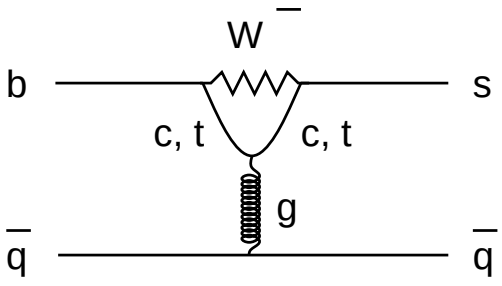

(e) Penguin

Figure 2.6: Quark-level Feynman diagram for B decays:(a) spectator, (b) color mixed, (c) annihilation, (d) exchange, and (e) penguin.

lepton pair created from the virtual W boson. Secondly, the total decay rates, also known as branching fractions, are relatively large. Finally, the flavor of the B meson can be indicated from the charge of the lepton. More precisely, a positive charge of the lepton indicates a B meson with a $\bar{b}$ quark, whereas a negative charge of the lepton indicates a B meson with a b quark.

In semileptonic transitions, however, it is impossible to do a full reconstruction of the decaying B meson due to an undetected neutrino. Measurements of semileptonic B decays are used to determine two of the three sides of the unitary triangle, $|V_{cb}|$ and $|V_{ub}|$. CLEO, ARGUS, and LEP collaborations have made great contributions in determining the value of $|V_{cb}|$ and $|V_{ub}|$, using various techniques which take advantage of B meson decays.

The differential rate for semileptonic $\bar{B}$ meson decay is given by [21]:

$$d\Gamma(\bar{B} \to X\ell\bar{\nu}_\ell) = |V_{cb}|^2 d\hat{\Gamma}(\bar{B} \to X_c\ell\bar{\nu}_\ell) + |V_{ub}|^2 d\hat{\Gamma}(\bar{B} \to X_u\ell\bar{\nu}_\ell) \ , \tag{2.7}$$

where the lepton, ℓ, refers to an electron (e) or a muon (μ). Although τ leptons are also produced, the much greater τ mass suppresses the decay rate. The function $d\hat{\Gamma}(\bar{B} \to X_q\ell\bar{\nu}_\ell)$ denotes the contribution to the differential rate, $d\Gamma(\bar{B} \to X\ell\bar{\nu}_\ell)$. Using an experimental lepton spectrum and predicted values of the functions $d\hat{\Gamma}(\bar{B} \to X_u\ell\bar{\nu}_\ell)$ and $d\hat{\Gamma}(\bar{B} \to X_c\ell\bar{\nu}_\ell)$, one can determine the ratio $|V_{ub}|^2/|V_{cb}|^2$. Furthermore, the absolute semileptonic decay rate can be used to determine values of the weak-mixing angles as shown in Figure 1.2.

In the free-quark decay model where the b quark decays freely from rest, the inclusive

semileptonic $\bar{B}$ meson decay rate can be written as [21]:

$$\Gamma(\bar{B} \to X_q \ell \bar{\nu}_\ell) = \frac{G_F^2 m_b^5}{192\pi^3} |V_{qb}|^2 F(x = m_q/m_b) \ , \tag{2.8}$$

where G_F is the Fermi constant, m_b is the b quark mass and the phase factor $F(x)$ is given by:

$$F(x) = 1 - 8x^2 + 8x^6 - x^8 - 24x^4 \ln x \ . \tag{2.9}$$

This phase factor is close to unity for $\bar{B} \to X_u \ell \bar{\nu}_\ell$ such as in the decay $\bar{B} \to D \ell \bar{\nu}_\ell$. For $\bar{B} \to X_c \ell \bar{\nu}_\ell$, such as in the decay $\bar{B} \to D^* \ell \bar{\nu}_\ell$, the value of this phase factor is approximately 0.5.

In this thesis, we discuss $b \to c$ decays, so that we can ignore the second part of Equation 2.7. Then the differential decay rate, $\bar{B} \to D^* \ell^- \bar{\nu}_\ell$, in the B meson rest frame can be given as [21]:

$$d\Gamma(\bar{B} \to D^* \ell^- \bar{\nu}_\ell) = \frac{1}{(2\pi)^3} \frac{1}{32 m_B^3} |M|^2 d\Pi^3 \ , \tag{2.10}$$

where the $d\Pi^3 = dq^2 dt$ is the three-body phase space factor and $q^2 = (k' - k)$.

The matrix element M can be expressed in terms of the well-known leptonic current, L^μ, the hadronic matrix element of the weak current, H_μ, and the CKM matrix element, V_{cb}, as:

$$M = \frac{G_F}{\sqrt{2}} V_{cb} L^\mu H_\mu \ , \tag{2.11}$$

The leptonic and hadronic currents are given by:

$$L^\mu = \bar{u}_\ell(p) \gamma^\mu (1 - \gamma_5) v_{\nu_\ell}(p') \tag{2.12}$$

$$H_\mu = \langle D^*(k) | V_{had}^\mu - A_{had}^\mu | \bar{B}(k') \rangle \ , \tag{2.13}$$

where p and p' are the four-momenta of the lepton and the associated neutrino; k and k' are the four momenta of the B meson and the D^* meson, respectively.

The effect of strong interactions may be rigorously parameterized into a set of Lorentz-invariant quantities called *form factors* that depend on the squared four-momentum transfer q^2. Figure 2.7 shows the kinematics of semileptonic B decays, $\bar{B} \to D^* \ell \bar{\nu}_\ell$ where $D^* \to D\pi$. The value of θ_ℓ is the angle of the lepton in the W boson rest frame with respect to the direction of the W in the B meson rest frame. The value of θ^* in the plane of $\ell, \bar{\nu}_\ell$ is the angle of the D meson in the D^* rest frame with respect to the direction of the D^* meson in the B rest frame. The value of χ is the angle between the $D\pi$ plane and $\ell\bar{\nu}_\ell$ plane. The value of the squared momentum transfer q^2 in the B rest frame can be expressed as:

$$q^2 = m_W^2 = (P_\ell + P_{\bar{\nu}_\ell})^2 = (P_B - P_{D^*})^2 = m_B^2 + m_{D^*}^2 - 2\, m_B\, E_{D^*} \ , \tag{2.14}$$

where E_{D^*} is the energy of the D^* meson in the B rest frame and m_B and m_{D^*} are the mass of the B and the D^* meson, respectively. The four-velocity transfer $w = (v_B \cdot v_{D^*})$ can be written in terms of q^2 as:

$$w = \frac{m_B^2 + m_{D^*}^2 - q^2}{2\, m_B\, m_{D^*}} \ . \tag{2.15}$$

The quantity w is just the relativistic γ factor of the D^* in the B rest frame.

The V-A leptonic current at the W boson vertex is calculable, and the matrix element in the hadronic current, H_μ, cannot be calculated perturbatively, since the two bound states B and D^* meson involve non-perturbative QCD.[2] The hadronic current can be estimated

[2]QCD represents quantum chromodynamics, which describes the strong interaction.

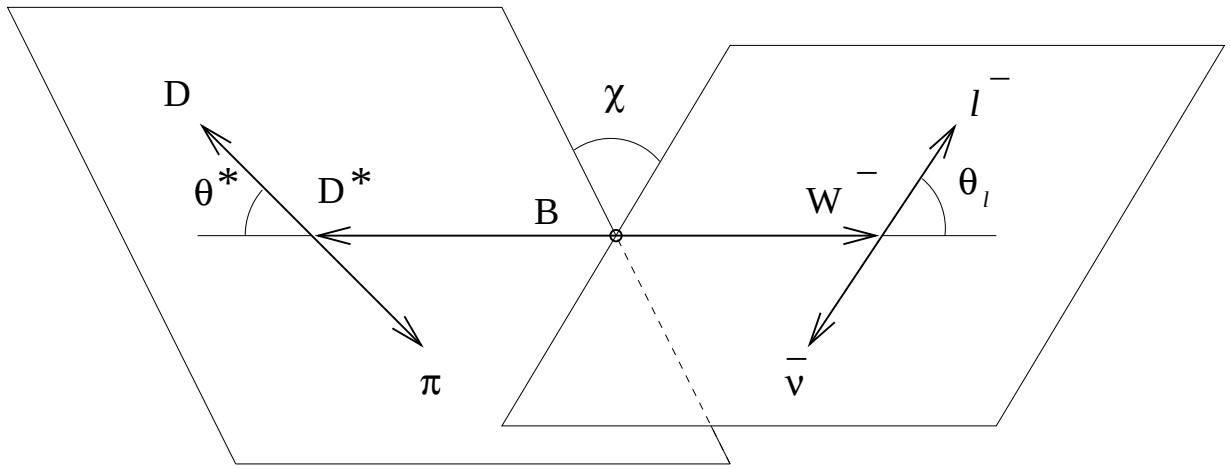

Figure 2.7: Illustration of angles in the decay $\bar{B} \to D^* \ell \bar{\nu}_\ell$, with $D^* \to D\pi$ in the B rest frame.

theoretically in a certain limit of QCD such as the heavy quark limit. In this limit, however, one treats the bound states as ideal structure particles, then does a heavy-quark expansion calculation for inclusive decays and a reliable heavy-quark effective theory (HQET) for exclusive decays. Therefore, semileptonic decay measurements may be used to determine V_{cb} or V_{ub} by giving some model for the hadronic current, H_μ. If V_{cb} or V_{ub} can be determined instead, one can then test models for H_μ.

2.4 Theory of $\bar{B} \to D^* \ell^- \bar{\nu}_\ell$ Decay

The hadronic current, H_μ, for decay $P \to V \ell \bar{\nu}_\ell$ where P is a *Pseudo-scalar* (B) meson and V is a *Vector* (D^*) meson, is expressed [21],[22] in terms of vector and axial vector current as:

$$H_\mu = \langle D^*(k,\varepsilon)|V^\mu_{had} - A^\mu_{had}|\bar{B}(k')\rangle$$

$$
\begin{aligned}
&= i\epsilon_{\mu\nu\rho\sigma}\varepsilon^{*\nu}(k'+k)^{\rho}(k'-k)^{\sigma}\frac{V(q^2)}{m_B+m_{D^*}} \\
&- (m_B+m_{D^*})\varepsilon^{*}_{\mu}A_1(q^2) - (\varepsilon^{*}\cdot k')(k'+k)_{\mu}\frac{A_2(q^2)}{m_B+m_{D^*}} \\
&+ (\varepsilon^{*}\cdot k')(k'-k)_{\mu}\frac{A_3(q^2)}{m_B+m_{D^*}} \ , \qquad (2.16)
\end{aligned}
$$

where ε^* is the polarization vector of the D^* meson, m_{D^*} is the mass of the D^* meson, and m_B is the mass of the B meson. The Lorentz-invariant form factors ($V(q^2)$, $A_1(q^2)$, $A_2(q^2)$, and $A_3(q^2)$) are dimensionless and describe the strong interaction effects. The weak hadronic current, H_μ, should transform as a vector under Lorentz transformations and it has to be linear in ε^*. In the limit of the lepton mass being equal to zero, which is a good approximation only for muons and electrons. The last term of the above equation does not contribute due to a large tau mass compared to the other leptons mass. This last term $(\varepsilon^{*}\cdot k')(k'-k)_{\mu}\frac{A_3(q^2)}{m_B+m_{D^*}}$ only plays an important role if the lepton is a τ. Therefore, in this analysis, there are only three form factors: $V(q^2)$, $A_1(q^2)$, and $A_2(q^2)$.

There are some phenomenological form factor models which describe exclusive semileptonic B decay. The Isgur and Scora (ISGW2) model [23] is an update of the Isgur, Scora, Grinstein and Wise (ISGW) model, which also uses the constraints of HQET. In the ISGW2 model, the hadron form factor is evaluated using a non-relativistic calculation. It assumes the binding potential inside a meson is a Coulomb plus linear potential as:

$$V(r) = -\frac{4\alpha_s}{3r} + c + br \ , \qquad (2.17)$$

with α_s, b, and c are real numbers determined from the experimental data. The form factors

can be expressed as:

$$F(q^2) = \frac{F(q^2_{max})}{\left[1 + a(q^2_{max} - q^2)\right]^2} \ , \tag{2.18}$$

where a is a real number.

The Körner and Schuler (KS) [24] Model describes quark wave functions that are boosted from the B meson rest frame into the W^- rest frame. Using the free quark model at $q^2 = 0$ and vector-dominance, the so called *"nearest pole dominance"*, the normalization of the form factors can be expressed as:

$$F(q^2) = F(q^2 = 0)\left[\frac{m^2_{pole}}{m^2_{pole} - q^2}\right]^n \ , \tag{2.19}$$

where m_{pole} is the mass of the lowest-lying $q\bar{q}$ in the decay mode and n is an integer. In the exclusive decay $\bar{B}^0 \to D^{*+}\ell^-\bar{\nu}_\ell$, the quark transition is $b \to c$ then the pole mass is B^*_c meson. The form factor $A_1(q^2)$ is calculated when $n = 1$. $A_2(q^2)$ and $V(q)$ are calculated when $n = 2$. The power n is determined from QCD.

The Bauer, Stech and Wirbel (BSW) [26] Model calculates the form factors relativistically. This model assumes the form factors in the same way as the KS model by finding the value of the form factors at the maximum recoil ($q^2 = 0$) and $n = 1$. This model assumes the initial state and the final state meson wave functions overlap each other. The general form factors can be expressed as:

$$F(q^2) = F(q^2 = 0)\left[\frac{m^2_{pole}}{m^2_{pole} - q^2}\right] \ . \tag{2.20}$$

The value for the normalization $F(q^2 = 0)$ and the pole mass, m_{pole}, are slightly different.

Table 2.1: Predictions for form factor ratios and their q^2 dependence based on a common factor, $A_1(q^2)$. The pole forms are $P_1 = 1 - q^2/6.34^2$ and $P_2 = 1 - q^2/6.73^2$. $\mathcal{E}(q^2)$ stands for $exp[-0.03(q^2_{max} - q^2)]$.

MODEL	ISGW2 [23]	BSW [26]	KS [24]
$V(q^2)/A_1(q^2)$	1.27	$1.09P_2/P_1$	$1.00/P_1$
$A_2(q^2)/A_1(q^2)$	1.14	1.06	$1.00/P_1$
$A_1(q^2)$	$0.94\mathcal{E}(q^2)$	$0.65/P_2$	$0.70/P_1$
$\frac{\Gamma(B\to D^* l\bar{\nu}_\ell)}{\lvert V_{cb}\rvert^2}$	24.6 ps^{-1}	21.9 ps^{-1}	25.8 ps^{-1}

Table 2.2: Neubert's form factor ratios with $N(y) = 2.5/(y+1)$.

MODEL	Neubert [22]
$V(q^2)/A_1(q^2)$	$N(y)[1.35 - 0.22(y-1) + 0.09(y-1)^2]$
$A_2(q^2)/A_1(q^2)$	$N(y)[0.79 + 0.15(y-1) - 0.04(y-1)^2]$
$A_1(q^2)$	$0.86[2/(y-1)]^{0.6}$
$\frac{\Gamma(B\to D^* l\bar{\nu}_\ell)}{\lvert V_{cb}\rvert^2}$	29.0 ps^{-1}

The form factor ratios for each form factor model can be written in terms of the common form factor $A_1(q^2)$. Including the form factors obtained by Neubert [22] using the QCD sum rules, the explicit functional forms of the form factors in terms of the V_{cb} and the absolute decay rate for the $\bar{B} \to D^* \ell^- \bar{\nu}_\ell$ decays are summarized in Table 2.1 and Table 2.2.

The Lorentz-invariant form factors can be written in terms of the *helicity form factors* [24] for convenience. A basis for the polarization vectors is chosen in such a way so that the

helicity eigenstates are simple and are labeled by the helicity. Because the B meson is a spin-zero particle and the D^* meson and the W boson are spin-one particles, the D^* and the W are constrained to have the same helicity. The four non-zero helicity amplitudes are defined as:

$$H_+(q^2) = (m_B + m_{D^*})A_1(q^2) - \frac{2m_B P_{D^*}}{m_B + m_{D^*}} V(q^2) \ ,$$

$$H_-(q^2) = (m_B + m_{D^*})A_1(q^2) + \frac{2m_B P_{D^*}}{m_B + m_{D^*}} V(q^2) \ ,$$

$$\begin{aligned} H_0(q^2) &= \frac{1}{2m_{D^*}\sqrt{q^2}}[(m_B^2 - m_{D^*}^2 - q^2)(m_B + m_{D^*})A_1(q^2) \\ &- \frac{4m_B^2 P_{D^*}^2}{m_B + m_{D^*}} A_2(q^2)] \ , \end{aligned}$$

$$\begin{aligned} H_t(q^2) &= \frac{m_B P_{D^*}}{m_{D^*}\sqrt{q^2}}[(m_B + m_{D^*})A_1(q^2) + \frac{(m_B^2 - m_{D^*}^2)}{m_B + m_{D^*}} A_2(q^2) \\ &+ \frac{q^2}{m_B + m_{D^*}} A_3(q^2)] \ , \end{aligned} \tag{2.21}$$

where P_{D^*} is the momentum of the D^* meson in the B meson rest frame. The quantity P_{D^*} can be expressed as:

$$P_{D^*} = \sqrt{\frac{(m_B^2 + m_{D^*}^2 - q^2)^2}{4m_B^2} - m_{D^*}^2} \ . \tag{2.22}$$

Again, in the zero lepton mass limit, there are only three non-vanishing helicity form factors: $H_+(q^2)$, $H_-(q^2)$, and $H_0(q^2)$.

Integrating over all decay angles, Equation 2.10 can be re-written in terms of the helicity amplitudes as:

$$\frac{d\Gamma(\bar{B} \to D^* \ell^- \bar{\nu}_\ell)}{dq^2} = \frac{G_F^2 |V_{cb}|^2 P_{D^*} q^2}{96\pi^4 m_B^2} \left[|H_+(q^2)|^2 + |H_-(q^2)|^2 + |H_0(q^2)|^2 \right] \ . \tag{2.23}$$

Finally, by inserting the branching fraction of $D^* \to D\pi$, the full differential decay rate can be expressed as [25]:

$$\begin{aligned}
\frac{d\Gamma(\bar{B} \to D^* \ell^- \bar{\nu}_\ell)}{dq^2 d\cos\theta_\ell d\cos\theta^* d\chi} &= \frac{3G_F^2 |V_{cb}|^2 P_{D^*} q^2 \mathcal{B}(D^* \to D\pi)}{8(4\pi)^4 m_B^2} [(1-\cos\theta_\ell)^2 (\sin^2\theta^*) |H_+(q^2)|^2 \\
&+ (1+\cos\theta_\ell)^2 (\sin^2\theta^*) |H_-(q^2)|^2 \\
&+ 4\sin^2\theta_\ell \cos^2\theta^* |H_0(q^2)|^2 - 2(\sin^2\theta_\ell)(\sin^2\theta^* \cos 2\chi) H_+(q^2) H_-(q^2) \\
&- 4\sin\theta_\ell (1-\cos\theta_\ell)(\sin\theta^* \cos\theta^* \cos\chi) H_+(q^2) H_0(q^2) \\
&+ 4\sin\theta_\ell (1+\cos\theta_\ell)(\sin\theta^* \cos\theta^* \cos\chi) H_-(q^2) H_0(q^2)] \ . \qquad (2.24)
\end{aligned}$$

Chapter 3

Experimental Apparatus

3.1 Particle Accelerator: CESR

A particle accelerator is needed to create a high energy environment for B meson production. The Cornell Electron Storage Ring [58] (CESR), an electron-positron collider, was built in 1977-1979, and started operating in 1979. The entire complex is 40 feet underground, below an athletic field on the campus of Cornell University in Ithaca, New York. CESR accelerates electron and positron beams to a common energy of between 4.5 GeV to 6.0 GeV per beam in a ring of 768 meters in circumference. Its purpose is to collide electrons with positrons with center of mass energy in the range of 9 GeV to 12 GeV, the region of the Υ resonances. A schematic of CESR is shown in Figure 3.1. Acceleration begins in the linear accelerator, or *linac*. Electrons are emitted from a filament cathode at the end of

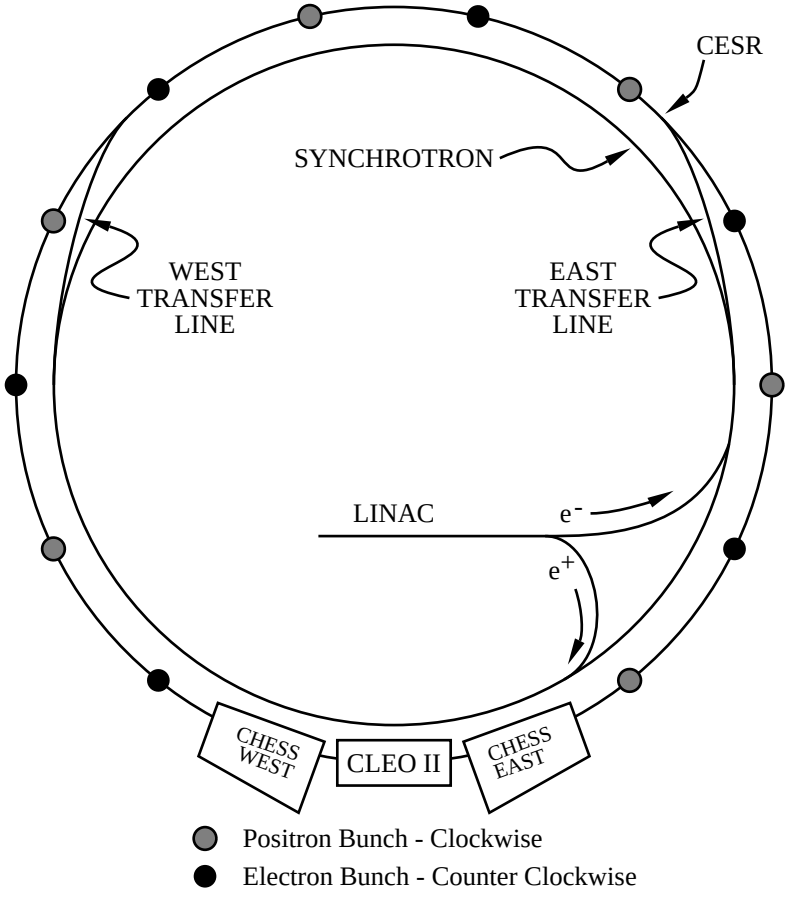

Figure 3.1: A schematic of CESR facility at the Wilson Synchrotron Laboratory on the campus of Cornell University in Ithaca, New York.

the linac and are accelerated by microwave electromagnetic fields. After transferring the 30 *meter* length of the linac, the electrons achieve energies of 200 MeV before being injected into the synchrotron. To create positrons, electrons are accelerated in the linac until they hit a tungsten target which is placed halfway through the linac. A shower of electrons, positrons, and X-rays are produced in the target. The positrons are collimated by magnetic fields, accelerated down the remaining length of the linac to 200 MeV and injected into the synchrotron in the direction opposite the electrons.

In the synchrotron, the electrons and positrons are accelerated by radio frequency electromagnetic waves until they reach their maximum energy of about 5 GeV after roughly 4,000 turns in the synchrotron which only takes a fraction of a second. Positrons are accelerated first then transfered into CESR through the west transfer line. The electrons are then passed to the storage ring through the east transfer line in the opposite direction within the same beam pipe. The entire injection procedure takes about 10 *minutes*. The particles are then stored into one of 9 different bunches evenly spaced about the storage ring. Each bunch is about 2 cm long, 0.3 mm wide, and 0.008 mm high, containing as many as 1.5×10^{11} particles. At the moment, CESR operates with nine trains of two bunches each. Typically, the particles are stored in the storage ring for approximately $75 - 90$ *minutes* per fill and are kept apart by a series of electrostatic separators such that there are no collisions except at the interaction point.

Once the particles are inside the storage ring, they travel in a circle and radiate x-rays in a direction tangent to the ring, losing energy gradually. The loss is of order 1.2 MeV per

turn around the ring. This energy needs to be replaced in order to keep the same radius of curvature. There are two radio frequency cavities in CESR which run at about 750 kW to provide the necessary energy to the beams to offset synchrotron radiation losses. A separate facility called the Cornell High Energy Synchrotron Source (CHESS) uses these intense x-rays, to study the structure of materials. These x-rays also strike the CESR beam pipe which is cooled by water.

The collision rate at which electrons and positrons collide in the interaction region is given by the product of the luminosity, $\mathcal{L}$, of the machine times the interaction cross section, σ, as:

$$R = \sigma \times \mathcal{L} \ , \tag{3.1}$$

where the luminosity of a collider is given as:

$$\mathcal{L} = fn\frac{N_{e^+}N_{e^-}}{A} \ , \tag{3.2}$$

where f is revolution frequency, n is the number of bunches in either beam around the ring, A is the cross-sectional area of each beam, N_{e^-} is the number of electrons in each bunch, and N_{e^+} is the number of positrons in each bunch. Obviously, the luminosity is large if the beams have a small cross-sectional area. The typical luminosity value at CESR is $4.0 \times 10^{32}\ cm^{-2}s^{-1}$. Recently, an instantaneous luminosity of greater than $0.8 \times 10^{33}\ cm^{-2}s^{-1}$ has been achieved.

3.2 CLEO II Detector

The CLEO II detector is a multipurpose solenoid-based detector designed to measure momentum and energy of various particle types with excellent resolution and efficiencies. The CLEO II detector was installed in 1988-1989 and data taking began in October 1989. The entire detector is about 5.8 m long, 6.5 m tall, and 6.5 m wide. Figure 3.2, Figure 3.3, and Figure 3.4 show a side view, end view, and one quadrant of the CLEO II detector, respectively. The CLEO II detector consists of a charged particle tracking system surrounded by a time-of-flight scintillation system, used primarily in the trigger and for particle identification, and a CsI crystal calorimeter. All of these subsystems are immersed in a 1.5 $Tesla$ magnetic field which is generated by a superconducting solenoid. The outermost detector is a muon identification system which uses the iron flux return of the magnet to distinguish muons from other particles. The following sections describe the relevant components for this analysis. Further detail may be found in [58].

3.2.1 Tracking System

After particles collide at the CESR interaction point, they encounter a beam pipe that is made of a beryllium tube of radius 3.5 cm, 33 cm long and 0.5 mm thick. The beam pipe is part of the accelerator vacuum system and has a thin wall for reducing scattering and energy loss by particles when passing through it. To limit the background from synchrotron radiation, the inner surface of the beam pipe is coated with a 1 μm layer of nickel and a

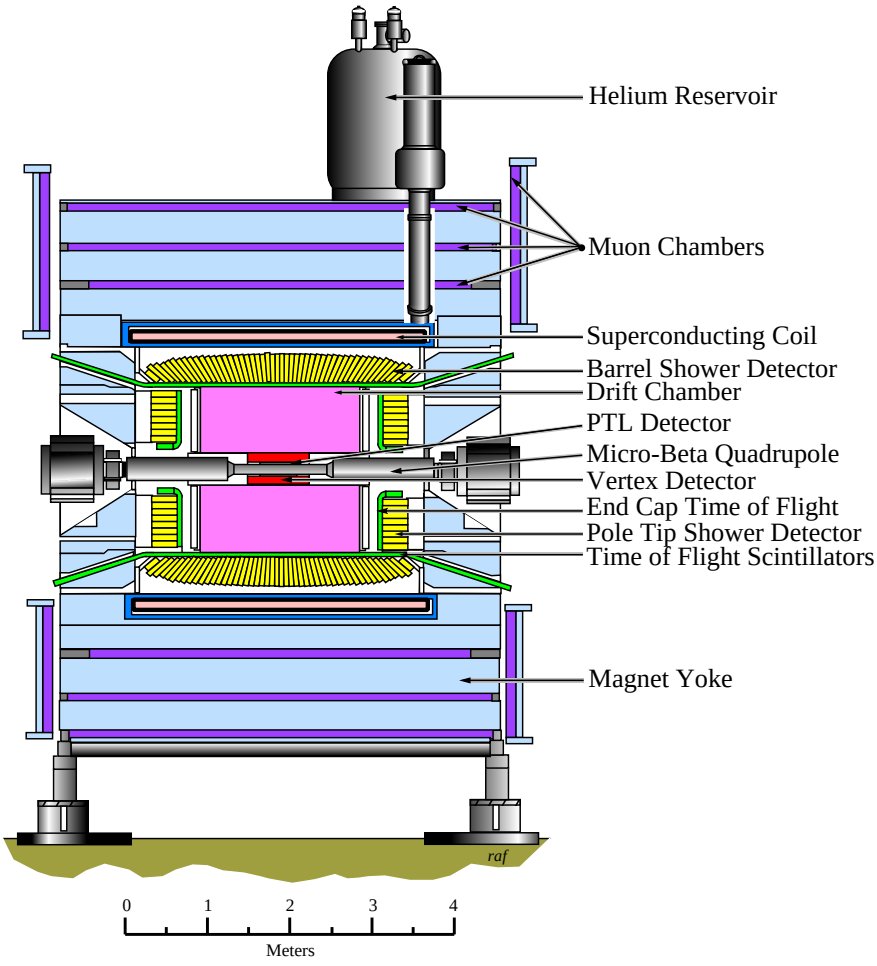

Figure 3.2: Side-view of the CLEO II detector.

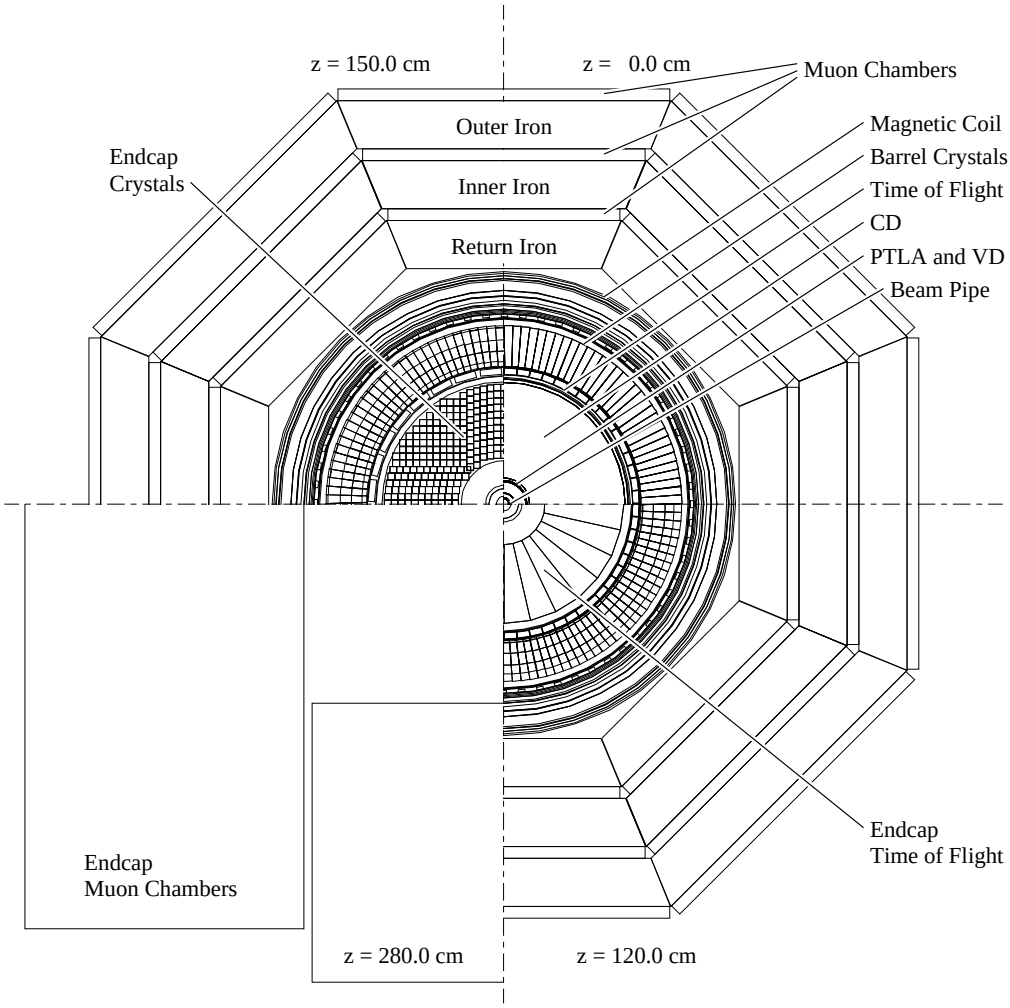

Figure 3.3: End-view of the CLEO II detector.

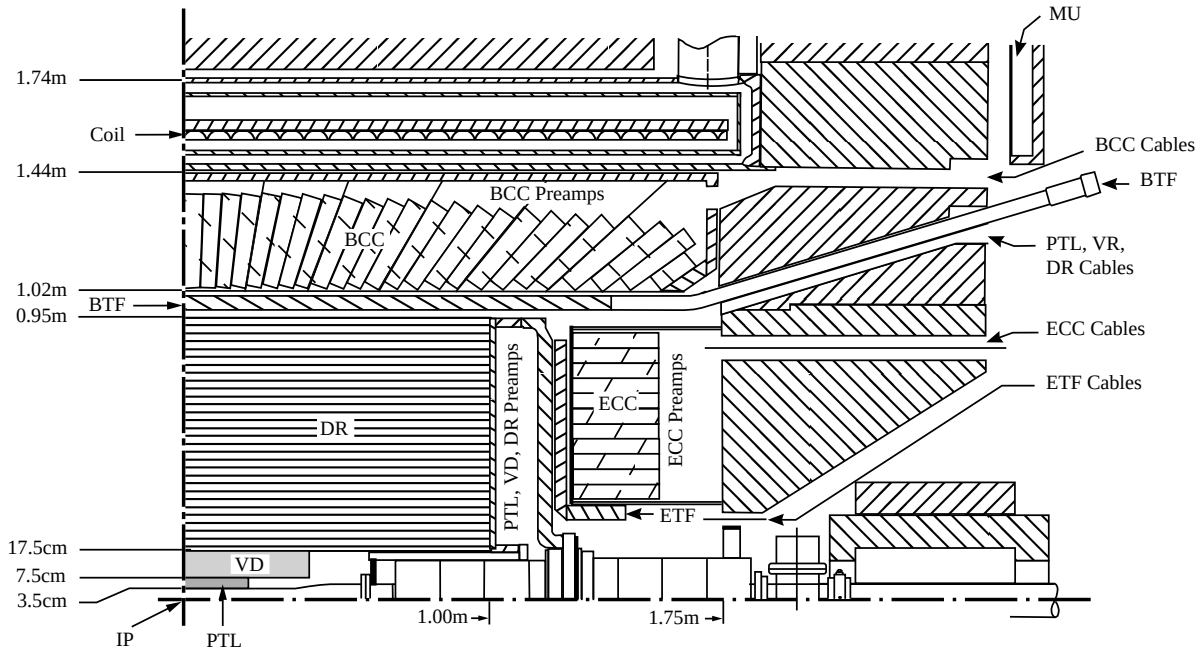

Figure 3.4: One quadrant of the CLEO II detector.

20 μm layer of silver.

The CLEO II central tracking system consists of a set of three cylindrical wire chambers with cathode strips to measure charged particle trajectories. The innermost tracking system is the Precision Tracking Layer (PT), follow by the Vertex Detector (VD) and the outer Drift Chambers (DR). A diagram of part of the CLEO II detector is shown in Figure 3.4.

Precision Tracking Layer

The purpose of the precision tracking layer (PT) is to measure the origin of the tracks precisely. It occupies the region between 3.5 cm and 7.5 cm from the beam pipe. It is a six-layer straw tube drift chamber, each with 64 tubes of increasing radius. In the middle of

each tube, there is a sense wire made of 15 μm gold plated tungsten serving as an anode. The tubes wall are conductive aluminized mylar, which serve as the cathode. At the beginning of CLEO II operation, the gas system used in the PT was a 50-50 argon and ethane mixture with a spatial resolution on the position measurement of about 100 μm. In 1992, the gas system in the PT was changed to dimethylethane (DME), which has a lower drift velocity and lower diffusion rate. The new improved resolution was about 50 μm in the $r - \phi$ plane. Figure 3.5 shows a cross section of the precision tracking layer.

Vertex Detector

The Vertex Detector (VD) occupies the region between 7.5 cm and 17.5 cm and has a length of 90 cm. The VD has 10 axial sense wire layers with radii from 8.4 cm to 16 cm and 70 cm in length. The axial sense layers are housed between two carbon filament tubes. In the first five layers, there are 64 sense wires per layer and the next five layers have 96 sense wires per layer for a total of 800 sense wires and 2,272 field wires. Figure 3.5 also shows the cross section of the vertex detector. The wires are composed of a nickel-chromium alloy with a slightly larger resistance than the tungsten that was used in PT. The gas system used in the VD was 50-50 mixture of argon and ethane with about 20 psi absolute pressure. Since there are no measurements of the z-coordinate of the track at the PT (longitudinal measurements only), the VD provides information about the z-coordinate of the track by comparing the relative amplitude of signals observed at the opposite ends of each sense wire. The resolution of measuring the z-coordinate of the track is 1.7 cm.

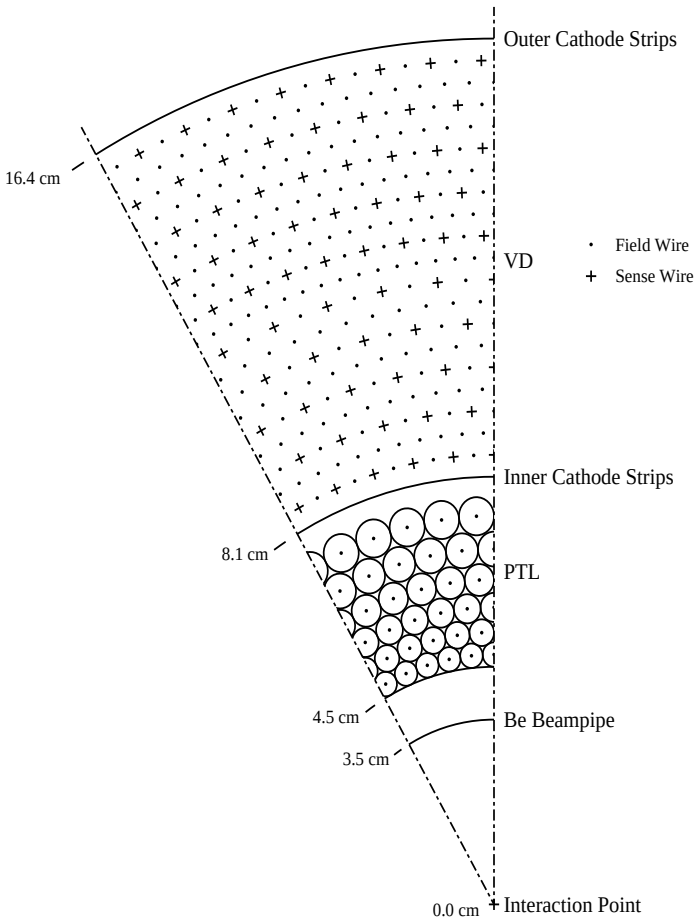

Figure 3.5: Cross section of the precision tracking layer and Vertex Detector.

Drift Chamber

The last tracking system in the CLEO II detector is the Drift Chamber (DR). It occupies the region between 17.5 cm and 95 cm and has a length of 193 cm. The DR has 51 layers of 20 μm gold plated tungsten sense wires, with a total of 12,240 anode sense wires and 36,270 field wires forming rectangular cells around them. These are 40 layers of axial sense wires aligned parallel to the z axis of the detector, and 11 layers of stereo wires. The cross section of the drift chamber is shown in Figure 3.6. The DR covers 94% of 4π at the inner surface and 71% of 4π at the outer surface. The transverse momentum resolution of the tracking system is measured to be:

$$(\delta p_t/p_t)^2 = \left(\frac{53 s p_t}{BL^2\sqrt{n}}\right)^2 + \left(\frac{0.054\sqrt{t}}{BL}\right)^2 , \tag{3.3}$$

where s is the accuracy of individual position measurement in meters, p_t is the transverse momentum perpendicular to the beam in GeV/c, B is the magnetic field strength in Tesla, n is the number of position measurements, L is the length (in meters) over which the measurements are made, and t is the thickness of obstructing material in the drift chambers in radiation length.

Using the formula given above with $L = 0.85\ m$, $B = 1.5\ tesla$, $n = 49$, $s = 150\ \mu m$, and $t = 0.025\ radiation\ length$, the expected transverse momentum can be written as:

$$(\delta p_t/p_t)^2 = (0.0011\ p_t)^2 + (0.0067)^2 . \tag{3.4}$$

At $p_t = 5.280\, GeV/c$, the expected the resolution is $\delta p_t = 47\ MeV/c$. The angular resolution is based on a sample of $e^+e^- \to \mu^+\mu^-$ events, which provides an estimate at high momentum.

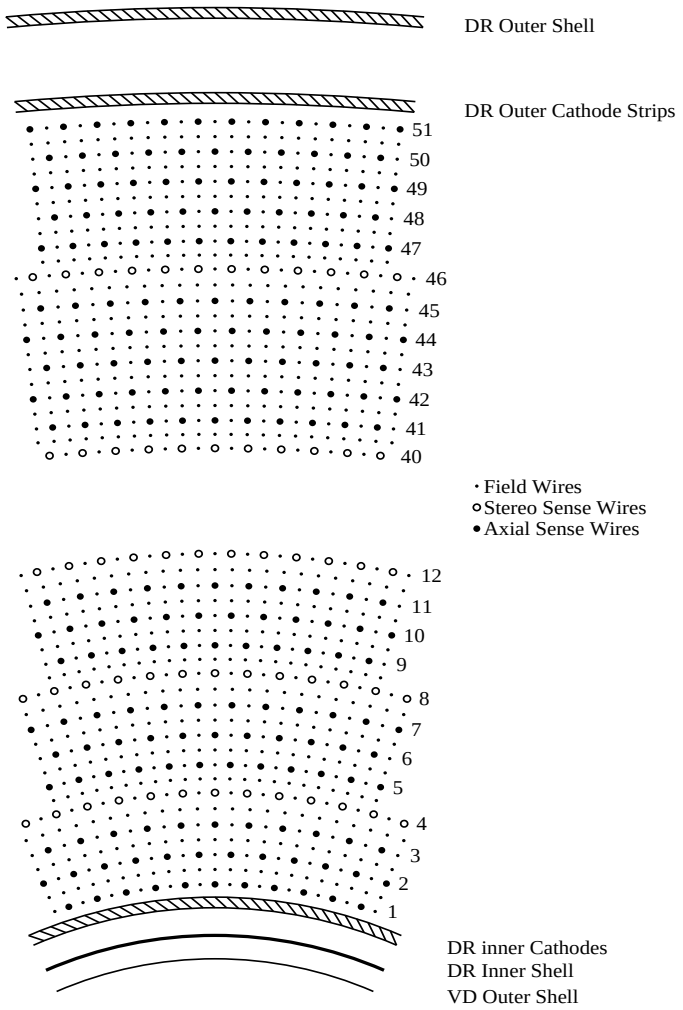

Figure 3.6: Cross section of the drift chamber.

At about 5.0 GeV/c, the angular resolutions are:

$$\sigma_\phi = 1\ mrad, \qquad \text{and} \qquad \sigma_\theta = 4\ mrad\ . \tag{3.5}$$

Charged Particle Identification by Specific Ionization

Particle identification in the main drift chamber is realized by picking up the ionization energy collected at the sense wire. Particles with velocity, $\beta \equiv \frac{v}{c}$, are characterized by their ionization energy loss per distance. The mean rate of energy loss is given by the Bethe-Bloch equation as:

$$-\frac{dE}{dx} = Kz^2\frac{Z}{A\beta^2}\left[\frac{1}{2}\ln\frac{2m_e\beta^2\gamma^2T_{max}}{I^2} - \beta^2 - \frac{\delta}{2}\right]\ , \tag{3.6}$$

where E is incident particle energy, A is atomic mass of medium, Z is atomic number of medium, I is mean excitation energy, m_e is electron mass, T_{max} is the maximum kinetic energy which can be imparted to a free electron in a single collision, δ is density effect correction to ionization energy loss, and dx is mass per unit area.

Particle species have been identified in CLEO II by examining the specific ionization energy loss, dE/dx, of the track within the 49 inner layers of the drift chambers. Figure 3.7 shows dE/dx (keV/cm) as a function of momentum for hadronic tracks in the drift chambers. Clear bands show each particle species. However, there is a large Landau tail of the ionization distribution, CLEO took the best estimator of dE/dx from the remaining 50% truncated mean. To obtain the best resolution, the raw data have to be corrected for the following effects: dip angle saturation, drift distance, entrance angle, and axial-stereo layer. More

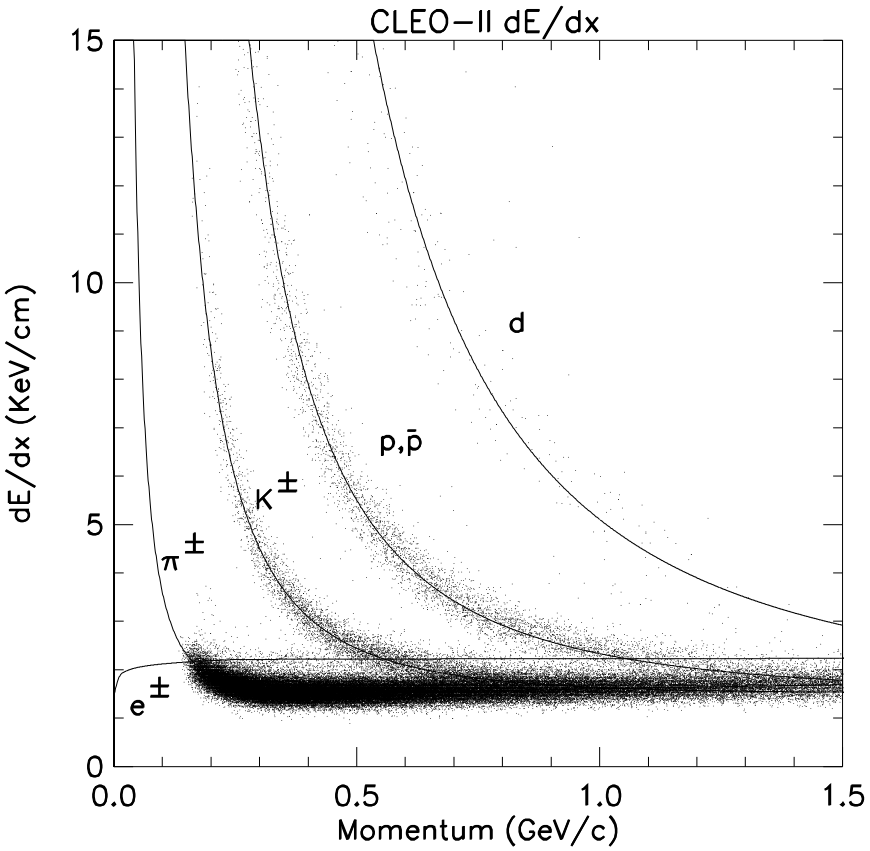

Figure 3.7: Specific ionization versus track momentum for electrons and hadrons.

detailed information for these corrections can be found in reference [58]. CLEO has measured the dE/dx resolution based on Bhabha tracks, $e^+e^- \to e^+e^-$, with 40 or more good hits per track. The resolution is found to be about 6.2% for Bhabha tracks and about 7.1% for minimum ionizing pions.

3.2.2 Time-of-Flight System

The time-of-flight (TOF) system at CLEO II detector is used not only as a tool for particle identification, but also as a primary trigger for data recording.

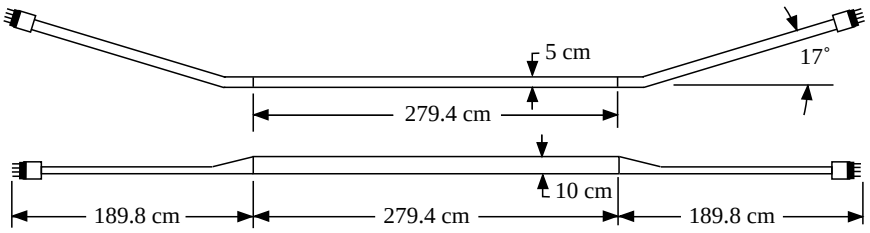

Figure 3.8: The geometry of a barrel time-of-flight counter.

The TOF system is comprised of both barrel counters and endcap counters. There are 64 barrel counters, each 279.4 cm long and 10 cm wide, mounted just outside the drift chamber with a light guide and photomultiplier at each end. Figure 3.8 shows the geometry of a barrel TOF counter. The light guides are needed for the photomultiplier tubes to operate properly in the magnetic field of 1.5 $Tesla$. There are 56 endcap counters, with 28 wedge-shaped counters mounted on each endcap calorimeter. Unlike the barrel, the endcap time-of-flight has one photomultiplier in each counter. The endcap time-of-flight counters are shown in Figure 3.9. The counters in the TOF system are made of bicron BC-408, a material with 2.1 ns decay time and 2.5 m attenuation length. The light pipes are made of UVT lucite with a 17° bend. The photomultiplier tubes are a slight modification of the Amperex 2020.

The purpose of the TOF system is to determine the species of a particle by measuring its velocity. The momentum is known from the curvature of the track within the tracking chambers and this independent measurement provides a constant on the mass of the particle. The TOF system measures the time that a particle takes to travel from the interaction point to the counter. The light that is produced in the counter is propagated through the light

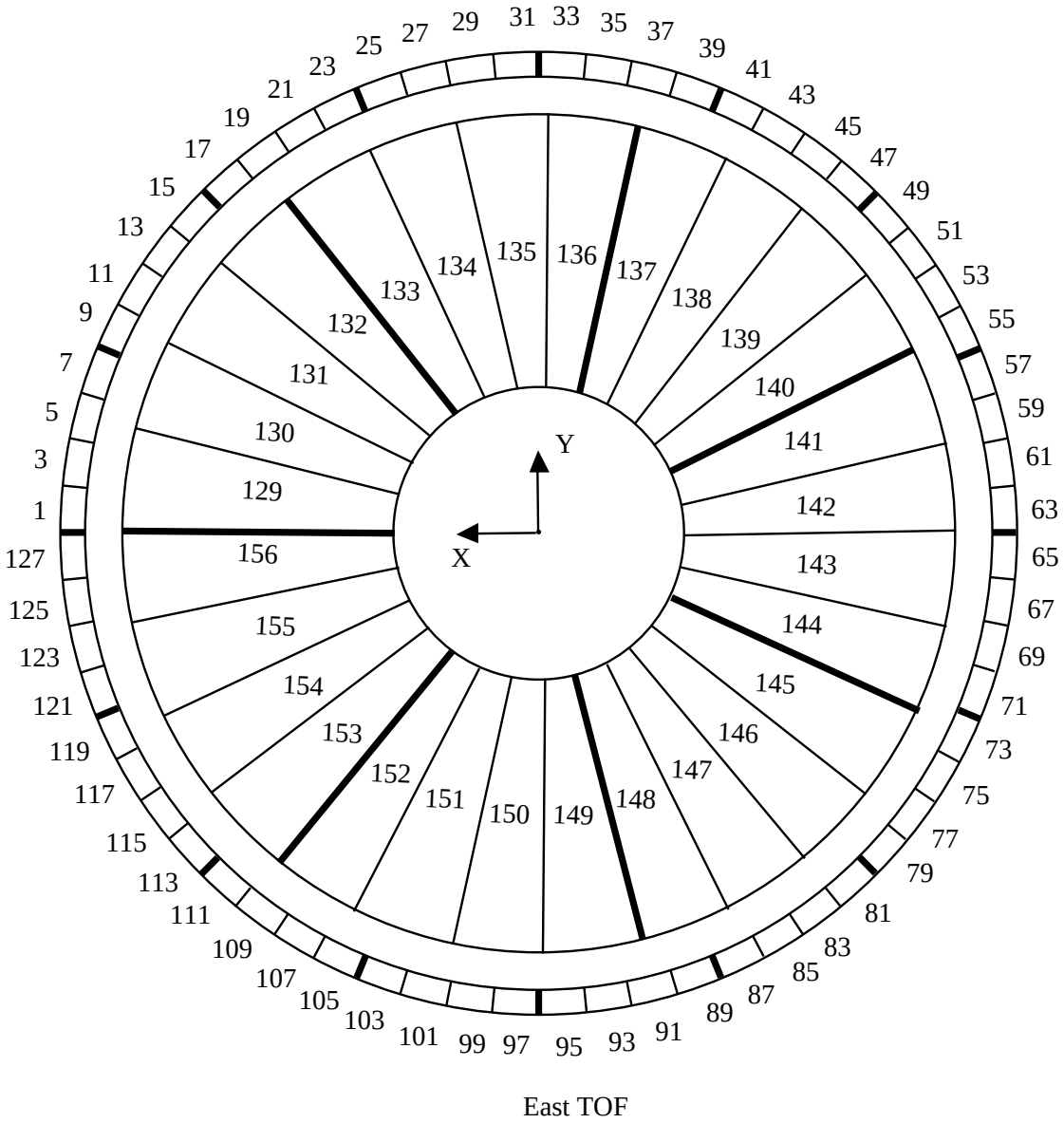

Figure 3.9: Endcap time-of-flight Counters.

guides and directed onto the face of a photomultiplier tube. This produces a current through the photoelectric effect from the cathode of the tube. The current is then amplified to give a fast electronic pulse, which can be used for triggering application.

Calibrating the TOF System

The purpose of TOF calibration is to calculate corrected values of flight time. This generates constants for use in physics analysis. CLEO II used Bhabha events to calibrate the TOF system and selected events for which there is only one hit in a counter. Kinematically, the speed of a given particle type with mass m_i (GeV/c^2) and momentum p (GeV/c) is given as a function of momentum, where $\beta \equiv \upsilon/c$:

$$\beta_i = \frac{p}{\sqrt{p^2 + m_i^2}} \ . \tag{3.7}$$

For a path length, L, and with the speed of light, c, the time-of-flight is given by:

$$T_i = \frac{L}{c\beta_i} \ . \tag{3.8}$$

The speed of the two particles with different mass but the same momentum p can be calculated as:

$$\frac{1}{\beta_2^2} - \frac{1}{\beta_1^2} = \left(\frac{m_2^2 - m_1^2}{p^2}\right) \ . \tag{3.9}$$

Using the above equations, the time difference for the two particles with the same path length, L, is given by:

$$(T_1 - T_2) = (L/c)\left(\frac{m_2^2 - m_1^2}{p^2}\right)\left(\frac{\beta_1\beta_2}{\beta_1 + \beta_2}\right) \ . \tag{3.10}$$

The calibration of the TOF system involves several possible time delays that need to be considered in order to correct the time of particles traveling from the interaction point to the counter. The time measured by one phototube is compared to the expected time, T_{ij}, which can be written as:

$$T_{ij} = T_{0j} + T_i + \frac{L_j}{v_i} + \frac{K_i}{Q_j^n} \ , \tag{3.11}$$

where T_{0j} is the calculated time for particles that travel from the interaction point to the counter, T_i is a time offset constant for each channel, L_j is the path length from where the particles hit the counter to the end of the counter, v_i is the velocity of signal propagation in the counter, n and K_i are the free parameters which depend on the pulse shape and the time slewing in the discriminator, and Q_j is the measured pulse height in ADC counts.

Appendix C describes a various TOF terminology and codes for calibrating TOF raw data at CLEO. The resolution of the barrel TOF system for electrons is 139 *ps* and the resolution for pions in hadronic events is 154 *ps*. There is some difficulty in calibrating the endcap TOF counters since there is only one phototube per counter. The preliminary result of the endcap TOF resolution is 272 *ps*. Figure 3.10 shows a plot of $1/\beta$ as a function of the particle momentum.

3.2.3 Electromagnetic Calorimeter

CLEO II has an Electromagnetic Calorimeter (CC) which is just outside of the TOF counters. It provides excellent photon detection down to low energies. The CC also consists of barrel

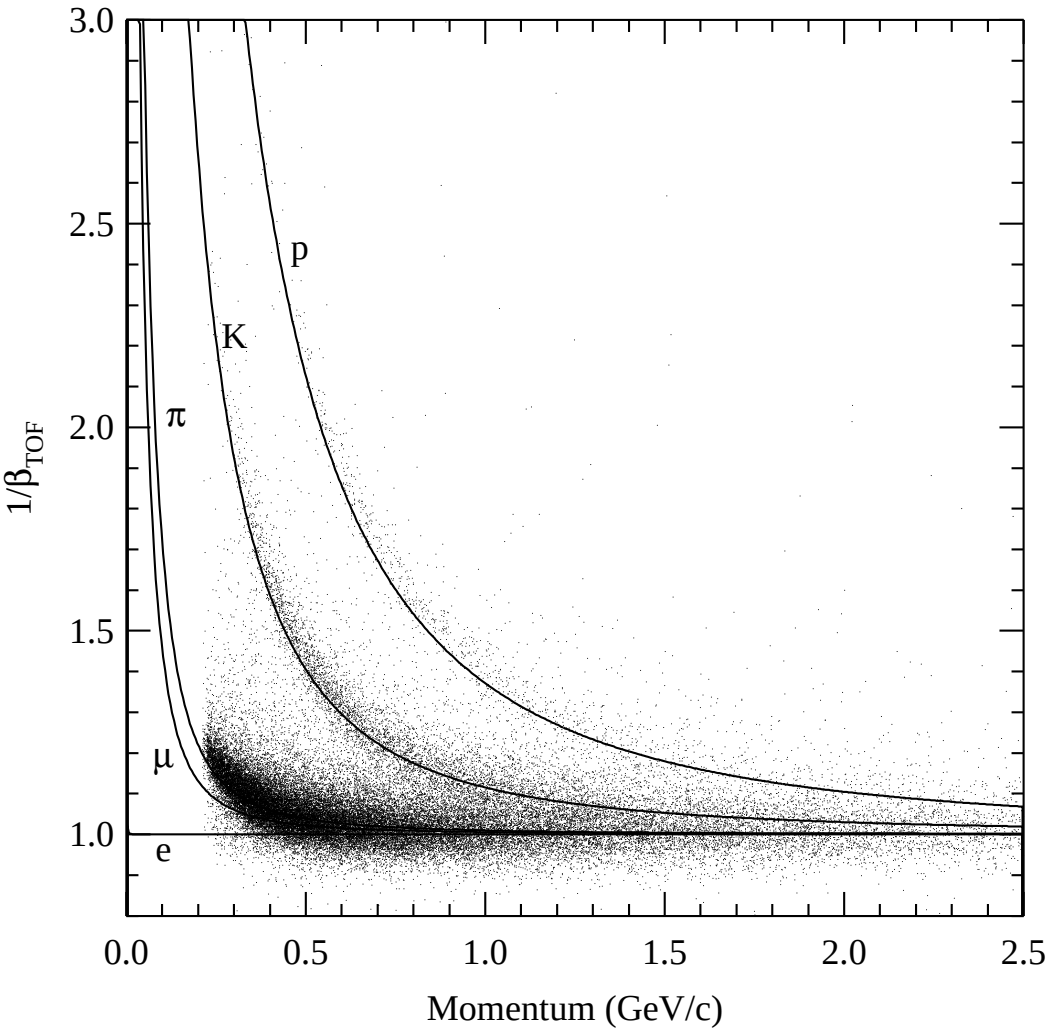

Figure 3.10: Plot of $1/\beta$ as a function of momentum measured in the drift chamber for a sample of hadrons and electrons in the barrel TOF.

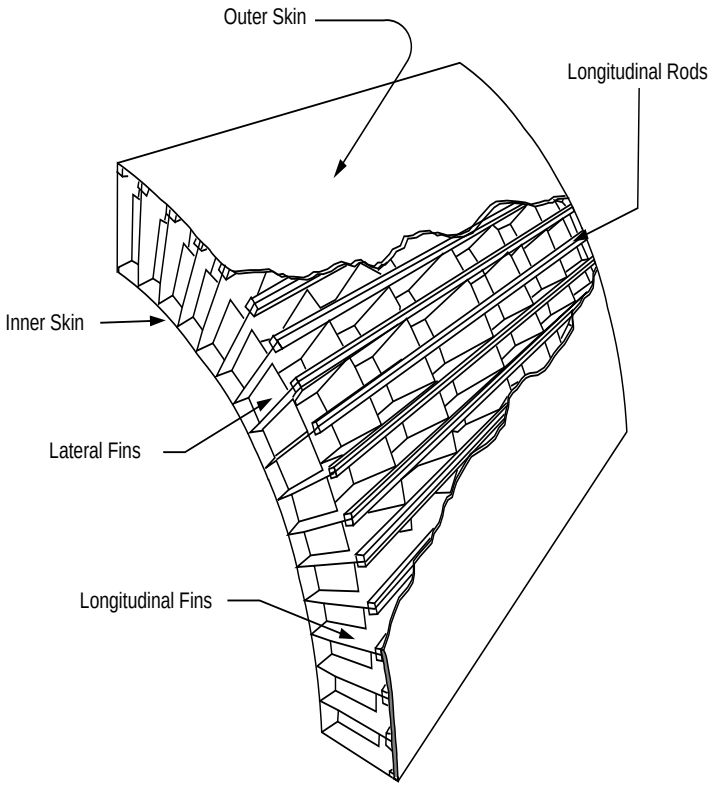

Figure 3.11: A portion of the barrel crystal holder.

and endcap sections that cover 95% of the solid angle. The barrel CC occupies the radial region between 1.02 *meter* and 1.44 *meter* and the endcap CC is located 1.25 *meter* from the interaction point. The CC is composed of 7,800 thallium-doped cesium iodide (CsI) crystals. The barrel CC contains 6,144 trapezoidal crystals that point towards the interaction point. The endcap CC contains 828 rectangular crystals all with axes parallel to the z-direction of the detector. Figure 3.11 and Figure 3.12 show a portion of the barrel and the endcap crystal holder, respectively. The CsI crystal is a scintillating material which can detect the neutral particles that pass through it and lose their energy by electromagnetic or hadronic

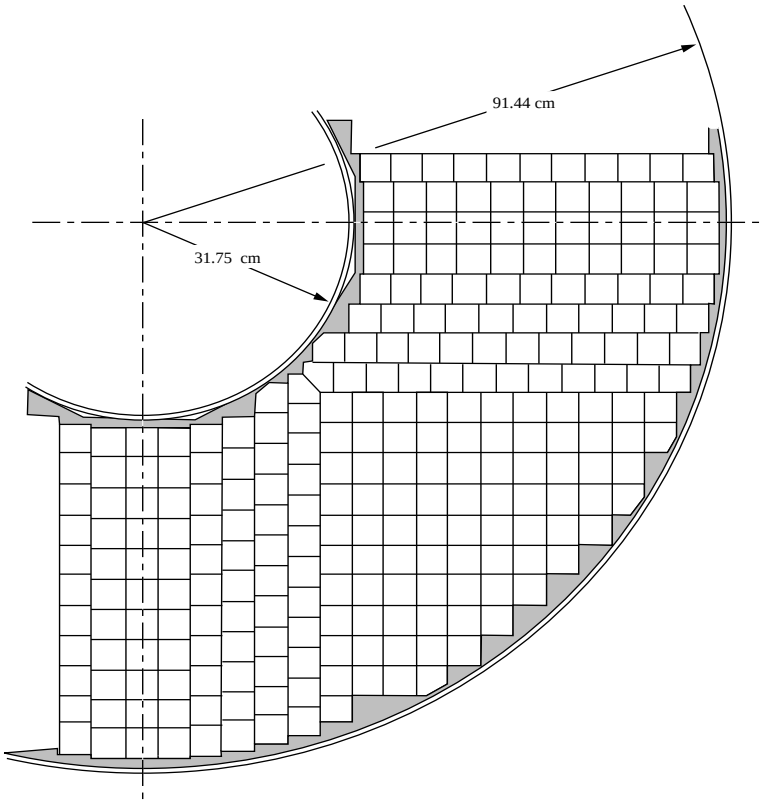

Figure 3.12: A layout of the crystals in the endcap.

showering. The crystal has a radiation length of about 1.83 cm and a very long decay time (900 ns), meaning very little energy is lost outside the crystal.

After calibration, the energy and angular resolutions of the CsI calorimeter for barrel and endcap region can be expressed as:

$$\frac{\sigma_E}{E}[\%] = \frac{0.35}{E^{0.75}} + 1.9 - 0.1E\,, \tag{3.12}$$

$$\sigma_\phi[\text{mrad}] = \frac{2.8}{\sqrt{E}} + 1.9 \quad \text{and} \quad \sigma_\theta[\text{mrad}] = 0.8\,\sigma_\phi \sin\theta\,, \tag{3.13}$$

for the barrel section, and

$$\frac{\sigma_E}{E}[\%] = \frac{0.26}{E} + 2.5\,, \tag{3.14}$$

$$\sigma_\phi[\text{mrad}] = \frac{3.7}{\sqrt{E}} + 7.3 \quad \text{and} \quad \sigma_\theta[\text{mrad}] = \frac{1.4}{\sqrt{E}} + 5.6\,, \tag{3.15}$$

for the endcap section, with E as the photon energy in GeV.

The great advantage of the CC is its very good resolution in reconstructing π^0 or η decays to $\gamma\gamma$. Photon energy resolution in barrel and endcap is 1.5% and 2.6% at 5 GeV, respectively. At low energy (100 MeV), the resolution in the barrel and endcap is 3.8% and 5.0%, respectively. The resolution in azimuth is 3 $mrad$ for barrel and 9 $mrad$ for endcap at 5 GeV; it is 11 $mrad$ for barrel and 19 $mrad$ for endcap at 100 MeV.

The ratio of E/p (where E is the energy measured in the calorimeter and p is the measured momentum), the shape of the shower, and dE/dx information from the tracking chambers can be used to identify electrons. These distributions are used to construct a log-likelihood defined by [27]:

$$\mathcal{L}_e = \sum_i ln(P_{ei}/P_{\neq ei})\,, \tag{3.16}$$

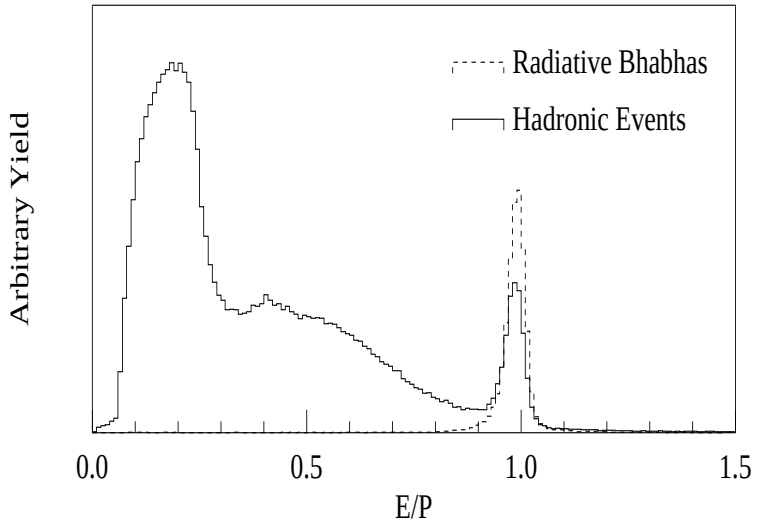

Figure 3.13: Distribution of E/p for electrons from radiative Bhabha events and charged tracks in hadronic events.

where P_{ei} is the probability that a track is an electron according to the i^{th} estimator and $P_{\neq ei}$ is the probability that the track is not an electron.

If an electron enteres the calorimeter, one expects that all of the electron's energy should be deposited in the calorimeter. Thus the ratio of E/p should be close to unity. Hadrons and muons have a smaller E/p. Figure 3.13 shows the typical ratios of E/p that result for electrons from radiative Bhabha events and charged tracks in hadronic events.

3.2.4 Superconducting Coil

The superconducting coil was designed to produce a 1.5 $Tesla$ uniform magnetic field directed along the beam line to within 0.2% over the volume of the drift chamber. This magnetic

field was used for bending the charged particle's paths in order to measure its momentum. The superconducting coil occupies the radial region between 1.44 m and 1.74 m; it is located just outside of the barrel calorimeter preamps. It consists of two layers of a 5 $mm \times 16$ mm aluminum rectangular tube containing a flat ribbon of Cu-Nb-Ti superconducting cable. It is operated with a current of $3,300$ $Amperes$ and is cooled by 700 $liters$ of liquid helium to a temperature of 4 $Kelvin$. The magnetic field in the solenoid must be returned through four layers of iron yoke outside the magnet, which are 36 cm thick each. The iron yoke is also used as an absorber for the muon chambers.

3.2.5 Muon Identification System

The outer CLEO II detectors are the Muon Chambers (MU) for muon identification, with the purpose of providing both maximum solid angle coverage and low probability of misidentification of a hadron as a muon. The MU only covers 85% of the total solid angle, with polar angle between 30° to 150°. There are three superlayers of detectors for muon identification. Each superlayer consists of three sublayers of plastic Iarocci tubes. The cross section of a muon chamber and one of the muon chamber superlayers can be seen in Figure 3.14 and Figure 3.15, respectively. The superlayers are about 5 m long and 8.3 cm wide. They are constructed from 8 rectangular plastic tubes which are 9 $mm \times 9$ mm. Three inner sides of the tube are coated with graphite to create the cathode. In the center of each tube, there is a silver-plated Cu-Be wire in each counter serving as an anode. The anodes operate at about $2,500$ V with a 50-50 Argon-Ethane mixture. The counter's spatial resolution is about

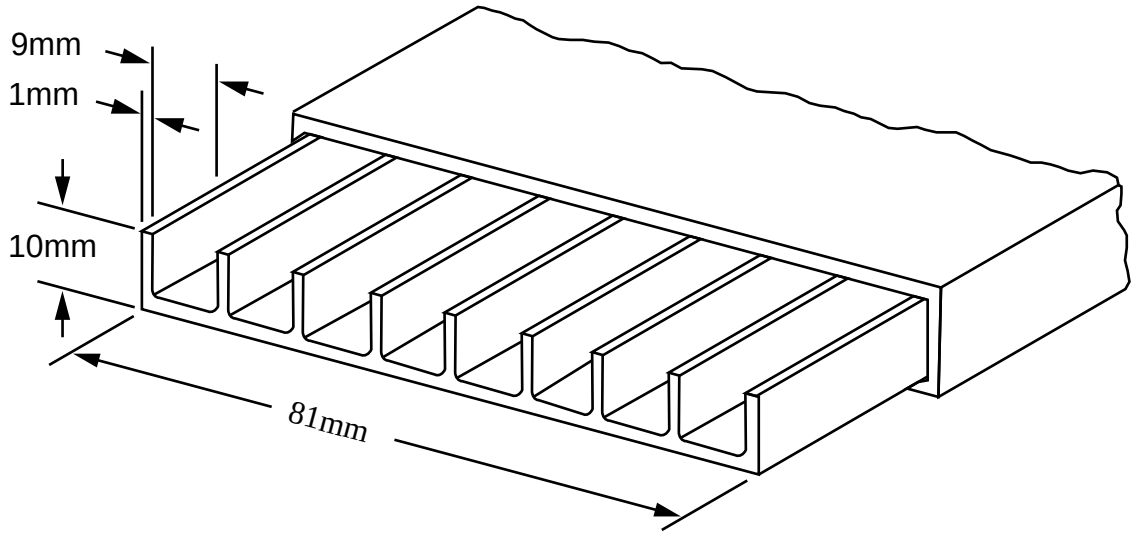

Figure 3.14: The cross section of a plastic proportional tube in the muon chambers.

2.4 *cm*.

Barrel muon chambers are embedded in an iron absorber at depths of 36 *cm*, 72 *cm*, and 108 *cm* of iron. The endcap muon chambers cover the two ends of the detector. The total equivalent thickness of iron absorber is between 7.2 and 10 nuclear absorption lengths. So the muon chambers are at depths of roughly 3, 5, and 7 absorption lengths (the nuclear absorption length in iron is 16.8 *cm*).

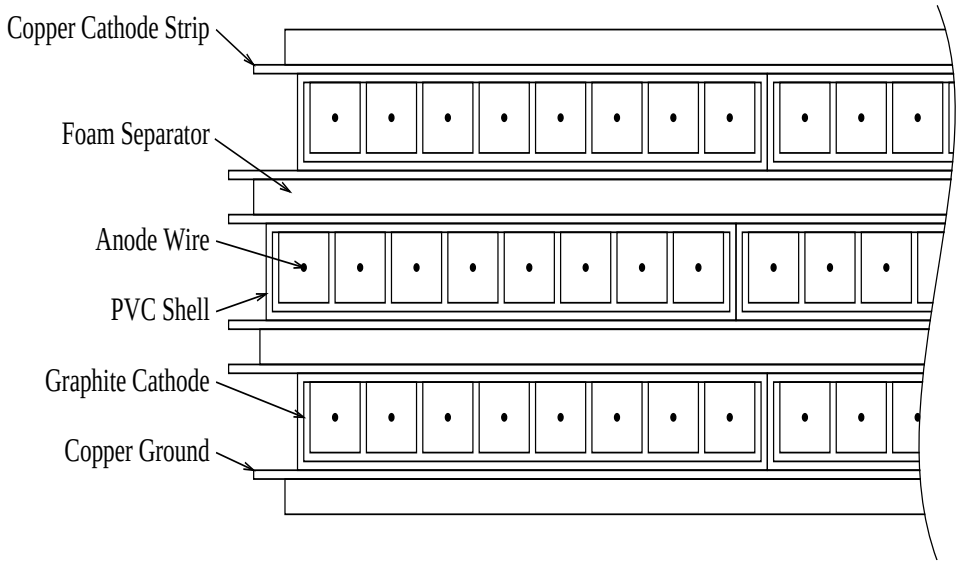

Figure 3.15: The Cross section of a muon chamber superlayer.

3.2.6 Trigger and Data Acquisition System

Two of the most important aspects of the Trigger and Data Acquisition System are the response time and the deadtime of the detector. The response time represents the time required to produce a signal after an event, and the deadtime is the minimum amount of time which must separate the recording of first event from the arrival of next recordable event. The sequencer at the CLEO II detector, which is used to reset the detector and trigger electronics and re-enable the experiment after an event is handled by an 8-bit programmable delay generator (AD9500).

The typical crossing rate of electrons and positrons in CESR is about 2.7 MHz and the actual rate of interesting annihilations is about 10 Hz. It is not possible for the CLEO II

detector to record all beam crossings. There is a hierarchical three-level trigger system at the CLEO II detector which is used for writing the interesting events onto the storage tape. The three-levels of the trigger system at the CLEO II detector are called: Level 0 (L0), Level 1 (L1), and Level 2 (L2). Once these three triggers hardware have decided that an interesting event has occurred, a final software filter called Level 3 (L3) is used for event quality, which records selected the events for subsequent analysis.

The fast L0 trigger makes an efficient decision whether charged or neutral particles have been produced in the detector. The L0 trigger receives inputs from the time-of-flight counters, the vertex detector, and from the electromagnetic calorimeter. The TOF detector is the fastest detector in CLEO, since signals from the phototubes are ready in about 55 ns. The rate of events passed by the L0 trigger is on the order of 20 kHz. After the L0 trigger requirements are met, all gates to the detector are disabled and all of the L1 trigger requirements are searched.

The L1 trigger receives inputs from the time-of-flight counters, the vertex detector, the drift chamber, and from the electromagnetic calorimeter. If there are no L1 criteria which have been met, then the system is reset and detector gating resumes. The overall L0 and L1 requirements reduce the rate of events to about 50 Hz.

The L2 trigger receives inputs from the vertex detector and the drift chamber to perform basic pattern recognition. The L2 criteria will only be examined if the L1 criteria are met. If the requirements of L2 are not met, then detector gating resumes. The L2 trigger decreases the overall event rate by a factor of two and stores information on disk for the L3 software

filter. Events that satisfy the L3 criteria are stored on magnetic tape for data reconstruction.

Before the physics analysis, the raw data that is stored on magnetic tapes must be processed for calibration from the various sub-detectors components. After calibration, the reconstruction program named PASS2 processes the data. This process converts the raw information such as drift-times and pulse heights into the reconstructed tracks and clusters of showers that are useful for physics analysis. This processed data is then stored on magnetic tape and is also made available on disk.

3.2.7 Monte Carlo Simulation

A Monte Carlo program is used to simulate the $\Upsilon(4S)$ decays and the CLEO II detector response. There are three steps for creating the Monte Carlo simulated data. The first step is performed by an event generator program called QQ [28]. This program simulates the decay of four-vectors and allows the user to choose the decay modes, according to the latest published values of particles properties and the branching fractions. All particles are simulated beginning with an $\Upsilon(4S)$ decay, except the long-lived particles such as $e^{\pm}$, $\mu^{\pm}$, γ, $\pi^{\pm}$, and $K^{\pm}$. In CLEO, we used two versions of an event generator program. In addition to the default QQ program, we used another generator program called EVT [29]. The EVT allows several corrections on semileptonic decays $B \to D^{**}\ell\nu$ according to ISGW2 model [23]. For example, the branching fraction of non-resonance decays $B \to D^{**}\ell\nu$ was changed from 1.3% to 1.2%.

The second step is performed by a package based on GEANT [30] from CERN called CLEOG. CLEOG is used to simulate the complete detector response to the events and to make the simulated data match with the true data. The long-lived particles which are not decayed within QQ are simulated here. This program simulates the passage of particles through the matter of the detector, the electromagnetic showering at the calorimeter, and the ionization of the drift chamber gas.

The last step in Monte Carlo simulation is to process the simulated data through PASS2, the standard event reconstruction in CLEO. In this process, the various detectors' noise and the beam background must be added to the physics hits generated by CLEOG. Hits from the random trigger events in data are also added.

We use the Monte Carlo simulation to determine the characteristics of signal-type events, to study the signal efficiency, to study the systematic error, and to estimate the various backgrounds in the analysis of real data.

Chapter 4

Measurement of $\frac{f_{+-}}{f_{00}}$ via Partial Reconstruction

4.1 Introduction

We report the first reconstruction of exclusive decays $B \to D^* \ell^- \bar{\nu}_\ell$ using a partial reconstruction method with neutral pions. By comparing with partially reconstructed decay using charged pions, we measure the ratio α, defined as:

$$\alpha \equiv \frac{f_{+-}}{f_{00}} \frac{\mathcal{B}(B^- \to D^{*0} \ell^- \bar{\nu}_\ell)}{\mathcal{B}(\bar{B}^0 \to D^{*+} \ell^- \bar{\nu}_\ell)} \ , \tag{4.1}$$

where f_{+-} and f_{00} are the respective production fractions of charged and neutral B mesons in $\Upsilon(4S)$ events. It is reasonable to assume that the semileptonic widths of the neutral and charged B meson are the same, in which case the ratio of semileptonic branching fractions is

equal to the lifetime ratio. Using measured lifetime ratios, we derive from our measurement the value of $\frac{f_{+-}}{f_{00}}$. Although this ratio is expected to be near unity, the deviation due to mass differences and Coulomb corrections could be as much at 20% [31].

4.2 *B* Meson Reconstruction

CLEO II has measured the exclusive decay $\bar{B}^0 \to D^{*+}\ell^-\bar{\nu}_\ell$ ($D^{*+} \to D^0\pi^+$) using reconstruction methods that involve both a full reconstruction of the D^* [32] and a partial reconstruction [33]. For the partial reconstruction[1] of $B \to D^*\ell^-\bar{\nu}_\ell$, the D^* is identified without reconstructing the D meson, and the presence of the neutrino is inferred by the conservation of momentum and energy. This is possible because the kinetic energies involved in the decays $D^* \to D\pi$ and in $\Upsilon(4S) \to B\bar{B}$ are very small compared to the masses. Compared to the full reconstruction method, partial reconstruction may result in a gain of as much as a factor of 20 in statistics. Partial reconstruction has been used at CLEO to tag neutral B mesons for measurements of the semileptonic branching fraction, b_0 [33], and the mixing parameter, χ_d [35].

In this thesis, we present the first measurement of the exclusive decay $B^- \to D^{*0}\ell^-\bar{\nu}_\ell$ ($D^{*0} \to D^0\ \pi^0$) and $\bar{B}^0 \to D^{*+}\ell^-\bar{\nu}_\ell$ ($D^{*+} \to D^+\ \pi^0$) using partial reconstruction. We use the partial reconstruction method not only for the charged B mesons, but also for the neutral

[1] This technique was pioneered by Professor Kay Kinoshita.

B mesons, through the decay chain:

$$\begin{aligned} \bar{B}^0 &\rightarrow D^{*+} \ \ell^- \ \bar{\nu}_\ell \\ &\hookrightarrow D^{*+} \rightarrow D^0 \ \pi^+. \end{aligned}$$

To partially reconstruct $\bar{B}^0 \rightarrow D^{*+}\ell^-\bar{\nu}_\ell$, lepton candidates are combined with charged pions from the decay $D^{*+} \rightarrow D^0\pi^+$. The corresponding charged B decay chain:

$$\begin{aligned} B^- &\rightarrow D^{*0} \ \ell^- \ \bar{\nu}_\ell \\ &\hookrightarrow D^{*0} \rightarrow D^+ \ \pi^- \end{aligned}$$

does not exist because of phase space limitations. In particular, there is not enough energy for the decay $D^{*0} \rightarrow D^+\pi^-$, as $M_{D^{*0}} < (M_{D^+} + M_{\pi^-})$. This limitation means only the $\bar{B}^0$ decay chain provides a source of leptons which correlate with slow charged pions. In this decay, the lepton must have a charge opposite to that of the slow charged pion. This combination will be referred to as $\ell - \pi^+$.

Leptons may also be combined with a slow neutral pion to reconstruct the decays $B \rightarrow D^*\ell^-\bar{\nu}_\ell$. In this case, both charged and neutral B will contribute to the signal. The charged B decay chain is:

$$\begin{aligned} B^- &\rightarrow D^{*0} \ \ell^- \ \bar{\nu}_\ell \\ &\hookrightarrow D^{*0} \rightarrow D^0 \ \pi^0 \end{aligned}$$

and the neutral B decay chain is:

$$\begin{aligned} \bar{B}^0 &\rightarrow D^{*+} \ \ell^- \ \bar{\nu}_\ell \\ &\hookrightarrow D^{*+} \rightarrow D^+ \ \pi^0. \end{aligned}$$

Table 4.1: The D^* decay modes and branching fractions.

D^* Decay	D^* Branching Fraction (%)
$D^{*+} \to D^0\pi^+$	68.3
$D^{*+} \to D^+\pi^0$	30.6
$D^{*+} \to D^+\gamma$	1.1
$D^{*0} \to D^0\pi^0$	61.9
$D^{*0} \to D^0\gamma$	38.1

These combinations will be referred to as $\ell - \pi^0$. Accounting for the respective $D^* \to D\pi$ branching fractions, the signal would consist of approximately $\frac{2}{3}$ $(B^- \to D^{*0}\ell^-\bar{\nu}_\ell)$ and $\frac{1}{3}$ $(\bar{B}^0 \to D^{*+}\ell^-\bar{\nu}_\ell)$. Table 4.1 shows the D^* decay modes and branching fractions.

4.3 Partial Reconstruction Kinematics

At the CLEO experiment, the momentum of B mesons produced in $\Upsilon(4S)$ decays is known and fairly small, $|\vec{P}_B| \simeq 340\ MeV/c$, and its direction is unknown. Using the constraint that the B meson, E_B, equals the precisely known beam energy, E_{beam}, we can write the mass of the neutrino in the decay $B \to D^*\ell^-\bar{\nu}_\ell$ as:

$$\begin{aligned}
\mathcal{M}_\nu^2 &= E_\nu^2 - P_\nu^2 \\
&= (E_{\rm beam} - E_\ell - E_{D^*})^2 - |\vec{P}_B - \vec{P}_\ell - \vec{P}_{D^*}|^2 \\
&= (E_{\rm beam} - E_\ell - E_{D^*})^2 - |\vec{P}_\ell + \vec{P}_{D^*}|^2 - P_B^2 + 2\vec{P}_B \cdot (\vec{P}_\ell + \vec{P}_{D^*}) \\
&= (E_{\rm beam} - E_\ell - E_{D^*})^2 - |\vec{P}_\ell + \vec{P}_{D^*}|^2 - P_B^2 + 2|\vec{P}_B||(\vec{P}_\ell + \vec{P}_{D^*})|\cos\theta_{(B,D^*l)} \quad (4.2)
\end{aligned}$$

where $\theta_{(B,D^*\ell)}$ is the angle between the B and the $D^*\ell$ momentum directions. The direction of the B is not known but we may use an approximation where $|\vec{P}_B| = 0$:

$$\widetilde{\mathcal{M}_\nu}^{\,2} \equiv (E_{\rm beam} - E_\ell - E_{D^*})^2 - |\vec{P}_\ell + \vec{P}_{D^*}|^{\,2} \ . \tag{4.3}$$

The last two terms in Equation 4.2 are always found to be small. $\widetilde{\mathcal{M}_\nu}^{\,2}$ peaks near zero if the decay has been properly reconstructed and the neutrino is the only missing particle. If additional daughter particles such as pions are produced, however, the value of $\widetilde{\mathcal{M}_\nu}^{\,2}$ will increase.

In the decay $B \to D^*\ell\nu$ with $D^* \to D\pi$, the D^* is just massive enough to create a D meson and a pion. These two daughters therefore have very little momentum in the D^* center-of-mass frame. In such threshold reactions, the pion produced from the D^* decay has a momentum below 225 MeV in the laboratory frame. This is often referred to as the "slow pion," and its direction coincides approximately with the direction of the parent D^*. This condition allows us to do an approximation of the D^* four-vector by measuring only the pion four-vector momentum, without the D meson reconstruction.

The $\Upsilon(4S)$ center-of-mass frame is the laboratory frame at CLEO. If the magnitude of the D^* velocity is given by β, then the D^* energy can be expressed as:

$$E_{D^*} = \gamma M_{D^*} \ , \tag{4.4}$$

and the energy of the slow pion in the laboratory frame is given by a Lorentz transformation as:

$$E_\pi = \gamma(E_\pi^{CM} + \beta P_\pi^{CM} \cos\theta) \ , \tag{4.5}$$

Table 4.2: Slow Pion Energy and Momentum in the D^* center-of-mass frame.

B Decay	D^* Decay	E_π^{CM} (MeV)	P_π^{CM} (MeV/c)
$\bar{B}^0 \to D^{*+}\ell^-\bar{\nu}_\ell$	$D^{*+} \to D^0\pi^+$	145.42	39.16
	$D^{*+} \to D^+\pi^0$	140.64	38.56
$B^- \to D^{*0}\ell^-\bar{\nu}_\ell$	$D^{*0} \to D^0\pi^0$	142.12	43.05

where E_π^{CM} and P_π^{CM} are the energy and the momentum of the slow pion in the D^* center-of-mass frame, respectively. The angle θ is the decay angle of the slow pion in the D^* center-of-mass frame with respect to the D^* direction in the laboratory frame. Table 4.2 shows the energy and momentum of the slow pion in the D^* center-of-mass frame for the various decay modes. Since the pions are distributed isotropically, in averaging over all the angles, the second term of Equation 4.5 drops out. As a consequence, the mean energy of the slow pion in the laboratory frame is

$$\gamma \simeq \tilde{\gamma} \equiv \frac{E_\pi}{E_\pi^{CM}} \ . \tag{4.6}$$

substituting this $\tilde{\gamma}$ into Equation 4.4, we get an approximation of the D^* energy in the laboratory frame:

$$E_{D^*} \simeq \tilde{E}_{D^*} \equiv \tilde{\gamma} M_{D^*} = \frac{E_\pi}{E_\pi^{CM}} M_{D^*} \ . \tag{4.7}$$

The approximate D^* momentum in terms of the slow pion is then

$$\vec{P}_{D^*} \simeq \tilde{\vec{P}}_{D^*} \equiv \frac{\vec{P}_\pi}{|\vec{P}_\pi|}\sqrt{\tilde{E}_{D^*}^2 - M_{D^*}^2} \ . \tag{4.8}$$

Finally, with all of these above approximations, the observable *missing mass squared* can be

expressed as:

$$\widetilde{\mathcal{M}_\nu}^{\,2} \equiv (E_{\rm beam} - E_\ell - \tilde{E}_{D^*})^2 - |\vec{P}_\ell + \tilde{\vec{P}}_{D^*}|^2 \ . \tag{4.9}$$

4.4 Data Sample and Selection Criteria

4.4.1 Data Sample

We use data taken with the CLEO II detector during the period 1990-5 (4S2 – 4SG); see Appendix B. We exclude the data sets 4S9 and 4SA due to problems with the calorimeter calibration which affect our π^0 sample. We analyze 2.729 fb^{-1} of data taken at the $\Upsilon(4S)$ resonance peak, and 1.430 fb^{-1} taken at a center-of-mass energy which is lower by 60 MeV (off-resonance). The on-resonance sample includes 2.890 million $B\bar{B}$ events. All events are required to pass the standard hadronic criteria ($KLASGL = 10$) [39]. This selection helps to remove Bhabha and muon pair events. In addition, we require an event to contain at least 5 charged tracks ($NTRKCD \geq 5$). To suppress continuum background, we require the ratio R_2 of Fox-Wolfram moments [40] to be less than 0.4 ($R2GL < 0.4$).

The contribution from continuum events is estimated by analyzing the off-resonance data and scaling to correct for differences in the integrated luminosity and center of mass energy. The continuum scaling factor, $\lambda_{continuum}$, is

$$\lambda_{continuum} = \frac{\mathcal{L}_{on}}{\mathcal{L}_{off}} \frac{E_{off}^2}{E_{on}^2} = 1.888 \ .$$

4.4.2 Selection Criteria

Appendix B describes all CLEO terminology for analysis variables used in the discussion below.

For our analysis, all lepton candidates are required to have momentum between 1.8 GeV/c and 2.5 GeV/c. Electrons are identified by using the Cornell ID package, with $R2ELEC \geq$ 3.0 and must fall in the fiducial region $|CZCD| < 0.707$. Muons must have $MUQUAL = 0$ and $DPTHMU \geq 5$ and also fall in the fiducial region $|CZCD| < 0.707$. All leptons are required to satisfy the following tracking criteria:

- $TNG \geq 0$ (good track that should be kept)
- $KINCD = 0$ *or* -2 (track classification for good primary track)
- $NHITPT > 0$ (number of hits in PT for track)
- $NHITVD > 0$ (number of hits in VD for track)
- $RHITDR > 0.4$ (percentage of DR hits over expected for a track)
- At least two of the following:

  $|DBCD| < 5\ mm$; (track impact parameter in radial distance to the beam line)

  $|ZOCD| < 5\ cm$; (track impact parameter in r-z direction)

  $RESICD < 1\ mm$ (RMS residual in tracking fitting)

Since we are only looking for "slow pions" in the partial reconstruction method, all pions

candidates are required to have momenta between 50 MeV/c and 220 MeV/c. The charged pions must satisfy the following criteria:

- $TNG \geq 0$
- $KINCD = 0$ *or* -2
- $|SGPIDI| < 3.0$ (number of sigma away from pion)
- $|DBCD| < 5\ mm$
- $|ZOCD| < 5\ cm$

Reconstructed π^0 mesons are obtained from pairs of showers in the electromagnetic calorimeter which do not match the projection of any drift chamber track. Each shower must have energy greater than 50 MeV, be in the good barrel region only ($\cos\theta_\gamma < 0.71$), and pass the shower shape cut called $E9/E25$ cut number 1 (99% efficient for isolated showers). The quantity $E9/E25$ is measured as:

$$E9/E25 \equiv \frac{Energy\ of\ 9\ central\ crystals}{Energy\ of\ 25\ central\ crystals}\ . \tag{4.10}$$

The 9 central crystals are those in a 3×3 array, with the most energetic crystal at the center whereas the 25 central crystals are those in the 5×5 array that is concentric with the 3×3 array. The most widely used cut on $E9/E25$ in CLEO (cut number 1) will keep 99% photons and get rid of most of hadronic showers. The $E9/E25$ cut also gets rid of two photons which are close together; however, we did not worry much about the photons which are being close together because we use a very low photon energy spectrum.

To find the π^0 mesons, we took pairs of photons and calculated the di-photon invariant mass. Each photon must be in the good barrel region ($\cos\theta_\gamma < 0.71$) of the crystal calorimeters.

The π^0 mass width depends on both the energy and angular resolution of its component photons and averages 5 MeV/c^2.

4.5 $\ell - \pi^+$ Analysis

Candidates for the decay $\bar{B}^0 \to D^{*+}\ell^-\bar{\nu}_\ell$ are formed by pairing identified leptons with slow charged pions of opposite charge (*"right sign combination"*) and calculating $\widetilde{\mathcal{M}}_\nu^2$, as described above. The contribution from continuum events ($e^+e^- \to \gamma^* \to q\bar{q}$ where $q = u, d, s, c$) is evaluated by analyzing the off-resonance data, and correcting the yields in the integrated luminosity and center of mass energy. The contribution from candidates containing a fake lepton is estimated by repeating this analysis using candidates in which the harder track satisfies all criteria except lepton identification. Further details may be found in [42]. After these have been subtracted, the remaining candidates consist of a real lepton from B decay in combination with a soft track. We define uncorrelated background as a random combination of real leptons from B decay that are paired with right sign soft pions that come from the other B. The distribution in $\widetilde{\mathcal{M}}_\nu^2$ is shown in Figure 4.1. The plot shows right sign data, with continuum and fake lepton contributions subtracted (solid histogram) and uncorrelated background estimated by Monte Carlo (dashed). Correctly identified signal candidates accumulate in the region $\widetilde{\mathcal{M}}_\nu^2 > -2.0$ (GeV^2), as shown in Figure 4.2. We shall

define this region to be the *"peak"* (PK) region.

We identify two general types of backgrounds to this signal from $B\bar{B}$ decay. Candidates formed from the lepton and soft π from the D^* in decays of the type $\bar{B} \to D^*\pi\ell^-\bar{\nu}_\ell$ ($D^* \to D^0\pi$), where the $D^*\pi$ may or may not form a D^{**} state, will also accumulate near $\widetilde{\mathcal{M}}_\nu^2 = 0$, although the distribution is shifted slightly to positive values due to the additional pion in the decay. We define such events as *"correlated background."* All other combinations, where the pion does not originate with a D^* from the same B meson as the lepton, are defined as *"uncorrelated background."* The uncorrelated background is estimated by analyzing 17.5 million generic Monte Carlo $B\bar{B}$ events, excluding signal and correlated background. The resulting distribution in $\widetilde{\mathcal{M}}_\nu^2$ is normalized to the data in the sideband (SB) region $-25 < \widetilde{\mathcal{M}}_\nu^2 < -4\ GeV^2$, where no signal candidates are expected. This estimated background is shown with the data in Figure 4.1 and Figure 4.3. After continuum, fake lepton, and uncorrelated $B\bar{B}$ background subtractions, $12,495 \pm 164$ candidates remain in the PK region. This includes correlated background as well as signal candidates. The yield in bins of pion momentum is shown in Figure 4.4.

4.6 $\ell - \pi^0$ Analysis

Candidates for the decay $\bar{B} \to D^* l^- \bar{\nu}$ ($D^* \to D\pi^0$) are formed by pairing identified leptons with π^0 candidates and performing an analysis similar to that with $D^* \to D\pi^+$. In assembling candidates, we save $\pi^0 \to \gamma\gamma$ candidates from a wide range of $\gamma\gamma$ invariant mass,

$0.085 < M_{\gamma\gamma} < 0.185\ GeV/c^2$, and calculate $\widetilde{\mathcal{M}}_\nu^2$ using the measured $\gamma\gamma$ momentum and the known π^0 mass, which is 134.9764 MeV/c^2 [5]. As with the $\ell - \pi^+$ analysis, continuum and fake lepton candidates are first estimated and subtracted from all distributions.

In the $\ell - \pi^0$ analysis, there is an additional background due to *"fake π^0"* candidates, formed from random γ pair combinations. To estimate the fake π^0 background, we construct candidates consisting of an identified lepton and a π^0 candidate and plot the $\gamma\gamma$ invariant mass of the π^0 candidate, in bins of 10 MeV/c width in the π^0 momentum, separately for candidates falling in the $\widetilde{\mathcal{M}}_\nu^2$ SB and SG regions. Each plot is fitted to a sum of π^0 signal and background shapes generated via Monte Carlo simulation. In the fit we exclude the region $0.14 < M_{\gamma\gamma} < 0.15\ GeV$ because the π^0 signal in this region does not show good agreement between Monte Carlo and data. This can be seen in Figure 4.5, where we have fitted the plots after summing over all π^0 momentum bins. We find that the fake π^0 background is well simulated by Monte Carlo in that the fits are all good and the scaling factors resulting from the fits are consistent with being a single constant over all π^0 momenta for both SB and PK candidates. Figures 4.6 and 4.7 show a sample of fits to the $\gamma\gamma$ invariant mass, and Table 4.3 gives the fitted fake π^0 scaling factors and confidence level for each. Figure 4.8 shows a fit of the scaling factors to a constant. It gives a confidence level of 70% and a scaling factor of 0.1680 ± 0.0008, very close to the ratio of the numbers of $B\bar{B}$ events in data and Monte Carlo (0.1667 ± 0.0001). This allow us to use the fitted value to calculate the amount of the fake π^0 in each distribution considered. Appendix A describes an alternative way to identify fake π^0 mesons which we explored.

Table 4.3: Data/Monte Carlo scaling factor to obtain fake π^0 rates, in bins of π^0 momentum for SB and PK candidates.

π^0 Momentum (GeV/c)	SB Fake π^0 SF	C.L (%)	SG Fake π^0 SF	C.L (%)
$0.05 - 0.06$	0.161 ± 0.014	99	0.170 ± 0.007	25
$0.06 - 0.07$	0.171 ± 0.008	40	0.161 ± 0.006	60
$0.07 - 0.08$	0.179 ± 0.006	25	0.170 ± 0.006	11
$0.08 - 0.09$	0.178 ± 0.005	61	0.170 ± 0.005	61
$0.09 - 0.10$	0.166 ± 0.005	89	0.170 ± 0.005	56
$0.10 - 0.11$	0.173 ± 0.004	87	0.165 ± 0.005	25
$0.11 - 0.12$	0.168 ± 0.004	54	0.172 ± 0.005	71
$0.12 - 0.13$	0.168 ± 0.004	62	0.167 ± 0.005	15
$0.13 - 0.14$	0.164 ± 0.004	71	0.166 ± 0.006	27
$0.14 - 0.15$	0.166 ± 0.004	52	0.172 ± 0.006	9
$0.15 - 0.16$	0.164 ± 0.004	36	0.170 ± 0.006	99
$0.16 - 0.17$	0.175 ± 0.004	83	0.165 ± 0.006	65
$0.17 - 0.18$	0.167 ± 0.004	38	0.166 ± 0.006	95
$0.18 - 0.19$	0.166 ± 0.004	4	0.165 ± 0.007	37
$0.19 - 0.20$	0.161 ± 0.003	35	0.170 ± 0.008	82
$0.20 - 0.21$	0.172 ± 0.003	30	0.157 ± 0.008	49
$0.21 - 0.22$	0.170 ± 0.003	9	0.177 ± 0.009	97

Having determined the quantity of fake π^0 mesons, we are able to determine the number of candidates which are a real lepton in combination with a real π^0 in a $B\bar{B}$ event. We would now like to determine the uncorrelated background portion of these. To do this we fit the $\gamma\gamma$ mass distributions from SB candidates to a sum of fake and real π^0 distributions, with the fake normalization fixed to the value determined above. Since the SB contains no signal or correlated background candidates, we use it to set the scaling factor for uncorrelated background candidates, and use the same scaling factor in the PK region. Figure 4.9 shows two plots with typical fit results. In Figure 4.10 the scaling factors resulting from these fits are plotted as a function of π^0 momentum and fitted to a constant. The fit has a confidence level of 25% and we obtain a scaling factor of 0.155 ± 0.004.

The remaining PK candidates are then our signal plus correlated background. The numbers are determined by taking the $M_{\gamma\gamma}$ distributions of PK candidates in pion momentum bins and fitting to fake π^0, real π^0 from uncorrelated background, both with fixed normalizations, and real π^0 with floating normalization. One fit is shown in Figure 4.11. The result of this fit is our raw count of candidates. After continuum, fake lepton, fake π^0, and uncorrelated $B\bar{B}$ background subtractions, $3,916 \pm 167$ candidates remain in the PK region. This count is plotted as a function of the π^0 momentum in Figure 4.12.

4.7 Correlated Background

Contributions from decays of the type $\bar{B} \to D^* \pi \ell^- \bar{\nu}_\ell$ can occur through the channels:

$$\begin{aligned} B^- &\to D^{*+} \pi^- \ell^- \bar{\nu}_\ell \\ \bar{B}^0 &\to D^{*0} \pi^+ \ell^- \bar{\nu}_\ell \\ B^- &\to D^{*0} \pi^0 \ell^- \bar{\nu}_\ell \\ \bar{B}^0 &\to D^{*+} \pi^0 \ell^- \bar{\nu}_\ell \ , \end{aligned}$$

where $D^*\pi$ may or may not be from an excited charm resonance ("D^{**}"). All four contribute to $\ell - \pi^0$, but only the modes with D^{*+} contribute to $\ell - \pi^+$. The distribution in $\widetilde{\mathcal{M}}_\nu^2$ of candidates originating with these modes is sufficiently similar to that of the signal that we cannot separate them easily. We use Monte Carlo simulation to estimate their contribution. We preserve the relative rates to the different D^{**} modes as generated by the CLEO Monte Carlo while requiring the total to be equal to the branching fraction measured at LEP [43], $\mathcal{B}(B \to D^* \pi^+ \ell^+ \nu X) = (2.26 \pm 0.29 \pm 0.33)\%$. We assume this rate branches equally to D^{*-} and D^{*0}, and that $B \to D^* \pi^0 \ell^+ \nu X$ contributes additionally at half the rate, so $\mathcal{B}(B \to D^{*-/0} \pi \ell^+ \nu X) = (1.70 \pm 0.33)\%$, where the statistical and systematic error have been added in quadrature. The branching fractions used are shown in Table 4.4.

Figures 4.12 show the raw signal yields with the estimated contribution from D^{**}, overlaid as a dashed histogram. The D^{**} contributions are small due to the relatively high lepton momentum requirement that we make in this analysis. This background comprises $(3.4 \pm 0.3)\%$ and $(2.3 \pm 0.2)\%$ of the raw signal for $\ell - \pi^+$ and $\ell - \pi^0$ analyses, respectively. We

Table 4.4: Branching fractions and efficiencies of $B \to D^{**}\ell\nu$ used to estimate correlated backgrounds. ϵ_0 is the reconstruction efficiency for modes involving $D^* \to D\pi^0$ and ϵ_+ is for modes with $D^{*+} \to D^0\pi^+$.

D^{**} state	$\mathcal{B}(B \to D^{**}\ell\nu)$	$\mathcal{B}(D^{**} \to D^*X)$	Product BR	$\epsilon_0(\%)$	$\epsilon_+(\%)$
D_1 (1P1)	0.0024	1.00	0.0024	0.28±0.02	0.78±0.03
D_1 (3P1)	0.0084	1.00	0.0084	0.28±0.05	0.92±0.08
D_2 (3P2)	0.0084	0.312	0.0026	0.39±0.05	0.88±0.08
Nonresonant	0.0036	1.00	0.0036	0.24±0.02	0.78±0.03
Total	0.0227		0.0170		

subtract it from the raw yield to obtain the numbers of reconstructed $B \to D^*\ell\nu$ candidates.

4.8 Efficiencies

To obtain reconstruction efficiencies, we generated events containing $B \to D^*\ell\bar{\nu}$ ($D^* \to D\pi$) using the EVT generator, which is based on the ISGW2 model [23]. The events were passed through a full GEANT detector simulation, and PASS2 offline analysis. We then analyzed the tagged signal candidates. Figure 4.13 shows the resulting efficiency as a function of pion momentum for both $\ell - \pi^+$ and $\ell - \pi^0$ analyses.

Table 4.5: The symbols for reconstruction efficiencies of the respective $B \to D^*\ell\nu(D^* \to D\pi)$ modes.

B Decay Mode	Efficiency
$\bar{B}^0 \to D^{*+}\ell^-\bar{\nu}_\ell$ $(D^{*+} \to D^0\ \pi^+)$	ϵ_{0+}
$B^- \to D^{*0}\ell^-\bar{\nu}_\ell$ $(D^{*0} \to D^0\pi^0)$	ϵ_{-0}
$\bar{B}^0 \to D^{*+}\ell^-\bar{\nu}_\ell$ $(D^{*+} \to D^+\pi^0)$	ϵ_{00}

4.9 Relationship of Measurement to Decay Rates

The numbers of reconstructed $\ell - \pi^+$ and $\ell - \pi^0$ signal candidates, N_+ and N_0, have the following relationships to the branching fractions:

$$N_+ = 2 \times 2 \times N_{B\bar{B}} f_{00} \times \epsilon_{0+} \times \mathcal{B}(\bar{B}^0 \to D^{*+}\ell^-\bar{\nu}_\ell) \times \mathcal{B}(D^{*+} \to D^0\pi^+) \qquad (4.11)$$

and

$$\begin{aligned} N_0 &= 2 \times 2 \times N_{B\bar{B}} f_{+-} \times \epsilon_{-0} \times \mathcal{B}(B^- \to D^{*0}\ell^-\bar{\nu}_\ell) \times \mathcal{B}(D^{*0} \to D^0\pi^0) \\ &+ 2 \times 2 \times N_{B\bar{B}} f_{00} \times \epsilon_{00} \times \mathcal{B}(\bar{B}^0 \to D^{*+}\ell^-\bar{\nu}_\ell) \times \mathcal{B}(D^{*+} \to D^+\pi^0)\ , \end{aligned} \qquad (4.12)$$

where f_{00} (f_{+-}) is the fraction of neutral (charged) B mesons in $\Upsilon(4S)$ events. The symbols for reconstruction efficiencies for each decay mode are defined in Table 4.5. Two factors of 2 enter in these expressions because each $B\bar{B}$ event contains two B mesons, and we add the signals for electrons and muons. Solving for the branching fractions,

$$\mathcal{B}(\bar{B}^0 \to D^{*+}\ell^-\bar{\nu}_\ell) = \frac{N_+}{4N_{B\bar{B}} f_{00}\epsilon_{0+}\mathcal{B}(D^{*+} \to D^0\pi^+)} \qquad (4.13)$$

$$\begin{aligned}\mathcal{B}(B^- \to D^{*0}\ell^-\bar{\nu}_\ell) &= \frac{N_0 - 4N_{B\bar{B}}f_{00}\epsilon_{00}\mathcal{B}(\bar{B}^0 \to D^{*+}\ell^-\bar{\nu}_\ell)\mathcal{B}(D^{*+} \to D^+\pi^0)}{4N_{B\bar{B}}f_{+-}\epsilon_{-0}\mathcal{B}(D^{*0} \to D^0\pi^0)} \\ &= \frac{N_0 - N_+\frac{\epsilon_{00}\mathcal{B}(D^{*+}\to D^+\pi^0)}{\epsilon_{0+}\mathcal{B}(D^{*+}\to D^0\pi^+)}}{4N_{B\bar{B}}f_{+-}\epsilon_{-0}\mathcal{B}(D^{*0} \to D^0\pi^0)} \end{aligned} \tag{4.14}$$

Dividing equation (4.14) by equation (4.13), assuming that $\epsilon_{-0} = \epsilon_{00}$ as shown in Figure 4.13 (top), and defining $n \equiv \frac{N_+\epsilon_{00}}{N_0\epsilon_{0+}}$, we get

$$\frac{\mathcal{B}(B^- \to D^{*0}\ell^-\bar{\nu}_\ell)}{\mathcal{B}(\bar{B}^0 \to D^{*+}\ell^-\bar{\nu}_\ell)} = \frac{f_{00}[\mathcal{B}(D^{*+} \to D^0\pi^+) - n\mathcal{B}(D^{*+} \to D^+\pi^0)]}{nf_{+-}\mathcal{B}(D^{*0} \to D^0\pi^0)} \tag{4.15}$$

so that

$$\alpha \equiv \frac{f_{+-}}{f_{00}}\frac{\mathcal{B}(B^- \to D^{*0}\ell^-\bar{\nu}_\ell)}{\mathcal{B}(\bar{B}^0 \to D^{*+}\ell^-\bar{\nu}_\ell)} \equiv \frac{\mathcal{B}(D^{*+} \to D^0\pi^+) - n\mathcal{B}(D^{*+} \to D^+\pi^0)}{n\mathcal{B}(D^{*0} \to D^0\pi^0)}\,. \tag{4.16}$$

The determination of n is model-dependent if we are required to extrapolate one or the other of the reconstructed modes over regions of zero acceptance, such as at very low pion momentum. However, if we take the ratio in restricted regions where both modes have finite and well-measured acceptance, it can be expected to be model-independent. We thus take the ratio of the $\ell - \pi^+$ to $\ell - \pi^0$ signals as a function of π momentum, corrected for the reconstruction efficiencies in each bin, and fit to a constant. We fit in the region $0.090 - 0.220\ GeV/c$ of π momentum; below this region the charged pion tracking efficiency drops rapidly and has a large systematic uncertainty. The fit yields an overall value $n = 0.667 \pm 0.037$ (Figure 4.14). Using this value and the D^* branching fractions shown in Table 4.6, we obtain $\alpha = 1.144 \pm 0.091$, where the error is statistical only.

Table 4.6: Branching fraction of $D^* \to D\pi$.

Mode	Branching Fraction	Reference
$D^{*+} \to D^0\pi^+$	$(67.6 \pm 0.8)\%$	[44]
$D^{*+} \to D^+\pi^0$	$(30.7 \pm 0.7)\%$	[44]
$D^{*0} \to D^0\pi^0$	$(61.9 \pm 2.9)\%$	[5]

4.10 Systematic Errors

The systematic uncertainty on this measurement of α is due to the uncertainty in determining the ratio n and the uncertainty in the D^* branching fractions. The reconstructions of $\ell - \pi^0$ and $\ell - \pi^+$ candidates have many features in common, and therefore have many shared systematic errors which cancel at least partially in taking the ratio. The common uncertainties are from lepton detection and identification and the background subtractions. The principal difference between the two reconstructions is in the reconstruction of the pions.

We first discuss the sources that are common to both reconstructions. The uncertainty on the continuum subtraction is obtained by changing the scaling factor up and down by 3%. The uncertainty on the lepton fake probability is 30%. The systematic uncertainty on the lepton identification efficiency has been determined to be 2.5% [35]. The systematic uncertainties from each of these sources is estimated by varying the affected quantity and observing the shift of the result. These errors cancel at least partially in taking the ratio n.

The estimation of uncorrelated background depends on accurate modeling of the data by

Monte Carlo. The overall shape of the $\widetilde{\mathcal{M}}_\nu^2$ distribution of the uncorrelated background is dominated by phase space, i.e., a hard lepton and soft pion distributed isotropically will produce a distribution similar to that shown. However, because this analysis has high statistical precision, we rely on the Monte Carlo B decay generator to simulate the shape correctly in greater detail. Because we depend only on the overall shape of the $\widetilde{\mathcal{M}}_\nu^2$ distribution (through SB scaling) and not on its normalization for this evaluation, the Monte Carlo will be sufficiently good if there is a good match between observed distributions in $\widetilde{\mathcal{M}}_\nu^2$, which depends on the magnitude of the lepton and pion momenta and the opening angle between them. A simple overall test of this match is in the $\widetilde{\mathcal{M}}_\nu^2$ distribution of wrong sign ($\ell^\pm - \pi^\pm$) candidates, where no signal is expected. An analysis identical to that performed with right sign $\ell - \pi^+$ candidates yields a signal of -144 ± 117, consistent with zero. The distribution in data and the corresponding result from Monte Carlo simulation are shown in Figure 4.15. We take the absolute sum, $|-144| + 117 = 261$, as an estimate of the systematic uncertainty due to modeling, corresponding to a fractional uncertainty on background in the PK region of 4.1%. This fraction of uncorrelated background in the right sign $\ell - \pi^+$ translates to 2.3% of the net signal. For the $\ell - \pi^0$, the corresponding uncertainty is 2.4%. Although these two uncertainties are believed to be largely correlated such that they must cancel at least partially in taking the ratio, we take the error on n to be equal to the larger one, 2.4%. The summary of wrong sign $\ell - \pi^+$ candidates and background subtractions is shown in Table 4.7. The distributions in data and Monte Carlo are shown in Figure 4.15 (normalized to the sideband).

Table 4.7: Summary of wrong sign $\ell - \pi^+$ candidates and background subtractions.

Source	SG region	SB region
Data, $\Upsilon(4S)$	7630	34766
Data, continuum (scaled)	1327±50	6130±107
Fake leptons (cont sub)	22.5±0.8	109.3±1.5
Fake and continuum subtracted	6281±101	28527±215
Scaled uncorrelated background	6425± 60	28527±202
Yield	-144± 117	0

To estimate the uncertainty due to our lack of knowledge of the B semileptonic decays to D^{**}, we vary both the total branching fraction and the mix of resonances comprising D^{**}. The branching fraction, which we took to be $(1.70 \pm 0.33)\%$ for each D^* charge averaged over B charges, is varied upward and downward by the amount of the error, holding fixed the relative contributions of the different modes. We recorded excursions of 0.7% and 0.5% for $\ell - \pi^0$ and $\ell - \pi^+$, respectively. We also allow each mode in turn to saturate the rate and take the maximum excursion of the result as a systematic uncertainty. We thus obtain errors of 1.1%, 1.6%, and 1.2%, for $\ell - \pi^0$, $\ell - \pi^+$, and n.

The systematic uncertainty on tracking efficiency for slow charged pions has been measured by CLEO [32] [45] [46], and determined to be 5%. The uncertainty on the efficiency ratio of slow neutral pions to slow charged pions was determined at CLEO to be 7% [46]. As the absolute efficiency for neutral pion reconstruction is determined by charged pion efficiency and

this efficiency ratio, the quadratic sum of their uncertainties gives a systematic uncertainty of 8.6% [32] on the neutral pion efficiency.

To estimate the systematic error on the evaluation of fake π^0 mesons in $\ell - \pi^0$, we vary the fake scaling factor up and down by the amount of its statistical error and repeat the analysis. We take the maximum excursion of 1.6% to be the systematic uncertainty from this source. We also repeat the analysis without excluding the $\gamma\gamma$ mass region $0.014 - 0.015$ GeV/c^2 and find that this shifts the result by 0.7%. We add the two numbers quadratically to get a systematic error on the π^0 fit of 1.7%.

We find the total systematic errors to be 9.5% for $\ell - \pi^0$, 6.3% for $\ell - \pi^+$, and 7.7% for n. This results in an uncertainty of 11.0% on α. The additional uncertainty from the D^* branching fractions is 6.3%. All the systematic uncertainties are summarized in Table 4.8.

By measuring the ratio of partially reconstructed $B \to D^* \ell \nu$ decays in the $\ell - \pi^+$ and $\ell - \pi^0$ channels as a function of pion momentum, we obtain a measurement of the ratio:

$$\frac{f_{+-}}{f_{00}} \frac{\tau_+}{\tau_0} = 1.144 \pm 0.091 \pm 0.146 \ .$$

This result is in good agreement with published CLEO values (Table 4.9).

Using the ratio of B^+ and B^0 lifetimes from a recent world average [59],

$$\frac{\tau_+}{\tau_0} = 1.066 \pm 0.024 \ , \tag{4.17}$$

we obtain the ratio of the charged and neutral B mesons production at the $\Upsilon(4S)$ resonance:

$$\frac{f_{+-}}{f_{00}} = 1.073 \pm 0.085 \pm 0.119 \pm 0.072 \pm 0.024 \ , \tag{4.18}$$

Table 4.8: Summary of systematic errors.

Source	$\ell - \pi^0$	$\ell - \pi^+$	n	α
Continuum subtraction	0.2%	0.2%	0.2%	0.3%
Fake leptons	0.5%	0.5%	0.5%	0.7%
Uncorrelated background	2.4%	2.3%	2.4%	3.4%
D^{**} background	1.1%	1.6%	1.2%	2.0%
Fake π^0 subtraction	1.7%	–	1.7%	2.4%
π efficiency	8.6%	5.0%	7.0%	10.0%
Lepton ID efficiency	2.5%	2.5%	–	–
D^* Branching Fraction	–	–	–	6.3%
Total	9.5%	6.3%	7.7%	12.7%

Table 4.9: Other CLEO measurements of the ratio of the product of production fraction and lifetime for charged and neutral B mesons.

Mode	$\frac{f_{+-}}{f_{00}}\frac{\tau_+}{\tau_0}$
$B \to D^* \ell \bar{\nu}$ [32]	$1.14 \pm 0.14 \pm 0.13$
$B \to \{c\} \ell \bar{\nu}$ [33]	$1.20 \pm 0.12 \pm 0.21$
$B \to \psi K^{(*)}$ [34]	$1.11 \pm 0.07 \pm 0.04$

where the first error is statistical, the second is systematic on n, the third is due to the uncertainty on the D^* branching fractions, and the fourth is due to the uncertainty on the B lifetime ratio. We add the systematic errors quadratically to obtain:

$$\frac{f_{+-}}{f_{00}} = 1.071 \pm 0.085 \pm 0.139 \ . \tag{4.19}$$

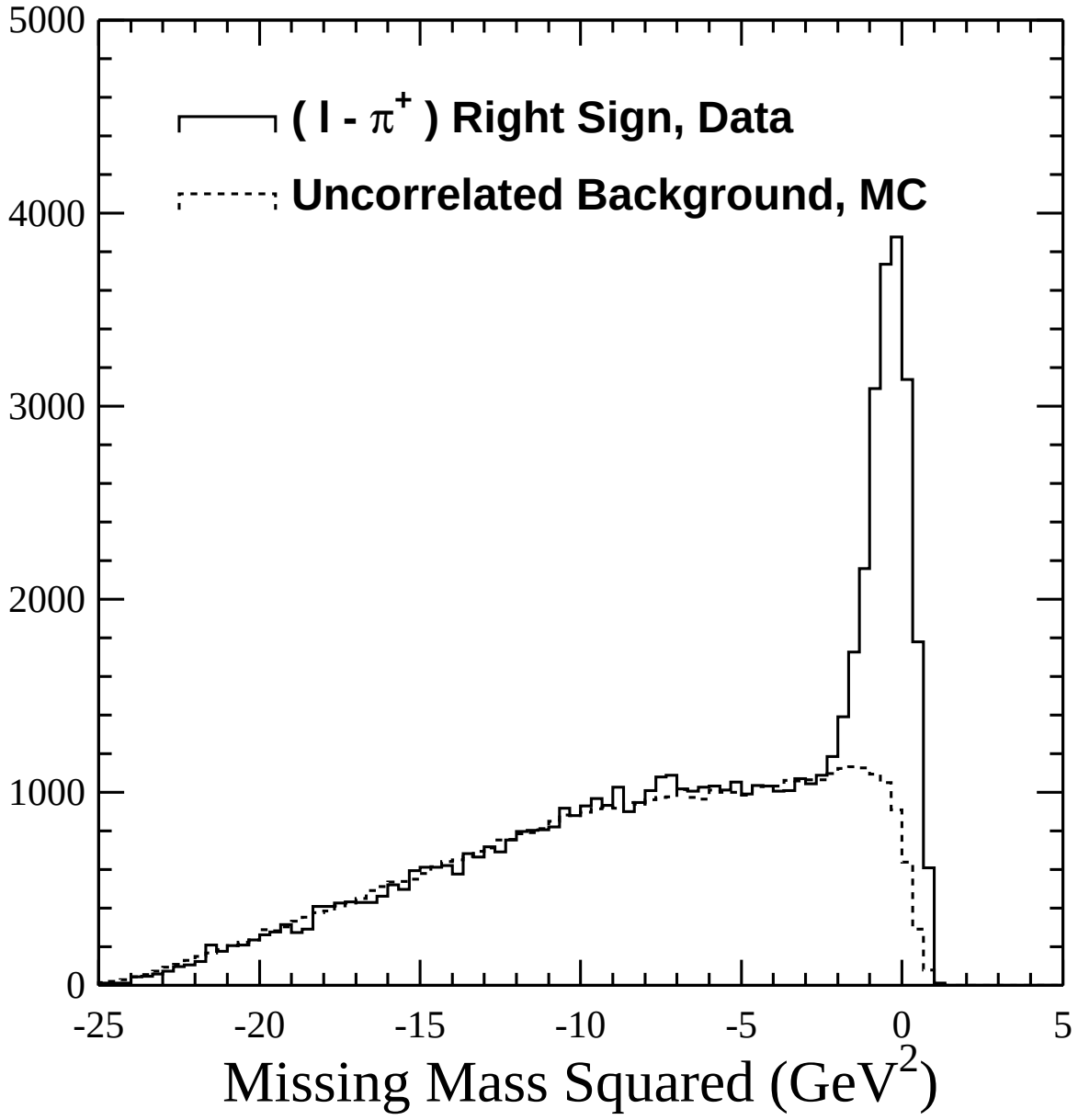

Figure 4.1: The distribution in $\widetilde{\mathcal{M}}_\nu^2$ for the decay $\bar{B}^0 \to D^{*+}\ell^-\bar{\nu}_\ell$.

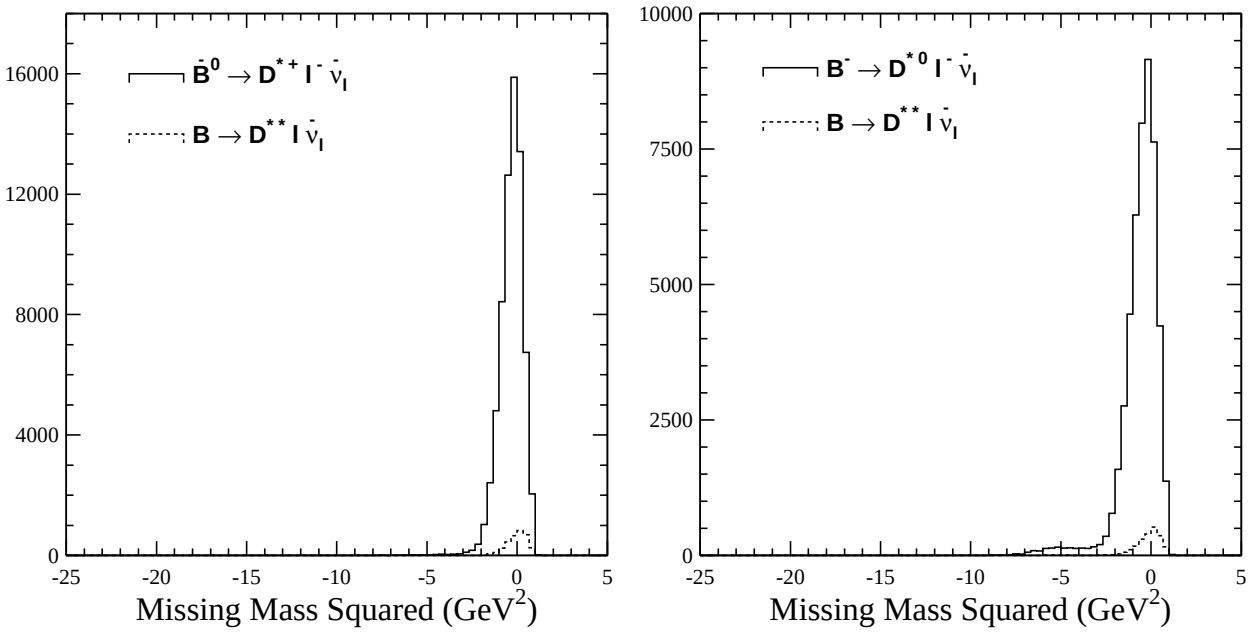

Figure 4.2: The distribution in $\widetilde{\mathcal{M}}_\nu^2$ for signal candidates (solid histogram), obtained from Monte Carlo simulation: (left) $\bar{B}^0 \to D^{*+}\ell^-\bar{\nu}_\ell$ and $\bar{B} \to D^*\pi\ell^-\bar{\nu}_\ell$; (right) the combined $B^- \to D^{*0}\ell^-\bar{\nu}_\ell$, $D^{*0} \to D^0\pi^0$ plus $\bar{B}^0 \to D^{*+}\ell^-\bar{\nu}_\ell$, $D^{*+} \to D^+\pi^0$. The dashed histogram shows the estimated relative contribution from decays $\bar{B} \to D^{**}\ell^-\bar{\nu}_\ell$ (correlated background).

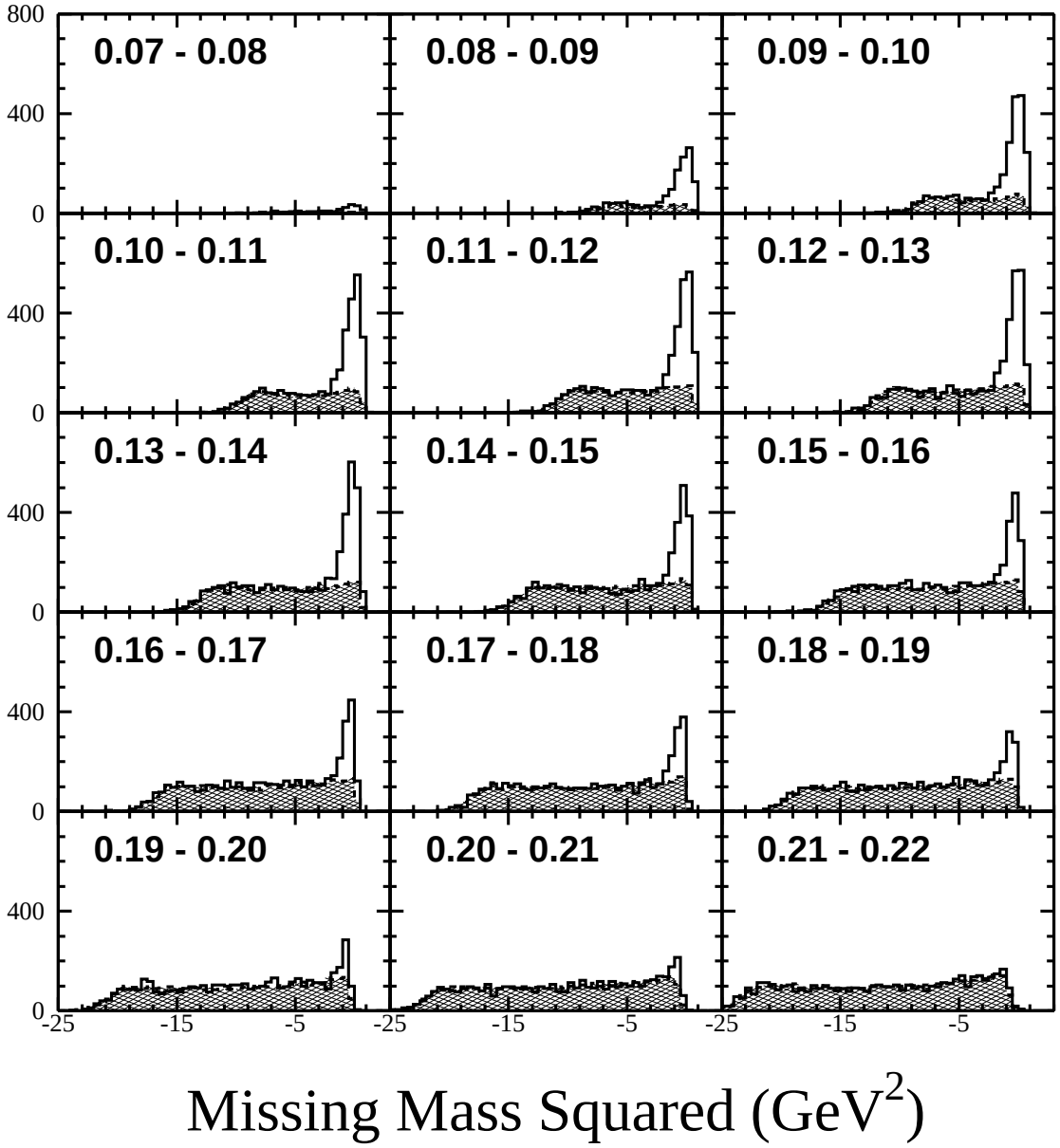

Figure 4.3: Distributions in $\widetilde{\mathcal{M}}_\nu^2$ for the decay $\bar{B}^0 \to D^{*+}\ell^-\bar{\nu}_\ell$, for 10 MeV/c bins of pion momentum. The plot shows right sign data, with continuum and fake lepton contributions subtracted (solid histograms) and uncorrelated background estimated by Monte Carlo (filled histograms).

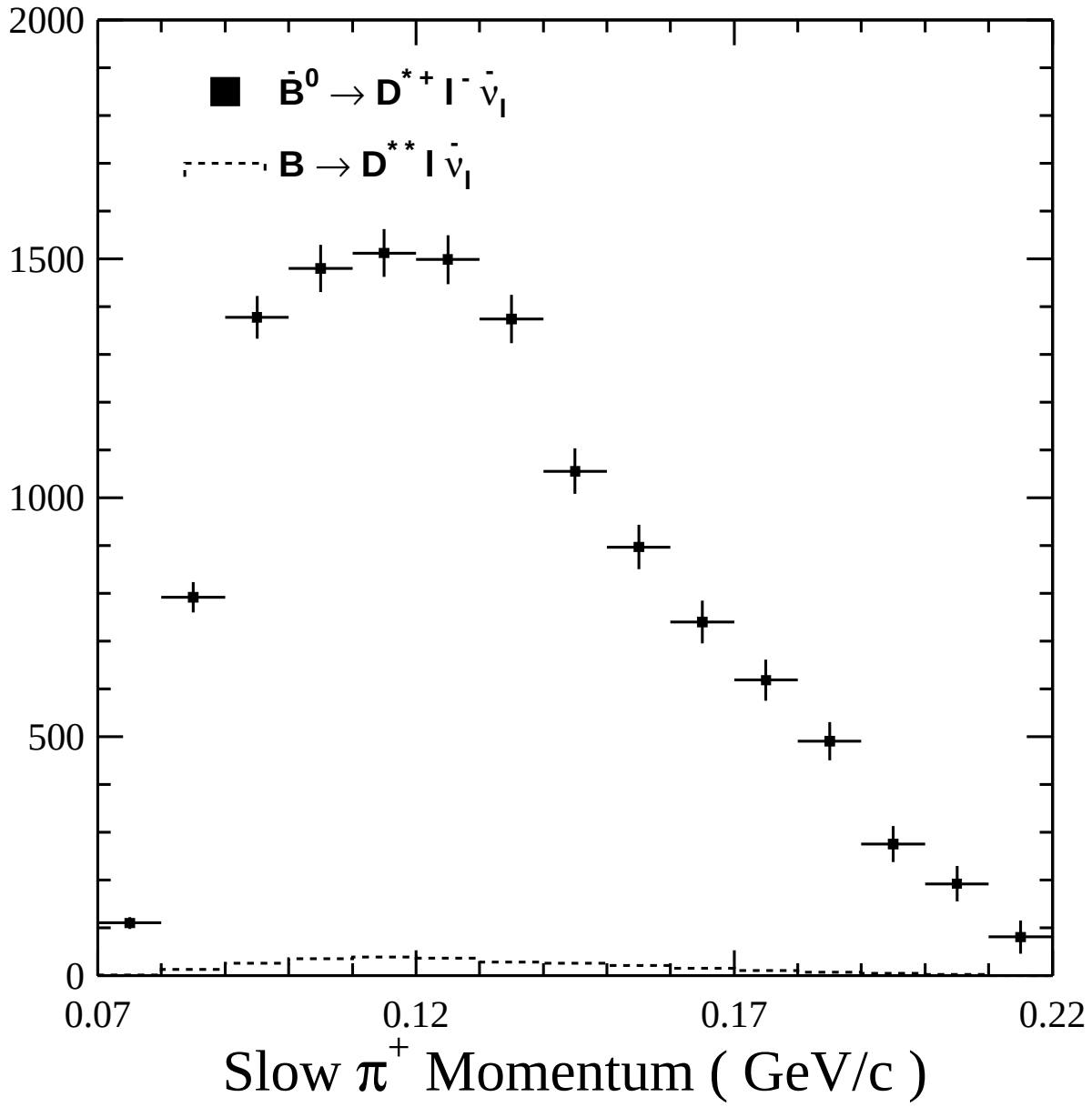

Figure 4.4: Raw yield in data of *"peak"* tags in $\ell - \pi^+$ as a function of π^+ momentum, with estimated contribution from correlated background (dashed).

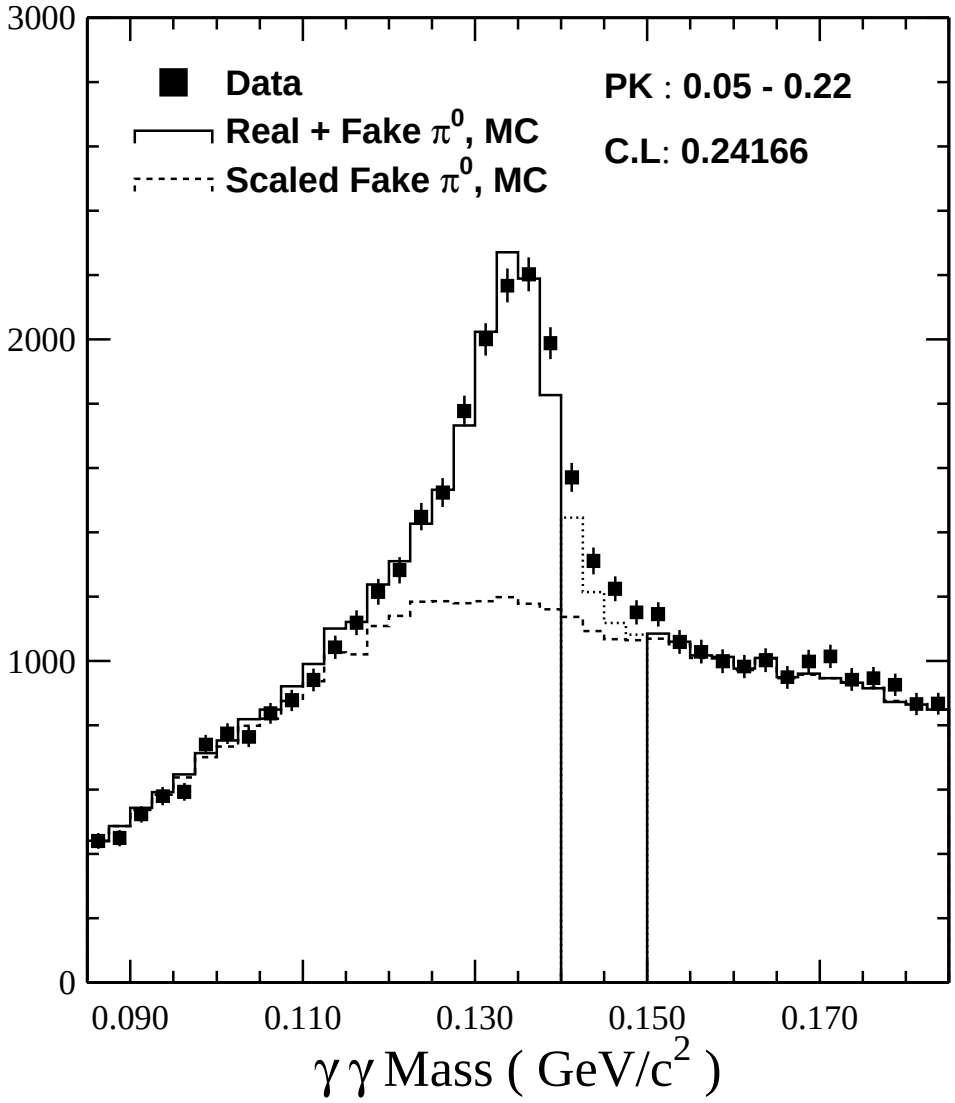

Figure 4.5: Fit of $M_{\gamma\gamma}$ distribution of π^0 candidates comprising $\ell - \pi^0$ PK tags. The region $0.140 - 0.150\ GeV/c^2$ is omitted from the fit in this and all other fits of $M_{\gamma\gamma}$ described in this thesis.

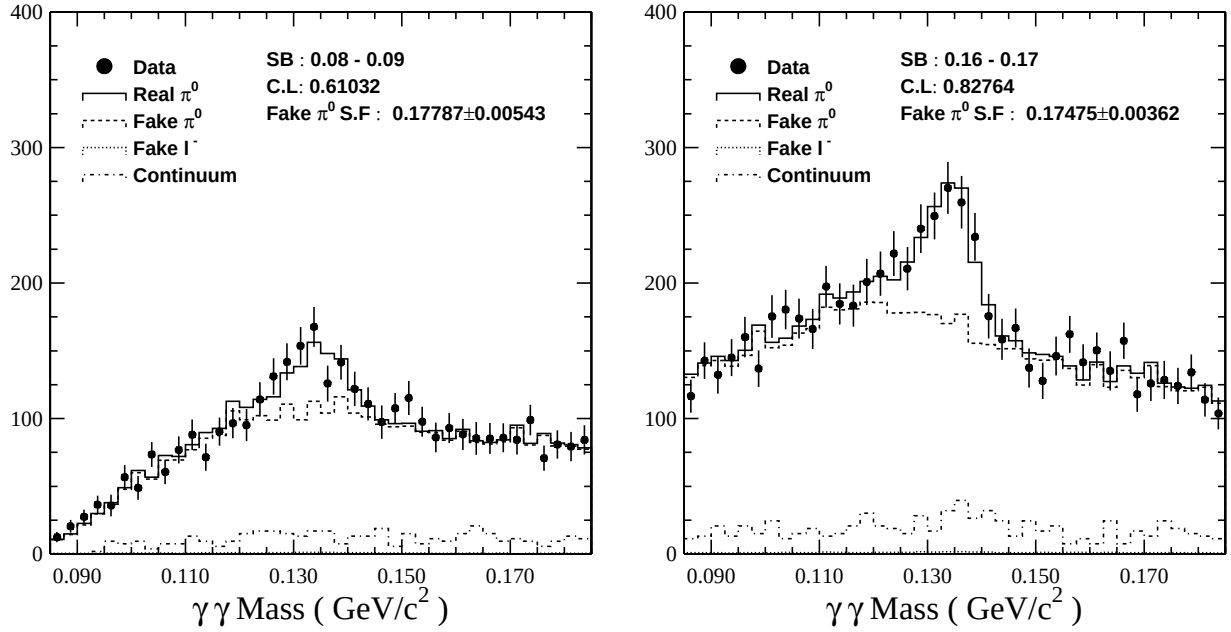

Figure 4.6: Fits of $M_{\gamma\gamma}$ to Monte Carlo-generated real and fake π^0 shapes for $\ell-\pi^0$ SB candidates. Shown are plots for two bins of π^0 momentum.

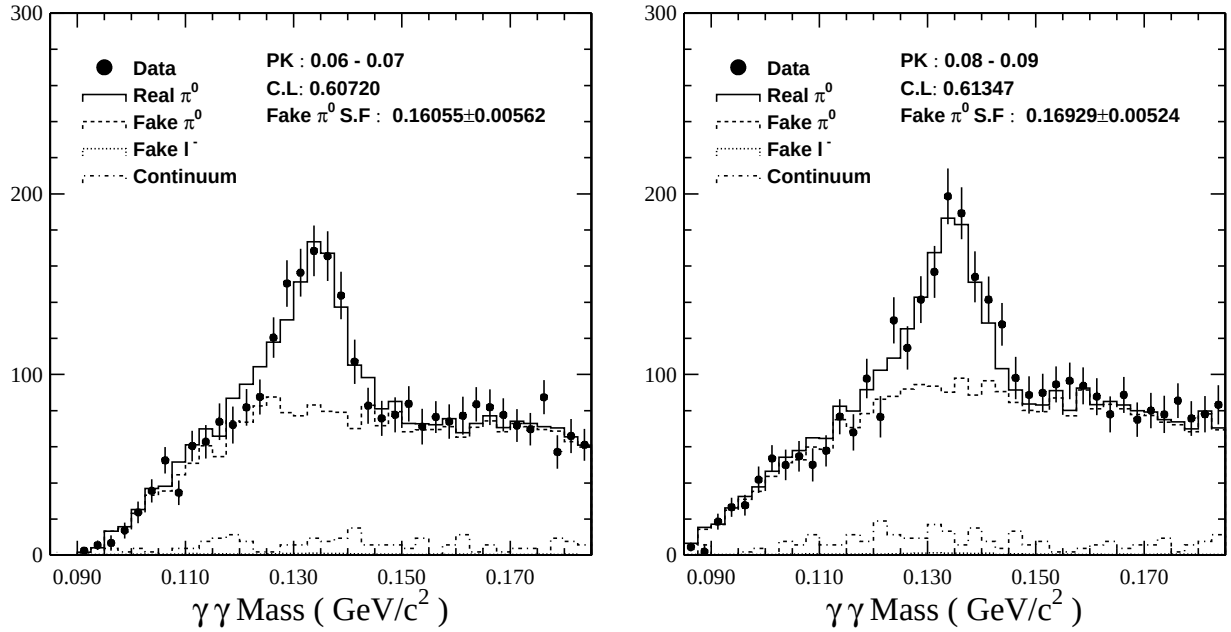

Figure 4.7: Fits of $M_{\gamma\gamma}$ to Monte Carlo-generated real and fake π^0 shapes for $\ell-\pi^0$ SG candidates. Shown are plots for two bins of π^0 momentum.

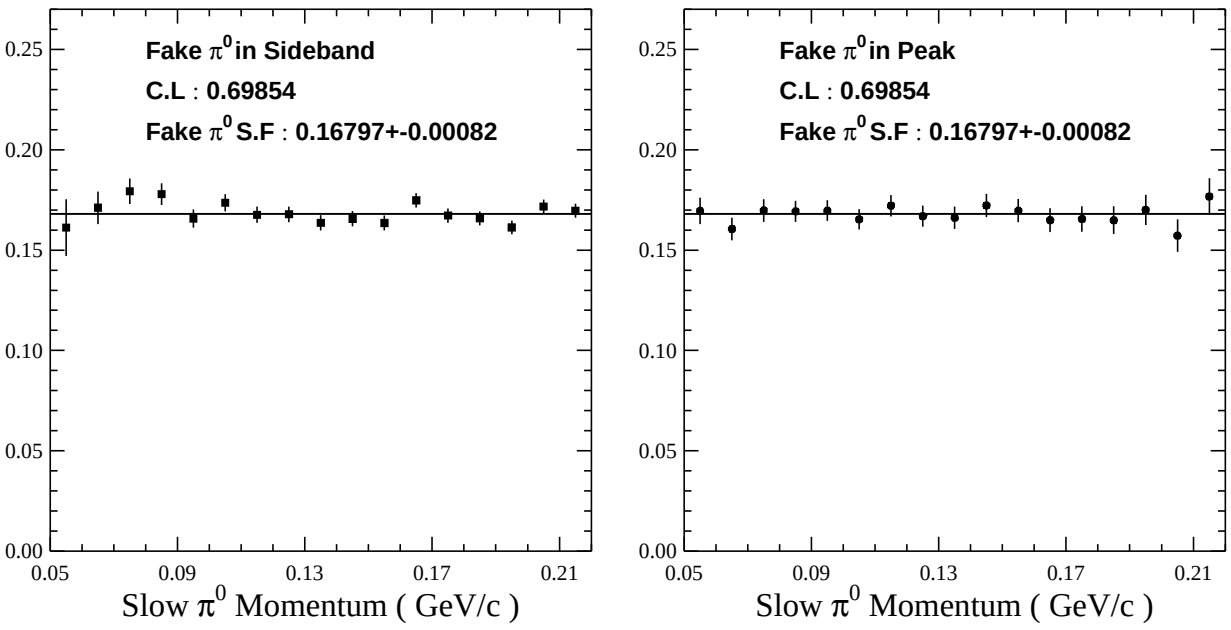

Figure 4.8: Fit of fake π^0 scaling factors to a constant. Scaling factors are plotted as a function of momentum for SB (left) and PK (right) candidates and fitted simultaneously to a single constant.

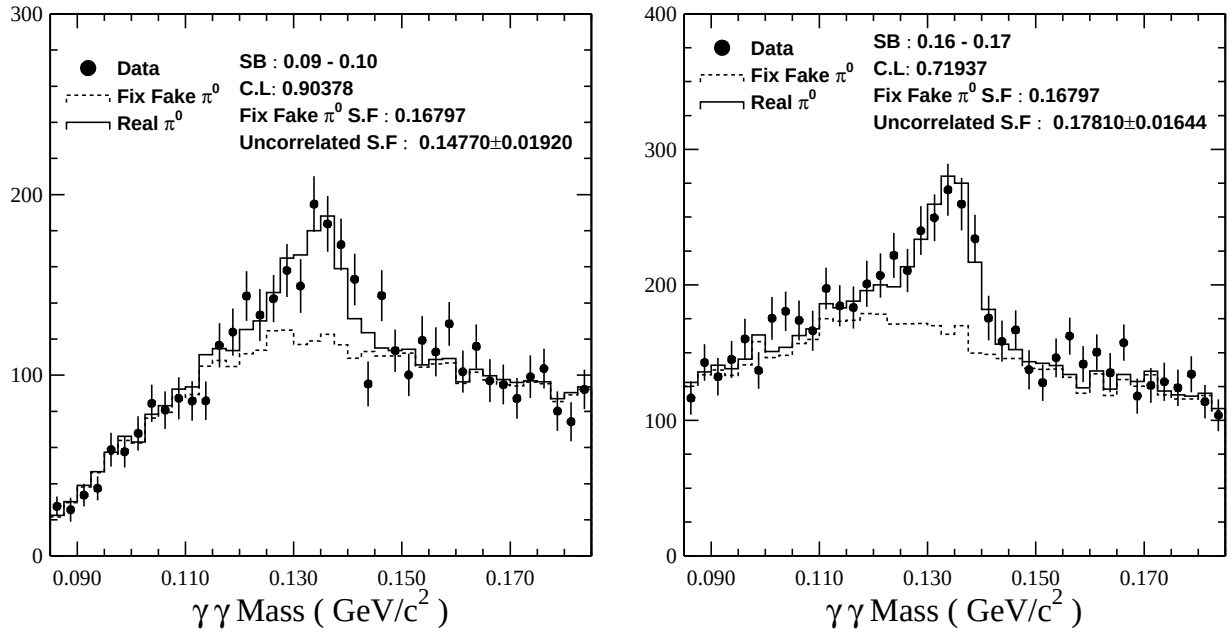

Figure 4.9: Fits of $M_{\gamma\gamma}$ to Monte Carlo-generated real and fake π^0 shapes for $\ell - \pi^0$ SB candidates. The fake normalization is fixed. The real π^0 contribution is dominated by uncorrelated background candidates. Shown are plots for two bins of π^0 momentum.

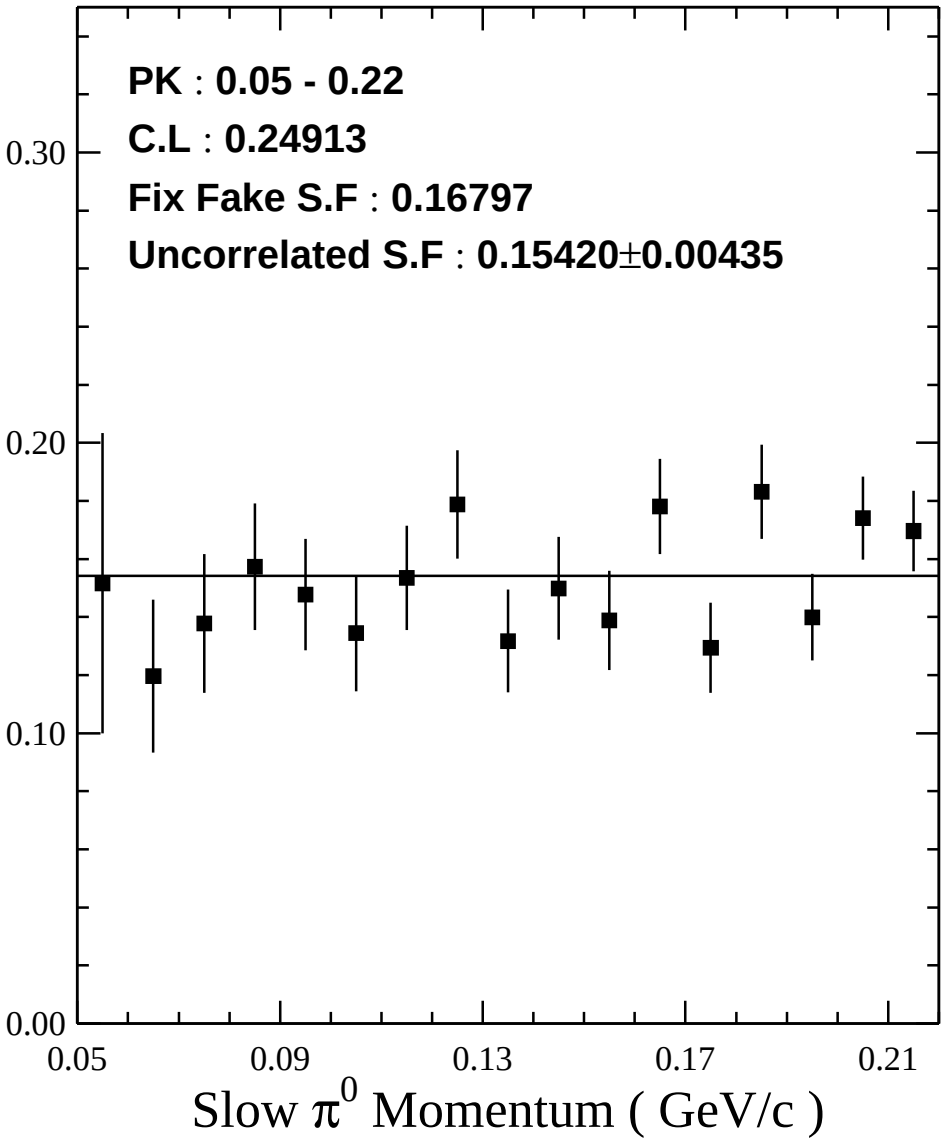

Figure 4.10: Fit to determine Monte Carlo scaling factor for uncorrelated background candidates. Scaling factors obtained by fitting in momentum bins are plotted as a function of momentum and fitted to a constant.

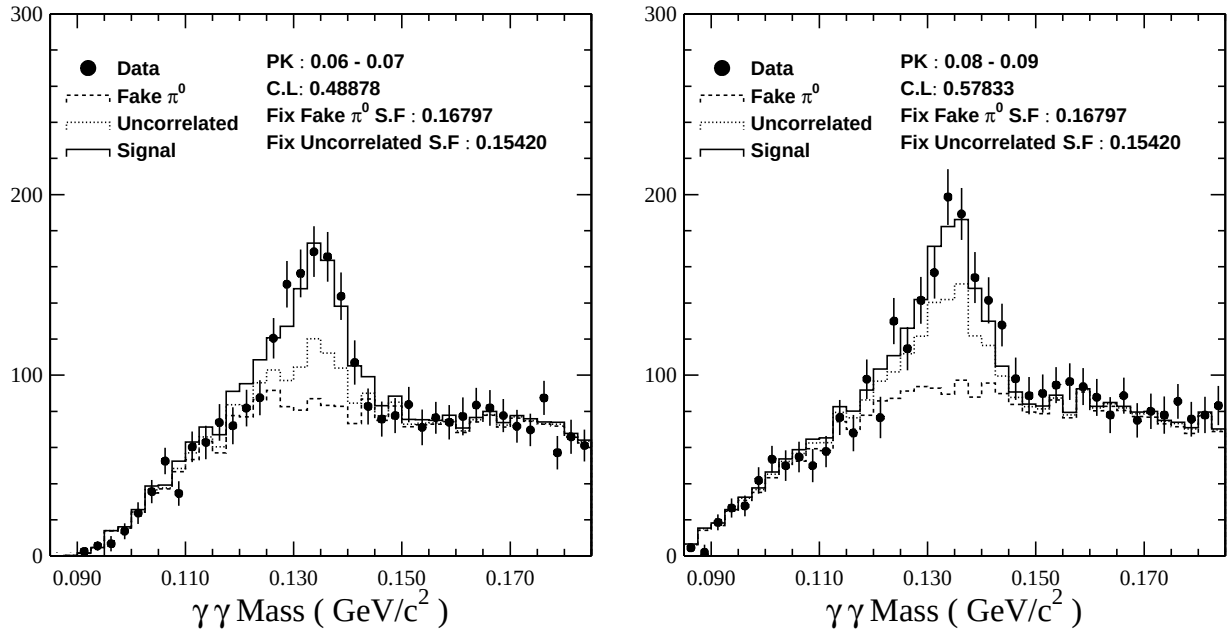

Figure 4.11: Fits of $M_{\gamma\gamma}$ to Monte Carlo-generated real (peak), real (uncorrelated background), and fake π^0 shapes for $\ell - \pi^0$ PK candidates. The fake and uncorrelated background normalizations are fixed. Shown are plots for two bins of π^0 momentum.

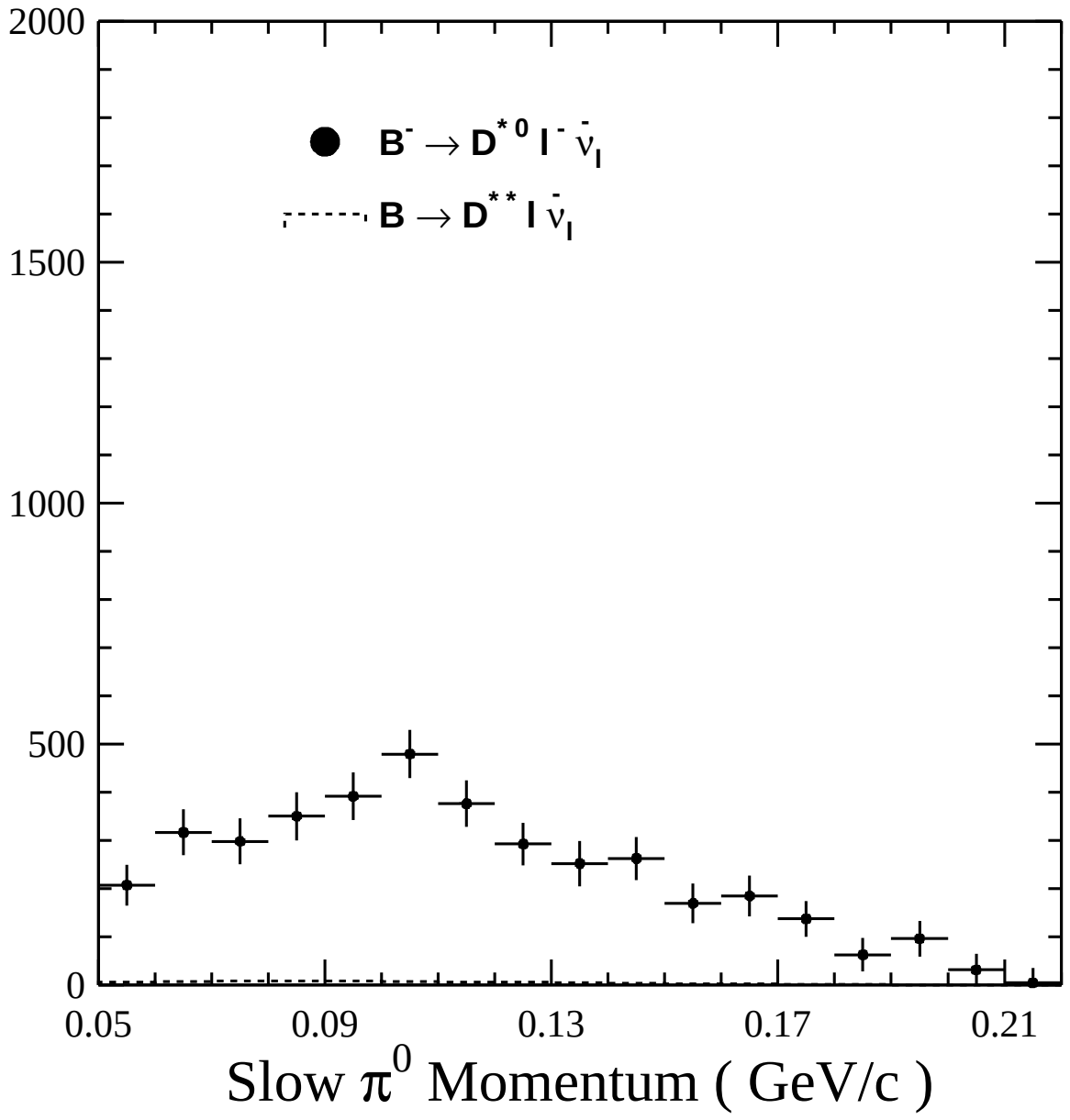

Figure 4.12: Raw yield in data of "peak" tags in $\ell - \pi^0$ as a function of π^0 momentum (filled circles histogram), with estimated contribution from correlated background (dashed).

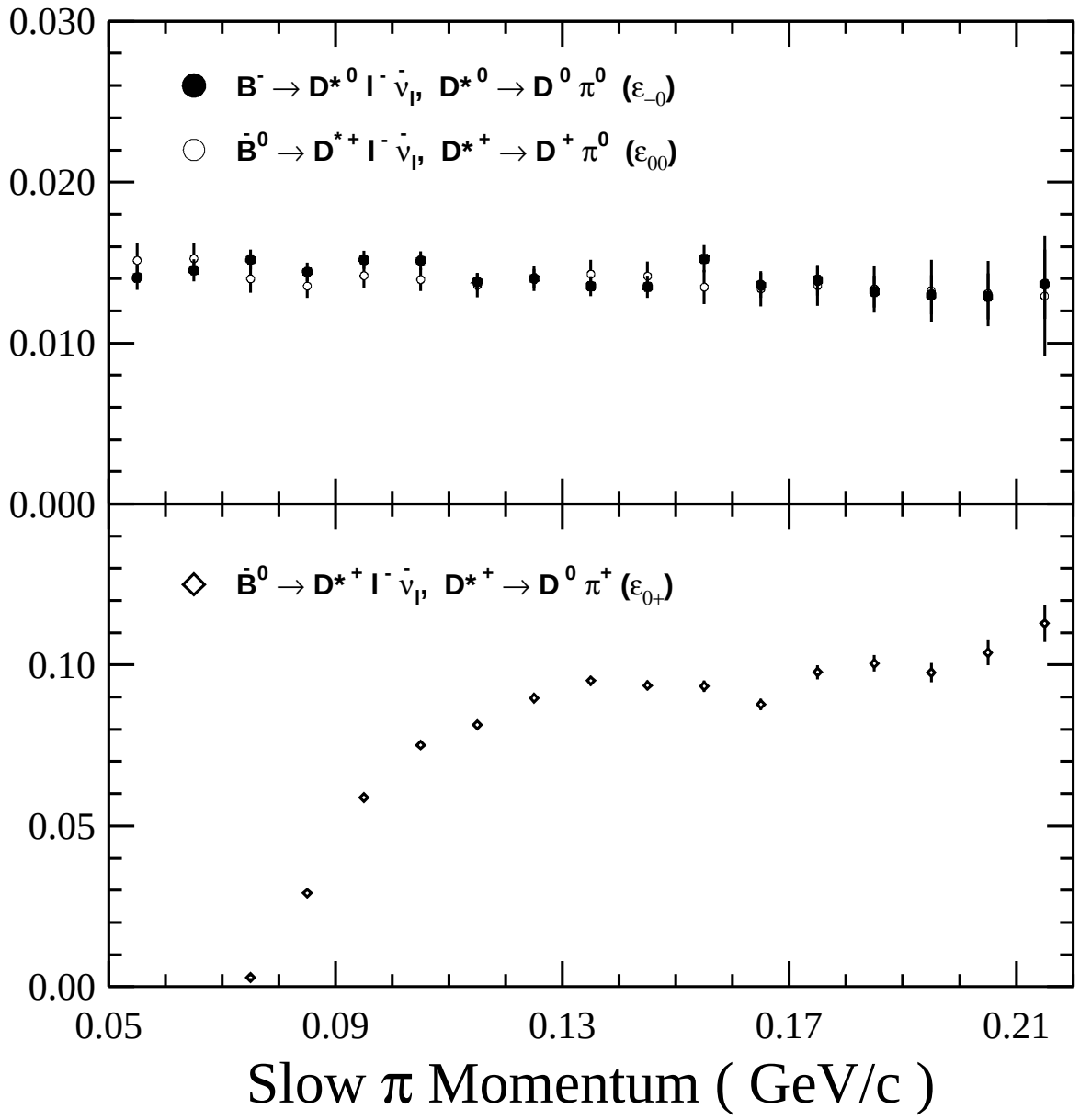

Figure 4.13: Efficiencies for reconstruction of decays $\bar{B}^0 \to D^{*+}\ell^-\bar{\nu}_\ell$ and $B^- \to D^{*0}\ell^-\bar{\nu}_\ell$ via partial reconstruction as a function of π momentum: $\ell - \pi^0$ (top) and $\ell - \pi^+$ (bottom) analysis.

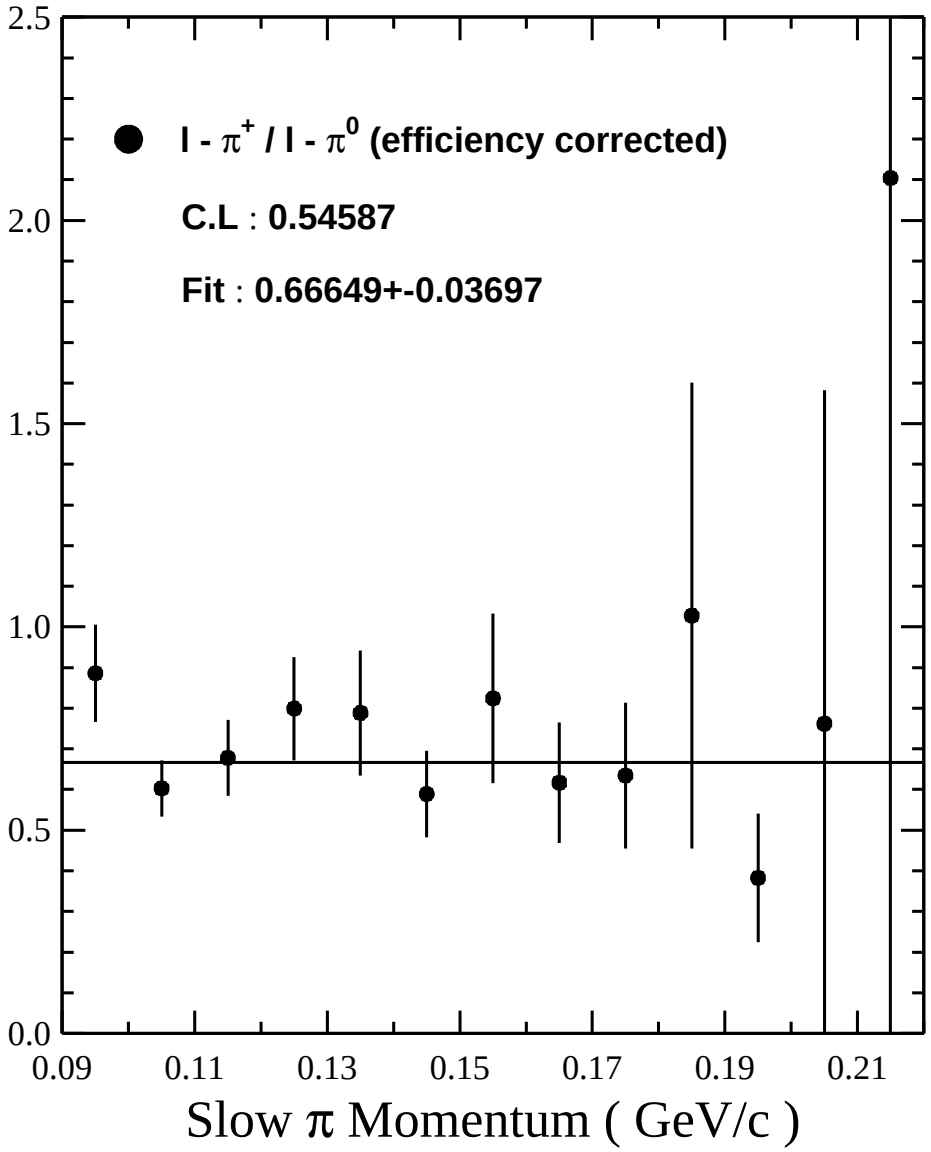

Figure 4.14: Efficiency-corrected ratio of $\ell - \pi^+$ to $\ell - \pi^0$ candidates in bins of π momentum. The values are fitted to a constant.

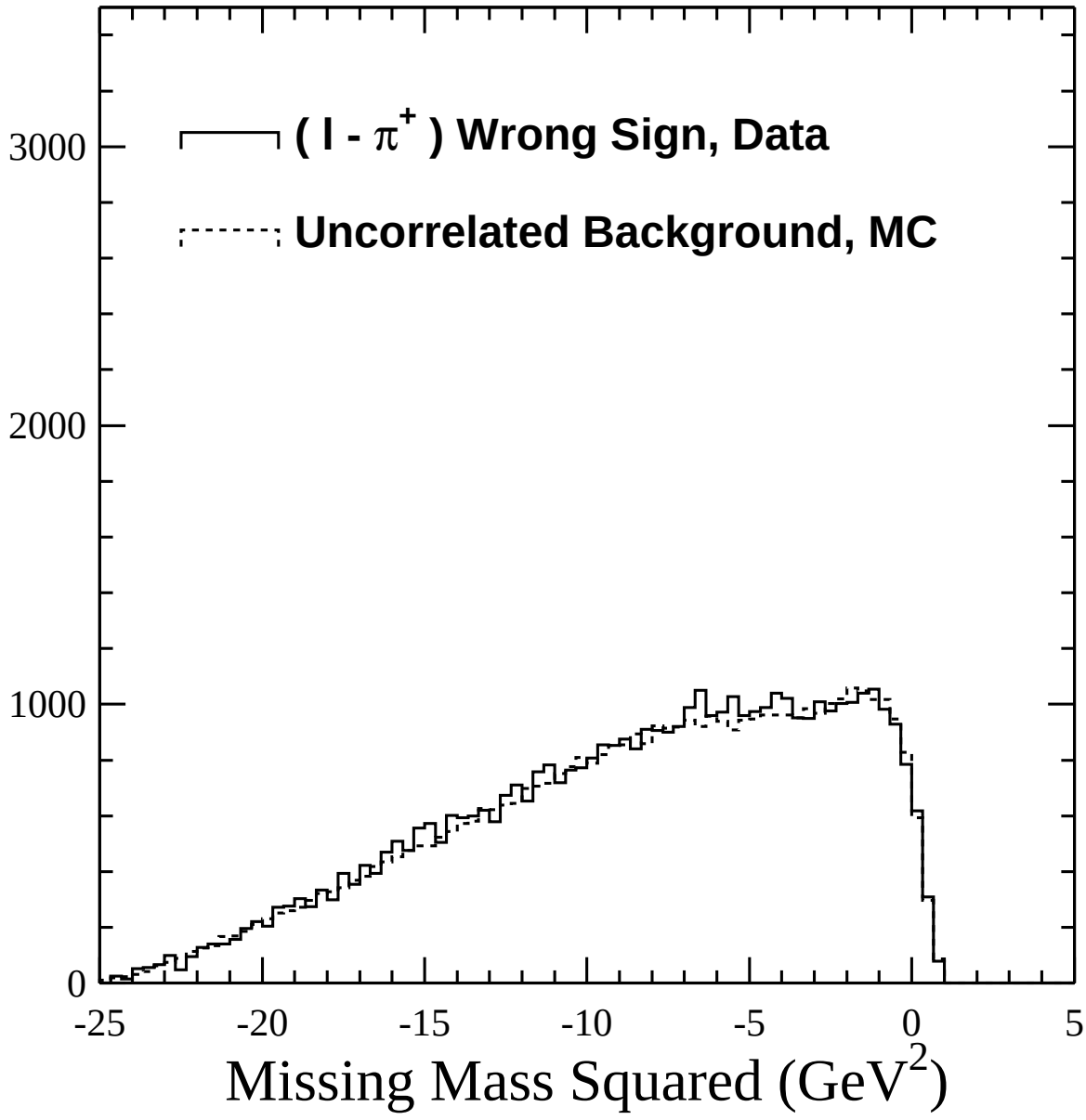

Figure 4.15: The squared missing mass distribution for the decay $\bar{B}^0 \to D^{*+}\ell^-\bar{\nu}_\ell$. The plot shows the comparison between wrong sign data and wrong sign normalized Monte Carlo.

Chapter 5

Conclusion

This thesis presents a measurement of the relative branching fraction of the $\Upsilon(4S)$ to charged and neutral B mesons using the partial reconstruction of the semileptonic decays $\bar{B}^0 \to D^{*+}\ell^-\bar{\nu}_\ell$ and $B^- \to D^{*0}\ell^-\bar{\nu}_\ell$.

From this measurement, we derive the ratio of the product of production fraction and semileptonic branching fraction for charged and neutral B mesons, $\frac{f_{+-}b_+}{f_{00}b_0}$. Assuming equality of semileptonic widths for all hadrons containing a b-quark, the ratio of semileptonic branching fraction, $\frac{b_+}{b_0}$, is equal to the lifetime ratio $\frac{\tau_+}{\tau_0}$. We then obtain the ratio of charged and neutral B mesons production at the $\Upsilon(4S)$. This measurement and its error apply to all exclusive branching fractions measured at the $\Upsilon(4S)$.

The Ratio of the Charged and Neutral B Mesons Production at the $\Upsilon(4S)$ Resonance

Using 2.729 fb^{-1} of data taken at the $\Upsilon(4S)$ resonance peak, and 1.430 fb^{-1} taken at a center-of-mass energy which is lower by 60 MeV (off-resonance) from the CLEO data sample, we have reconstructed the decay $\bar{B}^0 \to D^{*+}\ell^-\bar{\nu}_\ell$ with $D^{*+} \to D^0\pi^+$. We have also reconstructed the decay $B^- \to D^{*0}\ell^-\bar{\nu}_\ell$ with $D^{*0} \to D^0\pi^0$ and $\bar{B}^0 \to D^{*+}\ell^-\bar{\nu}_\ell$ with $D^{*+} \to D^+\pi^0$. We have measured the ratio of the product of production fraction and lifetime for charged and neutral B mesons,

$$\frac{f_{+-}}{f_{00}}\frac{\tau_+}{\tau_0} = 1.144 \pm 0.091 \pm 0.146 \ ,$$

and using the current existing B lifetimes ratio measurements [59], we obtain the ratio of charged and neutral B meson production at the $\Upsilon(4S)$ resonance:

$$\frac{f_{+-}}{f_{00}} = 1.071 \pm 0.085 \pm 0.139 \ . \tag{5.1}$$

References

[1] S. Weinberg, Phys. Rev. Lett. **19**, 1264 (1967); S. Glashow, Nucl. Phys. **B22**, 579 (1961); A. Salam, Nobel Symposium, 167 (1968).

[2] P. W. Higgs, Phys. Lett. **12**, 232 and **13**, 508 (1964).

[3] J. Goldstone, A. Salam, and S. Weinberg, Phys. Rev. **127**, 965 (1962).

[4] J. Timmer, Preceedings of the Moriond Workshop on Antiproton-Proton Physics and the W Discovery Editions Frontieres, J. Tran Thanh Van, 593 (1983).

[5] Particle Data Group, C. Caso *et al.*, The Review of Particle Physics, The European Physical Journal. **C3** (1999).

[6] R. P. Feynman and M. Gell-Mann, Phys. Rev. **109**, 193 (1958).

[7] M. Kobayashi and T. Maskawa, Prog. Theor. Phys. **49**, 652 (1973).

[8] The 2000 Review of Particle Physics (WWW edition), http://pdg.lbl.gov/.

[9] N. Cabibbo, Phys. Rev. Lett. **10**, 531 (1963).

[10] L. Wolfenstein, Phys. Rev. Lett. **51**,1945 (1983).

[11] Particle Data Group, C. Caso *et al.*, Review of Particle Properties, Euro. Phys. Journal. **C**, Vol. 3.

[12] S. W. Herb *et. al.*, Phys. Rev. Lett. **39**, 252 (1977).

[13] C. Berger *et al.*, Phys. Lett. **76B**, 243 (1978);

C. W. Darden *et al.*, Phys. Lett. **78B**, 246 (1978);

J. K. Bienlein *et al.*, Phys. Lett. **78B**, 360 (1978).

[14] D. Andrews *et al.*, Phys. Rev. Lett. **44**, 1108 (1980);

T. Bohringer *et al.*, Phys. Rev. Lett. **44**, 1111 (1980);

G. Finnocchiaro *et al.*, Phys. Rev. Lett. **45**, 222 (1980).

[15] Belle Collaboration, A study of CP violation in B Meson Decay: Technical Design Report, KEK report 95-1 (1995).

[16] Babar Collection, Babar Technical Design Report, SLAC-R-95-457 (1995).

[17] S. Okubo, Phys. Rev. Lett. **5**, 165 (1963);

G. Zweig, CERN Reps. TH-401, 412 (1964);

J. Iizuka, Suppl. Prog. Theory. Phys. **37-38**, 21 (1966).

[18] D. Besson, CLEO internal report CBX 92-23 (1992).

[19] S. Willocq, SLD Collaboration, SLAC-PUB-7942 (1998).

[20] T. Skwarnicki, Decays of b Quarks, HEPSY-95-05 (1995).

[21] N. Isgur, D. Scora, B. Grinstein, and M. B. Wise, Phys. Rev. **D 39**, 799 (1989).

[22] M. Neubert, Phys. Reports **345**, 259 (1994).

[23] N. Isgur and D. Scora, Phys. Rev. **D 52**, 2783 (1995).

[24] J. G. Körner and G. A. Schuler, Phys. Lett. **B 226**, 185 (1989).

[25] R. Kutschke, An angular distribution cookbook, 1996.

[26] M. Wirbel, B. Stech and M. Bauer, Z, Phys. **C 29**, 637 (1985).

[27] B. Gittelman *et al.*, Electron identification with CLEO II, CLEO internal report. CBX 91-82.

[28] Avery, Read, and Trahern, CLEO internal report CSN-212 (1985).

[29] D. Lange, Ph.D. Thesis, University of California, 1999 (unpublished).

[30] R. Brun *et al.*, GEANT v. 3.15, CERN DD/EE/84-1.

[31] P. Lepage, Phys. Rev. **D 42**, 3251 (1990);
D. Atwood and W. Marciano, Phys. Rev. **D 41**, 1736 (1990).

[32] B. Barish *et al.*, Phys. Rev. **D 51**, 1014 (1995).

[33] M. Artuso *et al.*, Phys. Rev. Lett. **B 399**, 321 (1997).

[34] J. P. Alexander *et al.*, (CLEO), CLNS 00/1670, submitted to Phys. Rev. Lett. (2000).

[35] M. S. Saulnier, Ph.D. Thesis, Harvard University, (1995) (unpublished).

[36] J. Schwinger, Particle, Source, and Fields, Vol. II Addison Wesley 1973.

[37] N. Byers and E. Eichten, Phys. Rev. **D 42**, 3885 (1990).

[38] E. Eichten, K. Gottfried, T. Kinoshita, K. D. Lane, Phys. Rev. **D 42**, 203 (1980).

[39] F. Morrow, CLEO internal report CBX 90-5 (1990).

[40] G. C. Fox and S. Wolfram, Phys. Rev. Lett. **B 41**, 1581 (1978).

[41] D. G. Cassel and M. Ogg, CLEO internal report CSN 83-333 (1983); R. Kutschke, CSN 94-334 (1994) and R. Kutschke, CNS 94-335 (1994).

[42] Roy Wang, Ph.D. Thesis, University of Minnesota, (1994) (unpublished).

[43] J. Richman, Z. Phys. **C 73**, 601 (1997).

[44] J. Bartelt, *et al.*, (CLEO) Phys. Rev. Lett, **80** 3919 (1998).

[45] D. Besson, CLEO internal report CBX 96-001 (1996).

[46] M. Garcia-Sciveres, CLEO internal report CBX 93-114 (1993).

[47] B Decays, 2^{nd} Edition, Edited by S. Stone, World Scientific, Singapore (1993).

[48] M. L. Perl *et al.*, Phys. Rev. Lett. **35**, 1489 (1975).

[49] F. Halzen and A. D. Martin, Quarks and Leptons: An Introductory Course in Modern Particle Physics, Wiley (1984).

[50] Burcham and Jobes, Nuclear and Particle Physics, Longman Scientific & Technical (1995).

[51] M. Suzuki, Nucl. Phys. **145 B**, 420 (1978).

[52] C. Quigg and J. Rosner, Phys. Rev. **D 19**, 1532 (1979).

[53] N. Cabibbo *et al* Nucl. Phys. **B 155**, 93 (1979).

[54] N. Isgur and M. Wise, Phys. Lett. **B 232**,113 (1989); N. Isgur and M. Wise, Phys. Lett. **B 237**,527 (1990); E. Eichten and B. Hill, Phys. Lett. **B 234**,511 (1990); H. Georgi Phys. Lett **B 240**, 447 (1990).

[55] M. Gell-Mann and A. Pais, *Phys. Rev.* **97**, 1387 (1955).

[56] H. Albrecht et al. (ARGUS) *Phys Lett.* **B192**, 245 (1987).

[57] H-Y. Cheng, *Phys. Rev.* **D. 26**, 143 (1982).

[58] Y. Kubota *et al.*, *Nucl. Instrum. Methods* **A 320**, 66 (1992).

[59] F. Ukegawa, in *Proc. 3rd Int. Conf. on B Physics and CP Violation*, Taipei, Taiwan (1999).

Appendix A

Alternative Evaluation of π^0 Fakes

To estimate the fake π^0 background, we construct candidates consisting of a lepton and a π^0 candidate with mass away from the true π^0 mass, in the "sidebands." To define the appropriate π^0 sidebands and scaling factors, we studied fake π^0 mesons in Monte Carlo events. The signal region was selected to include candidates falling approximately within 3σ of the true π^0 mass. To select a sideband, we formed $\ell - \pi^0$ candidates using fake π^0 mesons in the signal and in a prospective sideband region and compared the distributions in $\widetilde{\mathcal{M}}_\nu^2$. Only sidebands that were symmetric around the π^0 mass were examined. Figure A.1 shows the mass distribution of π^0 candidates for $\ell - \pi^0$ candidates passing all other cuts, excluding $\widetilde{\mathcal{M}}_\nu^2 > -2.$ GeV^2, and the same distribution with real π^0 mesons removed. The figure also shows the regions defined as signal and sideband. Figure A.2 shows the $\widetilde{\mathcal{M}}_\nu^2$ distributions for $l - \pi^0$ candidates with π^0 candidates in the signal region and in the sideband regions (scaled). A variety of sideband cuts was explored. The selected region, ($110 \leq m_{\gamma\gamma} < 120$ MeV/c^2)

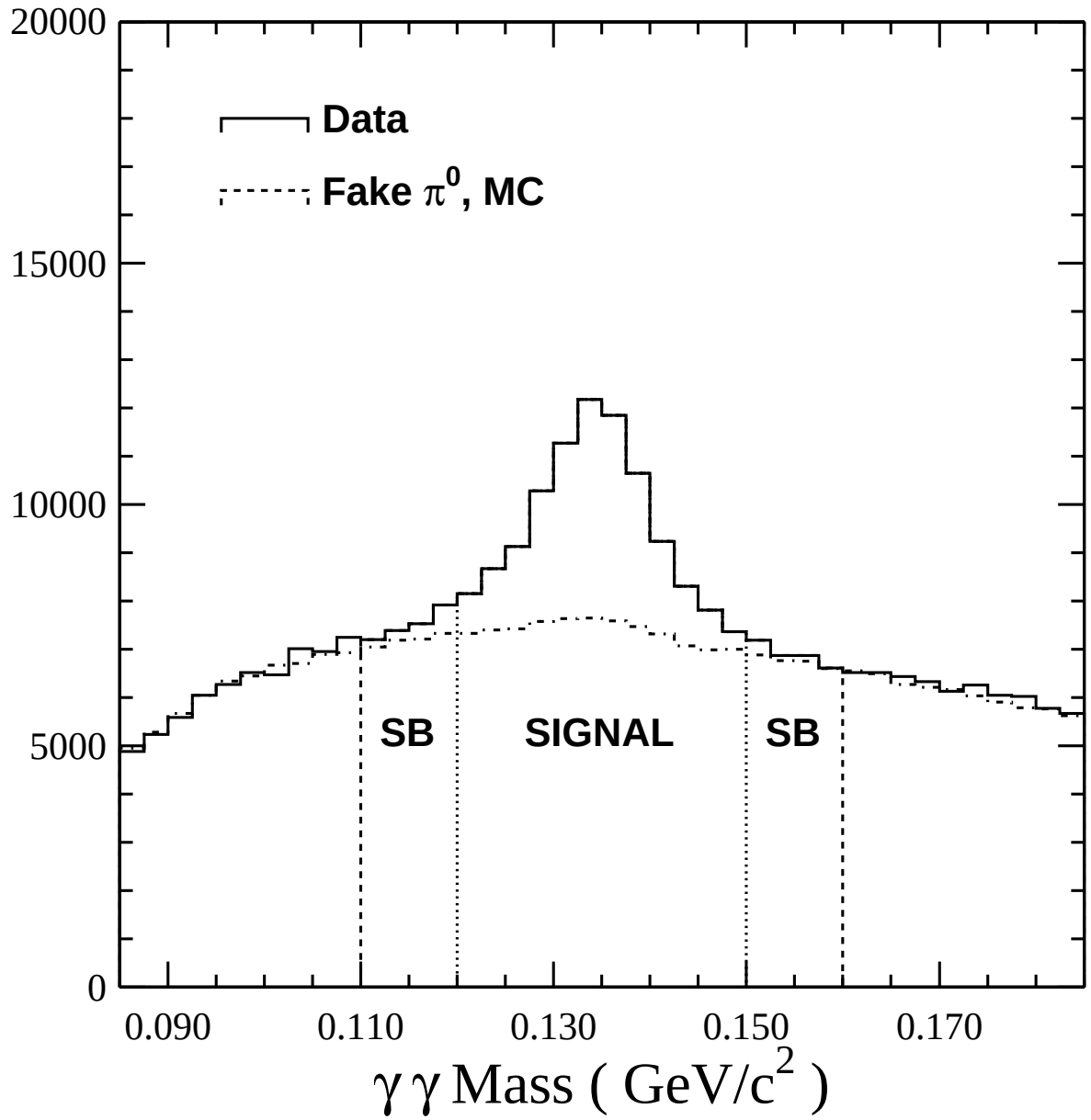

Figure A.1: The $\gamma\gamma$ invariant mass distribution in Monte Carlo with sideband region ($110 \leq m_{\gamma\gamma} < 120\ MeV/c^2$) and ($150 < m_{\gamma\gamma} \leq 160\ MeV/c^2$) and signal region ($120 \leq m_{\gamma\gamma} \leq 150\ MeV$).

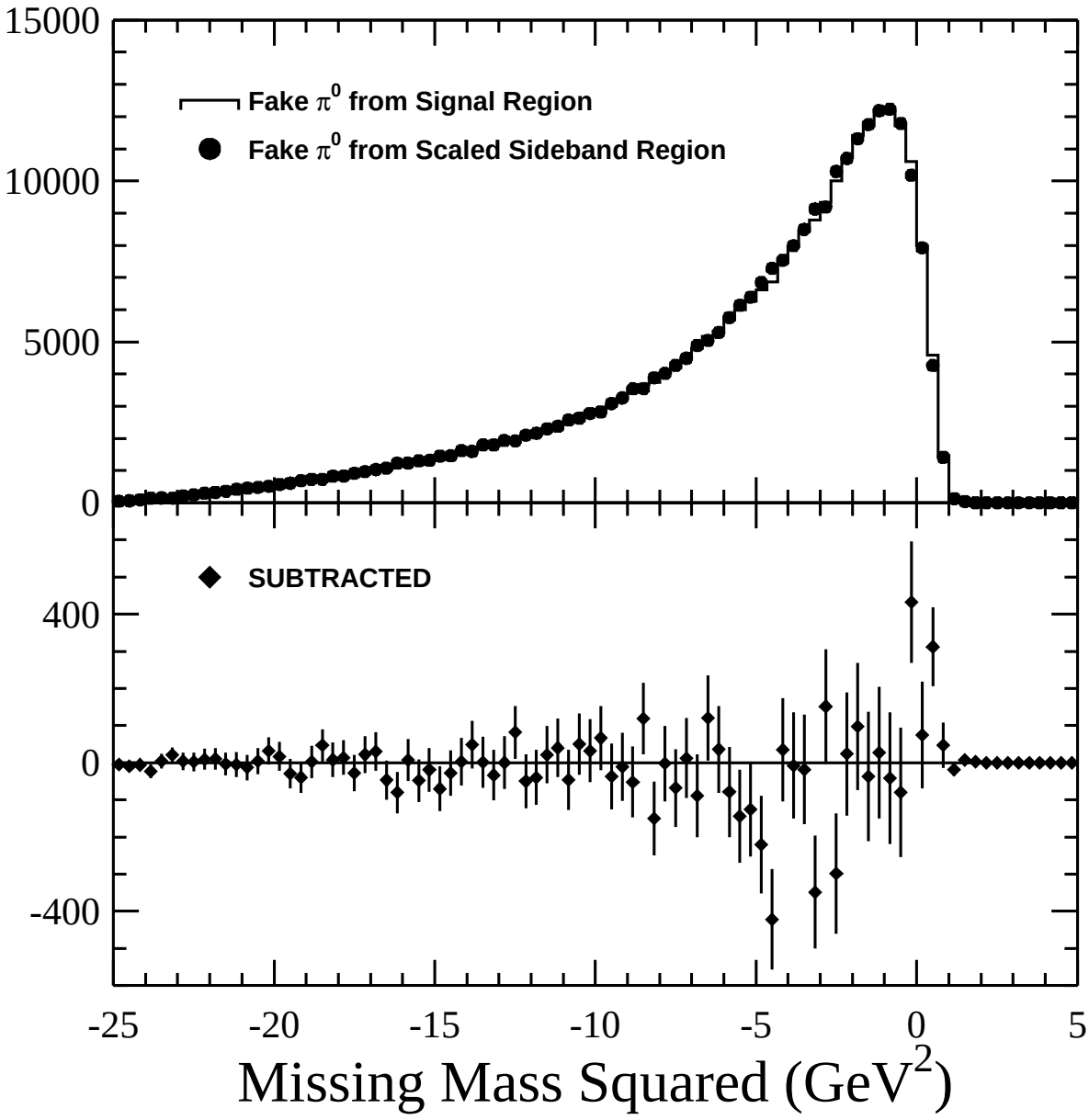

Figure A.2: $\widetilde{\mathcal{M}}_\nu^2$ distribution for $\ell - \pi^0$ candidates with π^0 candidates in the signal region and in the sideband regions (scaled).

and ($150 < m_{\gamma\gamma} \leq 160$ MeV/c^2), gave the best match to the signal region shape. The scaling factor was determined to be $\beta_{\pi^0} = 1.595 \pm 0.009$. The distributions in $\widetilde{\mathcal{M}}_\nu^2$ of candidates in data are shown in Figure A.3 (upper plot), where the π^0 candidate is in the signal and scaled π^0 sideband regions. The ratio of signal to fake π^0 background is about 1 to 6 in the SG region. This fake π^0 background is subtracted as shown in the lower part of the Figure A.3.

The remaining uncorrelated background under the $\widetilde{\mathcal{M}}_\nu^2$ peak, from random combinations of real leptons and π^0 mesons, is calculated using generic Monte Carlo $B\bar{B}$ events with tagged signal and correlated background candidates removed, as was done in the $\ell - \pi^+$ analysis and is shown with the data in Figure A.4.

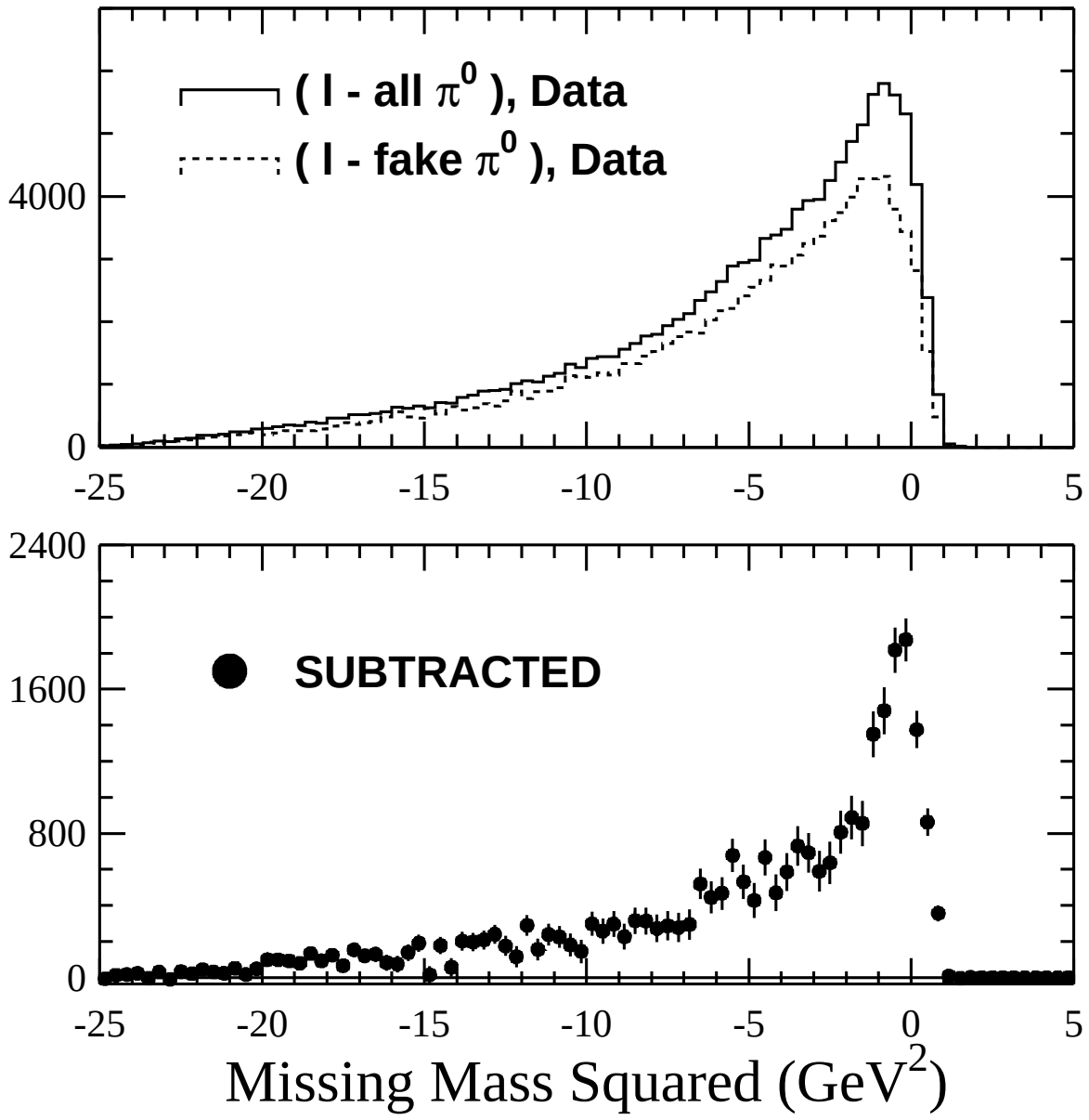

Figure A.3: The squared missing mass distribution for $\ell - \pi^0$: combination of real and fake π^0 with lepton distribution (continuum subtracted) in data.

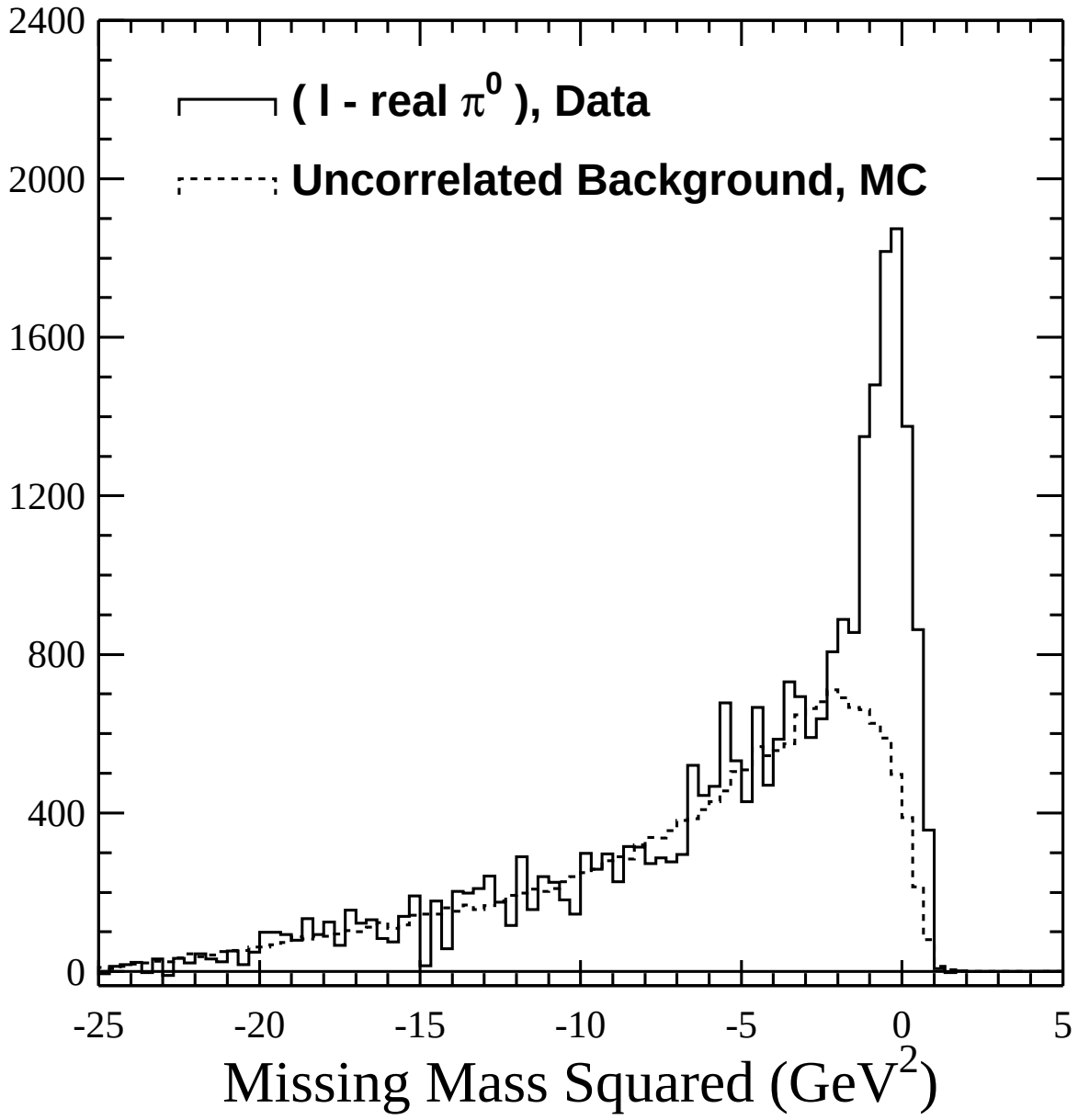

Figure A.4: The missing mass squared distribution for $\ell - \pi^0$.

Appendix B

CLEO Terminology

This Appendix details the meaning of various CLEO terminology, analysis variables, and lists some of their allowed values. This information is taken from the include files which declare the CLEO common blocks, most of which are located on the Cornell Alphas in `/cleo/clib/cvssrc/seq/clinc`.

```
CCCCCCCCCCCCCCCCCCCCCCCCCCCCCCCCCCCCCCCCCCCCCCCCCCCCCCCCCCCCCCCCCCCCCCC
C KINCD  - Track Classification
C      ( = 0 for good primary track
C      (   2 for good secondary track
C      (  -1 no z information, only r-phi. Do not use.
C      (  -2 KINCD=0 but identified as the inward
C                    going half of a curler. Do not use.
```

```
C      (  -3 KINCD=-1 but identified as the inward
C                       going half of a curler. Do not use.
C         -4 ... -8 These are created by the Kalman filter and
C                     are copies of KINCD=0 tracks which have been
C                     refitted using a different mass hypothesis.
C         -4 = electron hypothesis
C         -5 = muon hypothesis
C         -6 = kaon hypothesis
C         -7 = proton hypothesis
C         -8 = pion hypothesis, but at the outermost hit.
C         (The pion hypothesis at the origin is stored as KINCD=0)
C     TNG(I) < 0
C                 track I should be killed by user
C     TNG(I) >= 0
C                 track I should be kept by user
C     INT( TNG(I)/100 )  =  N
C                 track I was killed/kept for broad reason N.
C                 If N is +1 then the track was kept because
C                 it was a surviving ghost.  If N is -2 then
C                 it was killed because it was a curler ...
C TNG             Explanation
```

```
C   0           not found in a subgroup, i.e. a good track

C 101           Tight ghost

C 111           Loose ghost, possible decay in flight

C 112           Loose ghost, both dbcd small

C 113           Loose ghost, both dbcd large

C 201           2 curler, 2 zfits, by far the most populous curler group

C 301           Wee (pronounced vee), i.e. decay in flight or scatter

C 401           dbcd/density regions

C 410           tails

C 501           miscleaneous (killed if cucd = 0 )

C 502           miscleaneous (killed if |pqcd| > 6.5 GeV)

CCCCCCCCCCCCCCCCCCCCCCCCCCCCCCCCCCCCCCCCCCCCCCCCCCCCCCCCCCCCCCCCCCCCCCCCCCCC

C-> DBCD        SIGNED IMPACT PARAMETER WRT BEAM SPOT

C-> CZCD        Z DIRECTION COSINE

C-> ZOCD        Z coordinate at the point of closest approach

C               to the origin.

CCCCCCCCCCCCCCCCCCCCCCCCCCCCCCCCCCCCCCCCCCCCCCCCCCCCCCCCCCCCCCCCCCCCCCCCCCCC

C IQALDI - DE/DX QUALITY OF THE TRACK

C       IF =  0, NO DE/DX information

C       IF =  1, DE/DX information available with   NHITDI>10

C       IF = -2, DE/DX information available with 4<NHITDI<11
```

```
* DE50DI - MEAN OF THE LOWEST 40 PERCENT OF PULSE HEIGHTS

* RESDI  - EXPECTED RESOLUTION FOR THAT PULSE HEIGHT AND NUMBER OF HITS

* SGELDI - NUM. SIGMA AWAY FROM AN ELECTRON (DE50DI-ELDEDI) / RESDI

* SGMUDI -  "     "    "    "    A MUON        "    MUDEDI     "

* SGPIDI -  "     "    "    "    " PION        "    PIDEDI     "

* SGKADI -  "     "    "    "    " KAON        "    KADEDI     "

* SGPRDI -  "     "    "    "    " PROTRON     "    PRDEDI     "

CCCCCCCCCCCCCCCCCCCCCCCCCCCCCCCCCCCCCCCCCCCCCCCCCCCCCCCCCCCCCCCCCCCCCCCCCCCCCC

* ENTRSH(I)   - total CCFC calorimeter energy matched to track I

* EPTRSH(I)   - energy/momentum = ENTRSH(I)/PPTRSH(I)

* ENTRSH(I)   - total CCFC calorimeter energy matched to track I

CCCCCCCCCCCCCCCCCCCCCCCCCCCCCCCCCCCCCCCCCCCCCCCCCCCCCCCCCCCCCCCCCCCCCCCCCCCCCC

C TFSTAT - Status word:  TFSTAT = 0 ----> no ToF measurement

C                        TFSTAT = 1 ----> Endcap ToF measurement

C                        TFSTAT = 2 ----> Barrel ToF measurement

C TFIDQL - Quality word: TFIDQL =  0 ----> good time measurement

C                        TFIDQL =  4 ----> T_east - T_west = 1 ns

C                        TFIDQL =  8 ----> ADC Saturated

C                        TFIDQL = 12 ----> Both 4 and 8 happened

C RESTF  - Estimated resolution for this measurement

C DTELTF - Difference from expected electron time in nanoseconds
```

```
C DTMUTF - Difference from expected muon time in nanoseconds
C DTPITF - Difference from expected pion time in nanoseconds
C DTKATF - Difference from expected kaon time in nanoseconds
C DTPRTF - Difference from expected proton time in nanoseconds
C SGXXTF - Same, but in units of sigma (DTXXTF/RESTF)
C BETATF - Relativistic Beta of the particle
CCCCCCCCCCCCCCCCCCCCCCCCCCCCCCCCCCCCCCCCCCCCCCCCCCCCCCCCCCCCCCCCCCCCCCCCCCCC
C  DPTHMU         - maximal depth in absorption lenghts at which
C                    CD track MUTRDR(IMUTR) correlates to good quality
C                    hits in the MU detector.
C                    (roughly speaking, "good quality" = two of three
C                    layers hit in a MU chamber unit)
C  MUQUAL          - MU track quality flag :
C  MUQUAL .EQ. 0   - CD track MUTRDR(IMUTR) correlates with muon hits
C                    everywhere expected.
C  MUQUAL .NE. 0   - CD track MUTRDR(IMUTR) fails to correlate to any
C                    hits in at least one of iron gaps where it was
C                    expected to hit MU chambers.
CCCCCCCCCCCCCCCCCCCCCCCCCCCCCCCCCCCCCCCCCCCCCCCCCCCCCCCCCCCCCCCCCCCCCCCCCCCC
C R2ELEC - Log-Likelihood that the track is an electron.
C          The variables that the Electron ID package uses are:
```

```
C           1.  SGELDI

C           2.  EPTRSH

C           3.  Distance of track-to-shower match

C           4.  LP2SH  RMS shower width (meters)

C           5.  LP4SH  (shower shape, E9/E25 = Sum of  9 crystals

C                       about highest divided by Sum of 25 crystals

C                       around highest)

C           6.  LP3SH  (theta width / phi width)

C           7.  SGELTF

CCCCCCCCCCCCCCCCCCCCCCCCCCCCCCCCCCCCCCCCCCCCCCCCCCCCCCCCCCCCCCCCCCCCCCCCCCCCCCC

C NTRKCD    Number of charged tracks in CD (PT+VD+DR)

C R2GL      Ratio of second to zeroth Fox-Wolfram moments

C PQCD      Track momentum with electric charge as sign

C CZCD      cos theta of track where z is the beam axis

C DBCD      Track impact parameter in r-phi

C Z0CD      Track impact parameter in r-z

C RESICD    RMS residual in tracking fitting

C TRKMAN    Program to kill false tracks

C NHITPT    Number of hits in PT for track

C NHITVD    Number of hits in VD for track

C RHITVD    Percentage of DR hits over expected for a track
```

```
CCCCCCCCCCCCCCCCCCCCCCCCCCCCCCCCCCCCCCCCCCCCCCCCCCCCCCCCCCCCCCCCCCCCCCCC
$ CLEO DATASETS
$
$ Name Run Range    Dates Taken      Luminosity    Comment
$
$ 4S2  36233-40095  11NOV90-04JUN91  672.0 (Pb-1)  Single IP
$ 4s3  41386-45969  18SEP91-17FEB92  680.2 (Pb-1)  DAQ90/LVL3
$ 4s4  46035-48057  10APR92-26MAY92  317.5 (Pb-1)  DME in PT
$ 4s5  48789-51406  09JUL92-05OCT92  342.7 (Pb-1)  -
$ 4s6  51431-53702  03NOV92-19JAN93  316.5 (Pb-1)  Mark III
$ 4s7  53741-56976  16MAR93-06JUL93  461.3 (Pb-1)  -
$ 4s8  57038-58813  01AUG93-27SEP93  274.4 (Pb-1)  -
$ 4s9  58836-60576  22NOV93-10JAN94  340.1 (Pb-1)  -
$ 4sA  60770-61778  20JAN94-28FEB94  190.8 (Pb-1)  -
$ 4sB  61826-62855  19MAR94-16MAY94  140.9 (Pb-1)  X-angle
$ 4sC  63086-64026  16JUN94-15AUG94  141.5 (Pb-1)  -
$ 4sD  64085-64674  15SEP94-09OCT94  98.0  (Pb-1)  -
$ 4sE  64675-65238  09OCT94-01NOV94  128.8 (Pb-1)  VD broken
$ 4sF  65252-65818  03NOV94-28NOV94  145.9 (Pb-1)  9t2b(on)
$ 4sG  66539-68027  19JAN95-09APR95  456.6 (Pb-1)  -
CCCCCCCCCCCCCCCCCCCCCCCCCCCCCCCCCCCCCCCCCCCCCCCCCCCCCCCCCCCCCCCCCCCCCCCC
```

Appendix C

TOF Terminology

This Appendix details the meaning of various TOF terminology and codes for calibrating TOF raw data.

```
CCCCCCCCCCCCCCCCCCCCCCCCCCCCCCCCCCCCCCCCCCCCCCCCCCCCCCCCCCCCCCCCCCCCCCC
C  Directories for TOF Barrel and Endcap Calibration Constants
C  Author: Romulus Godang
C  TF.ZFX  GODANG
C  TF/BARREL/ATTEN                 96542 -  96667
C  TF/BARREL/CHARGE/BHABHA         96542 -  96667
C  TF/BARREL/CHARGE/RELATIVE_GAIN  96542 -  96667
C  TF/BARREL/ZCON                  96542 -  96667
C  TF/BARREL/QCON                  96542 -  96667
```

```
C  TF/BARREL/RESOL                  96542 -  96667

C  TF/BARREL/TZERO/TUBE             96542 -  96667

C  TF/BARREL/ZCONB3                 96542 -  96667

C  TF/BARREL/QCONB3                 96542 -  96667

C  TF/BARREL/RESOLB3                96542 -  96667

C  TF/BARREL/TZERO/TUBEB3           96542 -  96667

C  TF/BARREL/ZCONB5                 96542 -  96667

C  TF/BARREL/QCONB5                 96542 -  96667

C  TF/BARREL/RESOLB5                96542 -  96667

C  TF/BARREL/TZERO/TUBEB5           96542 -  96667

C  TF/BARREL/TZERO/RUN              96542 -  96667

C  TF/ENDCAP/ATTEN                  96542 -  96667

C  TF/ENDCAP/CHARGE/BHABHA          96542 -  96667

C  TF/ENDCAP/CHARGE/RELATIVE_GAIN   96542 -  96667

C  TF/ENDCAP/ZCON                   96542 -  96667

C  TF/ENDCAP/QCON                   96542 -  96667

C  TF/ENDCAP/RESOL                  96542 -  96667

C  TF/ENDCAP/TZERO/TUBE             96542 -  96667

C  TF/ENDCAP/ZCONB3                 96542 -  96667

C  TF/ENDCAP/QCONB3                 96542 -  96667

C  TF/ENDCAP/RESOLB3                96542 -  96667
```

```
C  TF/ENDCAP/TZERO/TUBEB3          96542 -  96667

C  TF/ENDCAP/ZCONB5                96542 -  96667

C  TF/ENDCAP/QCONB5                96542 -  96667

C  TF/ENDCAP/RESOLB5               96542 -  96667

C  TF/ENDCAP/TZERO/TUBEB5          96542 -  96667

C  TF/ENDCAP/TZERO/RUN             96542 -  96667

CCCCCCCCCCCCCCCCCCCCCCCCCCCCCCCCCCCCCCCCCCCCCCCCCCCCCCCCCCCCCCCCCCCCCCCCCCC

C Software Inspection Checklist

C Author:Jorge Rodriguez

C Inspector:Romulus Godang

C Program(s):

C   bunch.F       :  Deletion of histograms improved

C   calinit.F     :  Events between bunches removed and added more docs

C   chkallcnt.F   :  Added more docs

C   fcnresz.F     :  New subroutine for new sigmas calculation

C   filres.F      :  Events between bunches removed and added more docs

C   fulcorr.F     :  Added a debug ntuple and improved docs

C   gtbtime.F     :  Endcap resolution calculation bug fix

C   hgausp1.F     :  New subroutine for new sigmas calculation

C   meanadc.F     :  Deletion of histograms improved

C   rbrcorr.F     :  Events between bunches removed and added more docs
```

```
C   readnt.F      :  Events between bunches removed and added more docs

C   rqlims.F      :  Deletion of histograms improved

C   rt0lims.F     :  Events between bunches removed

C   savezf.F      :  Modified to reflect changes in new sigma calculation

C   sigmas.F      :  Complete rewrite

C   tofcal.F      :  Cosmetic changes

C   tofcsig.inc   :  Modified to work with new sigmas.F

CCCCCCCCCCCCCCCCCCCCCCCCCCCCCCCCCCCCCCCCCCCCCCCCCCCCCCCCCCCCCCCCCCCCCCCCCCCC

C  TOF Resolution Comparison

C Data Comment  tf.zfx  EC dtel EC dtp  BA dtel BA dtpi BA dtka BA dtmu

C                       (ps)    (ps)    (ps)    (ps)    (ps)    (ps)

C ---- -------  ------  ------  ------- ------- ------- ------- -------

C 4sD  pre-slope CCON    251     444     158     170     163     159

C 4sD  pre-slope TEB     220     338     157     174     167     171

C 4sD  pre-slope Romulus 221     311     159     170     163     158

C 4sD  post-slop TEB     266     441     166     180     183     167

C 4sD  post-slop CCON    264     551     166     179     191     162

C 4sE  post-slop Romulus 265     550     165     185     167     158

C 4sF  post-slop Romulus 288     487     174     176     217     138

CCCCCCCCCCCCCCCCCCCCCCCCCCCCCCCCCCCCCCCCCCCCCCCCCCCCCCCCCCCCCCCCCCCCCCCCCCCC
```

Vita

Romulus Godang was born in Sibolga, Indonesia. He received a Bachelor of Physics with high honors from University of North Sumatra in August 1987. During 1988-1991, he was a Senior Researcher at University of North Sumatra and a Headmaster at Sutomo High School in Indonesia. He came to the United States in 1992 for graduate study. He received a Master of Science from Virginia Polytechnic Institute and State University in August 1994. He joined the CLEO experiment in January 1996 and was stationed in Ithaca, New York from 1996-2000. He received a Doctor of Philosophy in Physics from Virginia Polytechnic Institute and State University in August 2000.